Contents

Chapter 1

Introduction

1.1 Cosmological parameters

Cosmology is the study of the large-scale structure of the Universe extending to distances of billions of light-years. Although such a study may appear an ambitious task, our Universe has the remarkable characteristic that on large scales it is close to homogeneous and isotropic. Density fluctuations are confined to scales less than a few hundred million light years (1 megaparsec $\sim$ 3 million light years) (Peebles 1993). Moreover, the average of these fluctuations reveals a Universe that looks much the same in all directions and would appear much the same when viewed from any other position, as if there were no preferred centre and no edges. This simplicity of the large scale Universe makes it possible for us to make some sense out of the observable Universe. One might ask whether the problem is circular, that cosmologists have invented a Universe that is easy to describe. For the time being there is no way we can consult intelligent life in a distant galaxy to see if they observe the Universe the same way we do. However, measurements of the microwave background radiation, of X-ray background from distant sources, and deep galaxy counts, all show that the large scale Universe is quite close to isotropic around our position. Therefore, either we are at a very special central place of the Universe, or the observable Universe is close to homogeneous. The latter interpretation leads to the standard cosmological theory characterized by: (i) a homogeneous mass distribution in the large-scale average; (ii) the Universe is expanding; (iii) the dynamics of the expanding Universe is described by Einstein's general relativity theory (except for very early epochs where conventional physics cannot be applied; and (iv) the Universe expands from a hot dense state where its mass was dominated by thermal blackbody radiation.

Cosmological parameters that govern geometry and evolution of the Universe are: the Hubble parameter H, the mass density ρ, the curvature parameter k and the cosmological constant Λ. The *Hubble constant* H_0 is a dimensional parameter that describes the current expansion rate of the Universe. It is defined as:

$$H_0 = \frac{\dot{R}}{R}_{t=0} \tag{1.1}$$

where R is the time dependent scale factor of the Universe, also called the *expansion factor*, and $\dot{R}$ is its time derivative, thus the expansion velocity. The Hubble parameter

H changes with time and the subscript "0" refers to the present epoch. The dimension of H_0 is the inverse of time but is by convention expressed as km s^{-1} Mpc^{-1} as e.g.,

$$H_0 = 100\ h_0 \text{ km s}^{-1} \text{ Mpc}^{-1} \tag{1.2}$$

where h_0 is a dimensionless number.

The mass density ρ_0 is the present value of the mean mass density in material, such as galaxies and intergalactic gas and stars. The cosmological constant Λ can be looked upon as a force of cosmic repulsion. This means that a universe with a given mass density ρ and a positive cosmological constant will present a faster expansion than a universe with the same ρ and $\Lambda = 0$. Physically it can be described as a constant proportional to the vacuum energy density in the Universe. Abbott (1988) discusses the cosmological constant and its influences on our Universe. The mass density and the cosmological constant are often transformed into dimensionless density parameters, Ω_m and Ω_Λ, according to Peebles (1993):

$$\Omega_m = \frac{8\pi G\rho_0}{3H_0^2} = \frac{\rho_0}{\rho_c} \tag{1.3}$$

$$\Omega_\Lambda = \frac{\Lambda c^2}{3H_0^2} \tag{1.4}$$

where G is the constant of gravity and ρ_c is the critical density of the Universe, i.e., the density of the Universe necessary so that the expansion rate of the Universe is just sufficient to prevent a recollapse. For $\rho \le \rho_c$, the Universe expands forever, while for $\rho > \rho_c$, the Universe will eventually stop expanding and recollapse.

The parameter k measures the curvature of space. For $k = -1$ the Universe has negatively curved or hyperbolic geometry, for $k = 0$, the Universe has Euclidean or flat geometry and for $k = 1$, the Universe has positively curved or spherical geometry.

Given the total energy density of the Universe, the Hubble constant sets the age of the Universe, t_0. In the special case of a so-called Einstein-de Sitter Universe, a flat Universe with zero cosmological constant and a mass density equal to the critical density ($\Omega_m = 1$, $\Omega_\Lambda = 0$ and $k = 0$) the age of the Universe is:

$$t_0 = \frac{2}{3H_0} \tag{1.5}$$

With a non-zero cosmological constant ($\Omega_\Lambda > 0$) the expansion of the Universe will accelerate and t_0 will increase for a given H_0.

What are their values ?

Recent observations of the cosmic microwave background from the BOOMERanG and the MAXIMA experiments have provided strong evidence for a flat Universe, i.e., $\Omega_0 = \Omega_m + \Omega_\Lambda = 1$ (de Bernadis et al. 2000, Lange et al. 2000, Balbi et al. 2000). Moreover, observations of high-redshift supernovae (Riess et al. 1998; Perlmutter et al. 1999) suggest a non-zero cosmological constant. A model commonly used today is a flat Universe with $\Omega_m = 0.3$, $\Omega_\Lambda = 0.7$. These values have also recently been confirmed by estimates of the mass density from clustering of galaxies in the 2dF Galaxy Redshift Survey (Peacock et al. 2001). Fig. 1.1 shows the constraints on Ω_m and Ω_Λ from the BOOMERanG experiment (de Bernadis et al. 2000). We see that the "allowed" (dotted) region is elongated around the $\Omega_0 = 1$ line, identifying a flat geometry i.e., a Euclidean Universe. There are lines defining the age of the Universe in units of H_0^{-1} for the considered models. The shaded region is consistent (95% confidence contour) with the recent results of high-redshift supernovae surveys (Perlmutter et al. 1999, Schmidt et al. 1998).

The Hubble constant is believed to lie somewhere in the range $50-70$ but there is still much debate about its value. I shall here leave the density parameters and look into how the Hubble constant can be measured with different methods, and in particular using gravitational lensing.

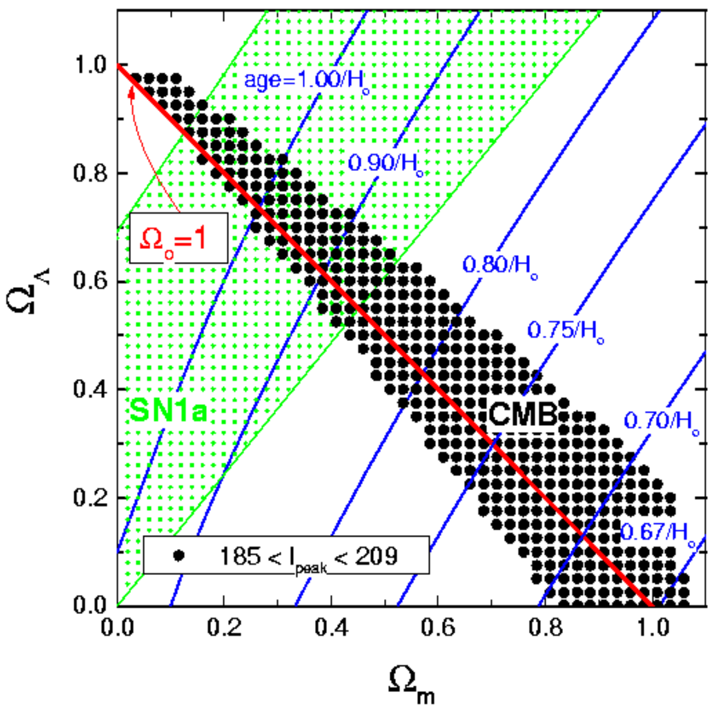

Figure 1.1: Observational constraints on Ω_m and Ω_Λ from the BOOMERanG experiment (from de Bernadis et al. 2000). The "allowed" (dotted) region is elongated around the $\Omega_0 = 1$ line, identifying a flat geometry, Euclidean Universe. The lines define the age of the Universe for the considered models. The shaded region is consistent (95% confidence contour) with the recent results of high-redshift supernovae surveys (Perlmutter et al. 1999, Schmidt et al. 1998).

1.1.1 Measuring the Hubble constant

The Hubble constant is a quantity which sets the basic size and age of the Universe. Since Hubble first tried to determine its value in 1925 there have, for a variety of reasons, been much dispute about its value. Before 1980 there were basically two schools: Sandage and collaborators who defended H_0 close to 50 (Sandage & Tammann 1982); and de Vaucouleurs and collaborators who suggested a higher value around 90 to 100 (de Vaucouleurs 1981). Since the 1980's, a number of new observing techniques, e.g., the replacement of photographic plates by Charge Coupled Devices (CCDs), have enabled more accurate measurements. However, there are still considerable uncertainties in the absolute value of this important cosmological parameter. This is mainly due to the difficulty of measuring astronomical distances.

H_0 relates the redshift z of a nearby galaxy to its distance D from us:

$$cz = H_0 D \tag{1.6}$$

where c is the velocity of light. Therefore measuring z and D for a number of galaxies, allows one to estimate H_0, as first conducted by Hubble. Whereas redshifts can be measured accurately, all actual distance measurements suffer from different kinds of systematic errors. Depending on the method used, the systematic errors are of different nature. It is common to divide the methods into what are known as "classical" and "physical" distance indicators.

Classical distance indicators

Most of the classical distance indicators were chosen because their intrinsic luminosity L can be estimated without prior knowledge about their distance. The absolute magnitude M is defined as $M = -2.5 \log L + \mathit{constant}$, where the constant is fixed by defining M as the apparent magnitude of an object if it was viewed from a distance of 10pc. By measuring the apparent magnitude m, the luminosity distance D can be estimated with the so-called distance modulus:

$$m - M = 5 \log(D) - 5 \tag{1.7}$$

where D is the distance measured in parsecs. If we substitute Eq. 1.6 in Eq. 1.7 with $H_0 = 100\ h_0\ \mathrm{kms}^{-1}\mathrm{Mpc}^{-1}$ and also substitute the value of c we get the following relation:

$$5 \log h_0 = 42.38 + (M - m) + 5 \log z. \tag{1.8}$$

A determination of the distance modulus $(M - m)$ and the redshift for a galaxy can hence be used to estimate h_0.

Cepheid variables are the primary classical distance indicators. The outer atmosphere of these stars pulsates regularly with a period varying from 2 to about 100 days. It has been established empirically that the period of pulsation is very well correlated with their intrinsic luminosity which itself is directly related to the distance to the object. The dispersion in the period-luminosity relation in the I band amounts to about 20% in luminosity, corresponding to an uncertainty of $\sim 10\%$ in the distance for a single Cepheid

(Freedman 2000). Strengths and weaknesses of Cepheids are described in, e.g., Feast & Walker (1987) and Madore & Freedman (1991). The main problem with Cepheid variables as distance indicators is their limited reach. Beyond ~20 Mpc, brighter objects are needed as secondary indicators. Several methods therefore use bright distant objects to measure relative distances to galaxies, e.g. type Ia supernovae (Tammann & Sandage 1995; Riess 1996), the Tully-Fisher relation (Tully & Fisher 1977), the fundamental plane (Faber & Jackson 1976) and surface brightness fluctuations (Tonry & Schneider 1988).

Type Ia supernovae result from the explosion of a white dwarf, probably triggered by the accretion of material from a binary companion. Supernovae are very bright and can be observed to distances of hundreds of Mpc. Since type Ia supernovae originate from identical systems it is predicted that their maximum luminosity is the same, which provide ideal standard candles observable at large distances. Empirically a relation has also been found between the luminosity of the supernova at its maximum and the rate at which the supernova decreases in brightness. A well determined supernova lightcurve may thus give the intrinsic maximum luminosity and hence its distance. The uncertainty is of about 6% in the distance to a single supernova. Unfortunately, the exact mechanism for the ignition of the explosion has not yet been theoretically or observationally established. Moreover there are possible extinction effect from the host galaxies that must be taken into account. Better confidence in this empirically-based method will be strengthened once the theoretical basis is more firmly established.

The Tully-Fisher relation is a correlation of the total luminosity of spiral galaxies with their maximum rotation velocity. The galaxy rotation rates can be measured spectroscopically and the luminosity and hence the distance can be inferred. The dispersion in this relation amounts to about 15% in distance for an individual galaxy (Freedman 2000).

For elliptical galaxies there exist a relation between the stellar velocity dispersion and the intrinsic luminosity. Elliptical galaxies also occupy a "fundamental plane" wherein the galaxy size is correlated with the surface brightness and velocity dispersion of the galaxy. The scatter in this relation is $10 - 20\%$ in distance.

Finally there is the method using surface brightness fluctuations (SBF) in the luminosity from stars on a CCD. The resolution of stars within galaxies is distance dependent. By normalizing the mean flux, and correcting for an observed colour dependence, relative distances to galaxies can be measured with a precision of $\sim 8\%$. The application of the method requires careful removal of sources of noise such as bad pixels on the detector, dust lanes, background galaxies and foreground stars.

All these classical methods need Cepheid distances for an absolute calibration, with the zero point being the distance to the Large Magellanic Cloud (LMC) (50 kpc). For this reason they are said to use "distance ladders". The inconvenience about distance ladders is that all the errors accumulate, e.g., an error in the zero-point will propagate into longer distances. Although Cepheids are generally considered to be the most reliable distance indicators, certain questions remain as to their zero-point calibration through LMC and the effect of metallicity variations. Results obtained with classical methods have recently been published by Freedman et al. (2000, results from the HST Key Programme) and Tammann et al. (2000) (see Table 1.1). The fact that these two groups obtain different values using the same methods is due to disagreements in their way of taking into account the various systematic errors.

Physical distance indicators

The so-called physical distance indicators are completely independent of the classical methods. The most common of these methods are based on (1) anisotropies in the cosmic microwave background (CMB) (Hu & White 1996), (2) the Sunyaev Zel'dovich effect (Sunyaev & Zel'dovich 1970, 1971; Carlstrom et al. 2001), and (3) time delays in gravitationally lensed quasars (Refsdal 1964b).

The cosmic microwave background contains a vast amount of information about cosmological parameters. So far the results (Hu, et al. 2000) are limited by few and uncertain observations. However, over the next few years, upcoming experiment, notably the two satellite missions *Microwave Anisotropy Probe* (MAP) and *Planck* will provide detailed measurements of the angular power spectra, of its anisotropy and polarization, which may determine many cosmological parameters with great accuracy. Eisenstein et al. (1998) find that combining future redshift surveys with CMB anisotropy data may yield an accuracy of 5% on H_0.

The Sunyaev Zel'dovich effect is a small spectral distortion of the CMB in clusters of galaxies. When CMB photons interact with high-energy electrons in cluster of galaxies they are partially scattered into X-rays. The effect can be caused by hot thermal distribution of electrons provided by the intracluster medium of massive galaxy clusters. As a result, measurements of the microwave background spectrum towards rich clusters of galaxies show a decrement at lower frequencies (and a corresponding increase at higher frequencies). The size of the decrement depends on the density of electrons in the cluster and the path length through the cluster, but is independent of the cluster distance. The observed X-ray flux from the cluster is, however, dependent on the distance to the cluster. If it can be assumed that the cluster is spherically symmetric, the distance to the cluster can be measured by combining the Sunyaev Zel'dovich effect with X-ray observations. It is assumed in this method that the gas distribution in clusters is uniform. If this is not the case then there will be systematic errors in the inferred values of H_0.

The "time delay" between the gravitationally lensed images of a distant source is a measurable parameter. Observed as the time difference between the arrival dates of the lensed wavefronts originating from one single source, it is directly related to the Hubble constant. Obtaining accurate time delay measurements in multiply lensed quasars can therefore yield a determination of H_0 provided the mass distribution in the lens is known. The latter is often a source of systematic errors in the method, as will be discussed in the next chapters.

The main advantage of these physical methods is that they can all be applied directly at very large distances, completely independent of the local extragalactic distance scale. To date, the numbers of measurements from these techniques is still small. Moreover, the systematic errors have not yet been tested thoroughly. However, these three methods are increasingly applied and ongoing and future experiments are likely to lead to rapid progress. Recent results from the three methods are displayed in Table 1.2.

Table 1.1: Recent published values for the standard methods to measure distances in the Universe, and hence H_0. Results from the HST key program (Freedman et al. 2000) are shown in column A and results from Tammann et al. (2001) are shown in column B. Subscripts r and s correspond to estimated random and systematic errors.

Method	H_0(A)	H_0(B)
Local Cepheid galaxies	$71 \pm 2_r \pm 6_s$	54 ± 5
Type Ia supernovae	$72 \pm 9_r \pm 7_s$	58 ± 6
SBF	$70 \pm 5_r \pm 6_s$	
Tully Fisher clusters	$71 \pm 3_r \pm 7_s$	55 ± 5
Fundamental plane	$82 \pm 6_r \pm 9_s$	
Combined	72 ± 8	

Table 1.2: Recent published H_0 estimates from the Sunyaev Zel'dovich effect (Carlstrom 2001) and Cosmic Microwave Background (Hu et al. 2000). The value from gravitational lensing is a mean of all the measurements shown in Table 9.1.

Method	H_0
Sunyaev Zel'dovich	60 ± 18
CMB	60−90
Lensed QSOs	60 ± 4

1.2 Gravitational lensing

During the last twenty years, gravitational lensing (that is, bending of light rays from distant objects due to the mass from foreground objects) has established itself as a very useful astrophysical and cosmological tool. Multiply-imaged quasars can be used to determine the Hubble constant (as will be described in the following sections), to study mass-to-light distribution and extinction laws in galaxies. Quasar microlensing can provide constraints on the size of quasars and on the mass of compact objects in galaxies. Galactic microlensing is used to search for compact halo objects in the Galaxy. On larger scales, the mass distribution of clusters of galaxies can be estimated from giant luminous arcs and arclets, which are galaxies lensed by foreground galaxy clusters. Finally very weak distortions of faint background galaxies that can only be detected statistically, can be used to map the mass distribution of foreground galaxies. Before going into detail on how gravitational lensing can be used to measure the Hubble constant I first present some of the basic physical aspects of the phenomenon. Excellent introductions to gravitational lensing are given by Narayan and Bartelman (1995) and by Refsdal & Surdej (1994). Wambsganss (1998) also gives an overview of the astrophysical applications of the different types of gravitational lensing.

1.2.1 Historical background

Einstein was the first to derive the basic theory of gravitational lensing which results from the phenomenon of light bending. Recent research in Einstein's notes back from 1912 (see Renn et al. 1997) reveals that he developed these basic theories three years before completing his theory of General Relativity. Unfortunately he did not publish them until 24 years later, and even then he considered that this idea could never be confirmed by observations.

Several authors in the 1920's were interested in the phenomenon of light bending. Eddington seems to have been the first to point out that multiple images can occur if two stars are sufficiently well aligned. Zwicky (1937a and 1937b) estimated the probability of a distant source to be multiply imaged to be a few tenths of a percent, very close to modern estimates. Zwicky also predicted that the lens effect would allow the determination of the mass of distant cosmic objects and, due to the magnification effect, allow deeper looks into the Universe.

Much later, in 1962, Sjur Refsdal reopened the subject of gravitational lensing in his Masters' degree thesis, followed by pioneering papers in 1964 (Refsdal 1964a and 1964b). Although the theory was undoubted, the subject was considered by many as unrealistic since observing the phenomenon requires very bright sources at large distances. With the discovery and identification of quasars in 1963 gravitational lensing studies became more realistic, but at the time only a few realized this possibility. It was first in 1979, when Walsh et al. (1979) serendipitously discovered the first quasar that displayed two images due to gravitational lensing that the subject received an increasing popularity. The field has since received increasing attention from a large number of astrophysicists. The discovery of a growing number of lensed quasars and galaxies permit us to investigate massive structures and distances in the Universe in a completely new way. As gravitational light deflection is insensitive to the physical nature of the deflecting mass, it is also ideally suited for the study of dark matter in the Universe.

1.2.2 The lens equation

General relativity predicts that a light ray which passes by a body of mass M at a minimum distance ξ is deflected by the angle $\hat{\alpha}$:

$$\hat{\alpha} = \frac{4GM}{c^2\xi} \tag{1.9}$$

where G is the constant of gravity and c the velocity of light.

In the case of a gravitational lens the light from a distant source is deflected by a lensing mass distribution on its way to the observer. The observer may see several images of the source in directions corresponding to the tangents to the real incoming light paths. In Fig. 1.2 the geometrical principles of a point mass lens (also called "Schwarzshild lens") is displayed. For most practical purposes, we can assume that deflecting matter is thin and situated at a single distance between the source and the observer. The mass distribution of the lens can then be projected along the line of sight and be replaced by a mass sheet orthogonal to the line of sight. We therefore speak of a lens plane, an observer plane and a source plane.

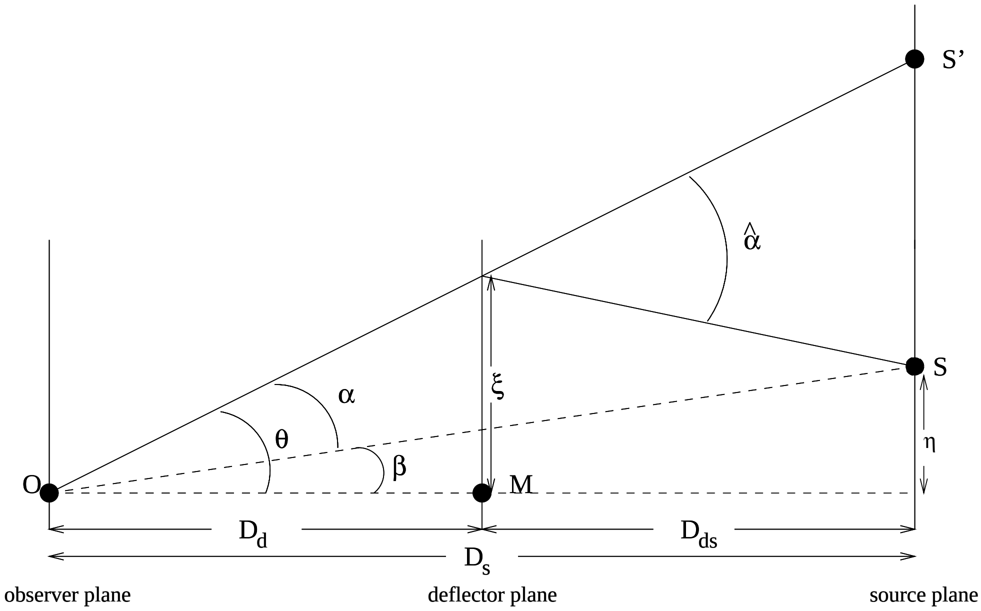

Figure 1.2: The basic geometry for a gravitational lens.

The deflection angle for a circular-symmetric lens is given as

$$\hat{\alpha}(\xi) = \frac{4GM(\xi)}{c^2}\frac{1}{\xi} \tag{1.10}$$

where $M(\xi)$ is the mass inside the radius ξ. If we consider that the angles are very small (θ, β, $\hat{\alpha} \ll 1$ in Fig. 1.2), simple geometry applies and we can write the following:

$$\theta D_s = \beta D_s + \hat{\alpha} D_{ds} \tag{1.11}$$

where D_s, D_d and D_{ds} are angular diameter distances observer-source, observer-deflector and deflector-source. Defining the reduced deflection angle as $\alpha(\theta) = (D_{ds}/D_s)\hat{\alpha}(\theta)$ we can write:

$$\beta = \theta - \alpha(\theta) \tag{1.12}$$

For a non-symmetric mass distribution the angles are vector-valued and the two-dimensional *lens equation* becomes:

$$\vec{\beta} = \vec{\theta} - \vec{\alpha}(\theta) \tag{1.13}$$

1.2.3 Critical surface mass density

In the thin lens approximation, the deflection angle for several point masses can be found by adding the contributions from all the point masses in the lens. All the mass can be considered to be located in the lens plane where the rays cross the deflector. The deflection can therefore be expressed as a two-dimensional vector in the lens plane $\vec{\xi} = (\xi_x, \xi_y)$

$$\hat{\vec{\alpha}}(\vec{\xi}) = \frac{4G}{c^2} \int\!\!\int \frac{\Sigma(\vec{\xi}\,')(\vec{\xi} - \vec{\xi}\,')}{\left|\vec{\xi} - \vec{\xi}\,'\right|^2} \, d\vec{\xi}\,' \tag{1.14}$$

where $\Sigma(\vec{\xi})$ is the surface mass density at position $\vec{\xi}$. It is convenient to replace the physical lengths in (1.14) by angular variables ($\vec{\theta} = \vec{\xi}/D_d$). For a finite circle with constant surface mass density Σ the reduced deflecting angle can be written:

$$\alpha(\theta) = \frac{4\pi G\Sigma}{c^2} \frac{D_d D_{ds}}{D_s} \theta = \frac{\Sigma}{\Sigma_{cr}} \theta = \kappa\theta \tag{1.15}$$

with the *critical surface mass density* Σ_{cr} defined as

$$\Sigma_{cr} = \frac{c^2}{4\pi G} \frac{D_s}{D_{ds} D_d} \tag{1.16}$$

The surface mass density scaled with its critical value is often referred to as the *convergence* κ. It can be shown that a circular disk with uniform surface mass density Σ, acts as a perfect converging lens. In the case where $\Sigma = \Sigma_{cr}$, the lens will focus all the rays from a source onto the observer. For an arbitrary mass distribution, the condition $\Sigma \geq \Sigma_{cr}$ at any point is sufficient to produce multiple images.

1.2.4 The Einstein ring and mass determination

The source will be imaged as a ring if the source, the point mass lens and the observer are perfectly aligned, and if the conditions of supercritical surface density prevail ($\Sigma \geq \Sigma_{cr}$). The lens equation then reduces to the scalar equation

$$\theta_E = \hat{\alpha}(\theta) \frac{D_{ds}}{D_s} = \sqrt{\frac{4GM}{c^2} \frac{D_{ds}}{D_d D_s}} \tag{1.17}$$

where θ_E is the angle that defines the *Einstein ring*. We can use the information about the Einstein ring to estimate the mass of the lens. For an axi-symmetric mass distribution the mean surface mass density inside the Einstein ring ($M/\pi(D_d\theta_E)^2$) is exactly the critical density Σ_{cr}. This means that once the angular diameter and the redshifts of lens and source are measured one may determine the mass inside the Einstein ring:

$$M(< \theta_E) = \Sigma_{cr}\pi(D_d\theta_E)^2 \tag{1.18}$$

Even though we seldom have perfect alignment and therefore do not observe the Einstein ring itself, the positions of multiply imaged sources and arcs resulting from lensed quasar host galaxies can be used to trace an imagined ring and therefore provide a good constraint on the mass of the lens (cf. Kochanek et al. 2001).

1.2.5 Magnification

Gravitational lensing conserves the surface brightness of a source (no photon is destroyed or created by the lensing phenomenon). The flux amplification is therefore simply given by the ratio (magnification) between the solid angle $d\Omega_I$ covered by the lensed image and that of the unlensed source $d\Omega_s$, as represented for a point mass lens in Fig. 1.3. More formally, the lens mapping of an infinitesimally small source is given by the inverse Jacobian matrix. Letting μ being the magnification factor, we have

$$\mu = \frac{d\Omega_I}{d\Omega_s} = \left| det(\frac{\delta\vec{\beta}}{\delta\vec{\theta}}) \right|^{-1} \tag{1.19}$$

which for any source lensed by a circularly symmetric lens becomes

$$\mu = \frac{\theta}{\beta}\frac{d\theta}{d\beta}. \tag{1.20}$$

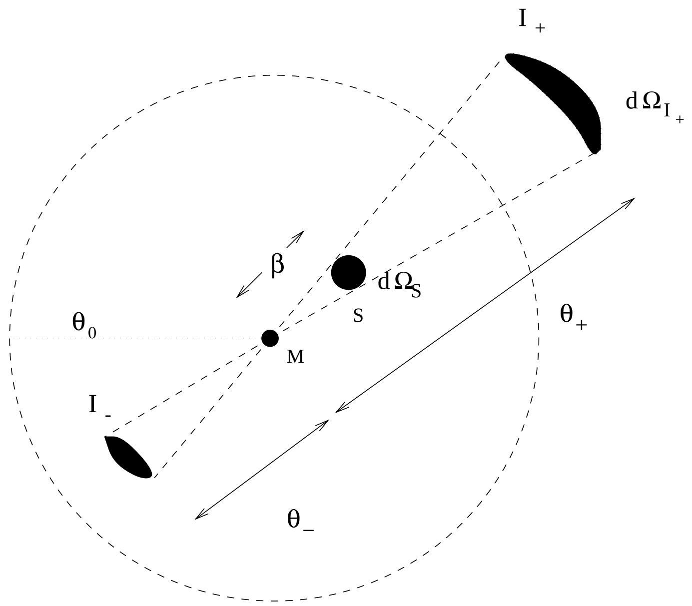

Figure 1.3: Magnified images of a source lensed by a point mass. The dashed circle is the Einstein ring. The solid angle of the source $d\Omega_s$ is magnified in the lens plane to $d\Omega_{I_+}$ and $d\Omega_{I_-}$ for the image with positive and negative magnification.

The regions in the lens plane where the Jacobian determinant has opposite sign describe the different parity of the images and they are separated by critical curves on which the Jacobian vanishes. These curves projected onto the source plane are called caustics, and the number of images changes by two if the source crosses a caustic (see Fig. 1.4). Fig. 1.3 illustrates how two images are formed for a point mass lens (for a lens with finite core there will also be a faint third image close to the lens, this image disappears for a point mass lens). The images correspond to the positive and negative solution of the lens equation for a point mass lens:

$$\theta_\pm = \frac{1}{2}(\beta \pm \sqrt{\beta^2 + 4\theta_E^2}) \tag{1.21}$$

An image outside or inside the Einstein ring is respectively positively or negatively magnified. Negative magnification means that the image has an inversed parity relative to the

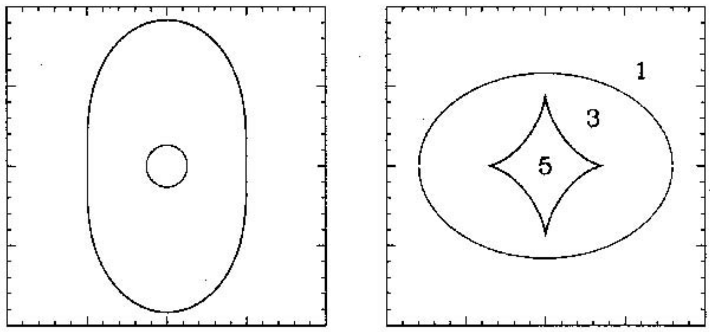

Figure 1.4: Critical curves (left) and caustics (right) for an elliptical lens. The numbers in the right panels identify regions in the source plane that correspond to 1,3 or 5 images, respectively. The smooth lines in the right hand panel are called fold caustics; the tips at which the inner curve two fold caustics connect are called cusp caustics. (Figure from Wambsganss 1998).

source. The net magnification of flux in the two images is obtained by adding the absolute magnifications. We define the *impact parameter* $u = \beta/\theta_E$ as the angular separation of the source from the point mass lens in units of the Einstein angle. The net magnification writes:

$$\mu = |\mu_+| + |\mu_-| = \frac{u^2+2}{u\sqrt{u^2+4}} \tag{1.22}$$

In the case where the source lies exactly on the imaginary projected Einstein radius in the source plane we have $\beta = \theta_E$, $u = 1$ and $\mu = 1.34$. When the source lies inside the Einstein ring the net magnification is $\mu \geq 1.34$ and we have by convention, significant lensing. The cross section for significant lensing is $\pi\theta_E^2$ and is proportional to the mass M (cf. Eq. 1.18).

1.2.6 Microlensing

Lensing by the gravitational field of a galaxy generates lensed quasar images typically separated by a distance of the order of an arcsecond. This phenomenon is called *macrolensing.* Galaxies partly consist of stars and compact objects (black holes, brown dwarfs, planets). Each of these objects also acts as a lens and produces new images of the source (see Fig. 1.5). However, since the image splitting is proportional to the lens mass, this separation is only of the order of a microarcsecond and cannot be resolved. This phenomenon is called *microlensing* and was first discussed by Chang and Refsdal (1979). Although we are unable to resolve the micro-images, microlensing manifests itself through intensity variations in one of the macro-images. This results from the fact that the observer, the lens(es) and the source move relative to each other so that the micro-image configuration changes with time and hence, so does the total magnification. An example of a lensed quasar where several microlensing events have been observed is the quadruple Q2237+0305 (Fig. 1.6). The four quasar images lie behind the lensing galaxy and the optical depth for microlensing is high. The time delay in this system is only of the order of a day so

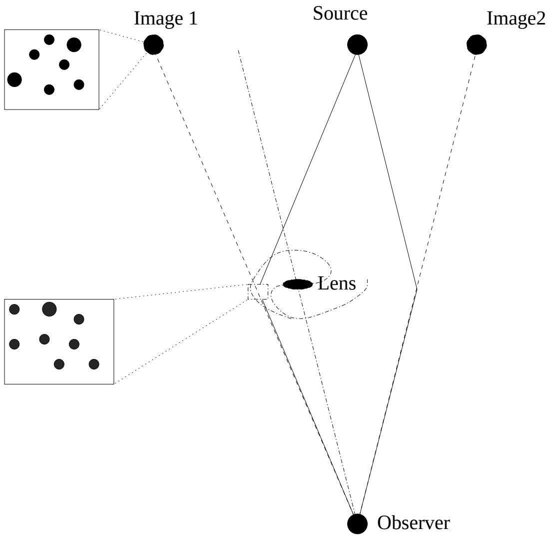

Figure 1.5: Schematic illustration of microlensing by individual stars in the lensing galaxy.

that any variation in brightness on longer time scales must be due to microlensing. Spectacular microlensing variations has been observed in this system by the OGLE (Optical Gravitational Lensing Experiment) group (Wosniak et al. 2000). Their light curves from three years of monitoring are shown in Fig. 1.7. Evidences for microlensing effects have also been detected in several other systems, e.g., QSO 0957+561 (Schild & Smith 1991), B1600+434 (Burud et al. 2000, Koopmans et al. 2000), H1413+017 (Angonin et al., 1990, Hutsemékers 1993, Monier et al. 1998) and HE1104-1805 (Courbin et al. 2000a). The microlensing timescales and amplifications in lensed quasars can be used to constrain the size of the source (quasar) and the lens masses (Wambsganss, Paczyński & Schneider 1990).

Microlensing effects can also be used to search for compact masses in our own Galaxy. Paczyńsky (1986, 1996) was the first to propose a monitoring of millions of stars in the LMC to look for magnifications due to microlensing from so-called *Massive Astrophysical Compact Halo Objects* (MACHOs) in the Galaxy. Huge observational campaigns, (MACHO, EROS and OGLE experiments) have been carried out to look at millions of stars in the LMC and towards the bulge of the Milky Way (Alcock et al. 1993, Aubourg et al. 1993, Udalski et al. 1993).

1.2.7 Measuring the Hubble constant

Sjur Refsdal (1964b) was the first to point out one of the most important applications of gravitational lensing: the determination of the Hubble constant H_0 or equivalently, the Hubble age $\tau_0 = H_0^{-1}$ of our Universe. One way of describing this is to use Fermat's principle (Narayan & Bartelman 1995) [1]. A photon traveling from a distant quasar to

[1]Another approach to describe how the Hubble constant can be derived from gravitational lensing, called the *wavefront method* is described in Refsdal and Surdej (1994).

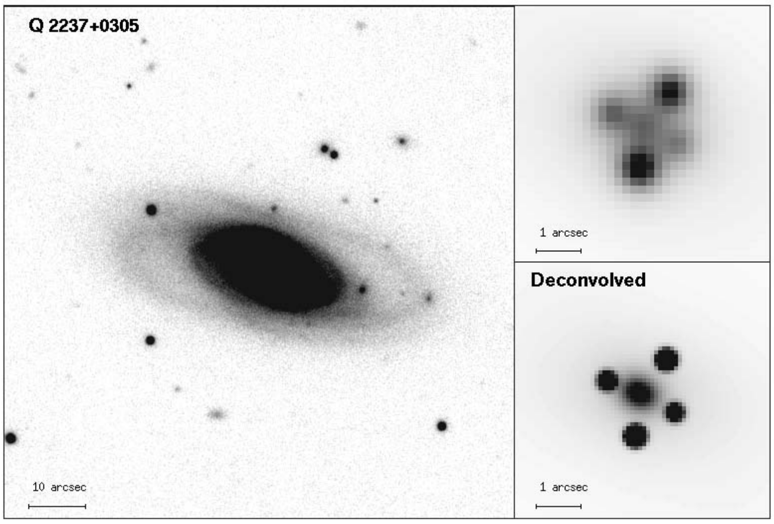

Figure 1.6: [*Left*:] I band image (total exposure time of 2400s) of the field of Q 2237+0305, obtained at the NOT. North is up and East to the left. We see the nearby spiral lensing galaxy ($z = 0.039$). [*Right*:] A zoom of the quadruple lens is displayed at the top and its deconvolved version at the bottom (see Section 2.1 for an explanation of the deconvolution). We see the four images of the lensed quasar ($z = 1.695$) and the central nucleus of the lensing galaxy.

the Milky Way will make a detour around a mass concentration, consistent with Fermat's principle, by the path which takes the least time. In the thin lens approximation the extra travel time τ, due to the gravitational potential of the lens, will be proportional to a two-dimensional lensing potential ψ and can be written:

$$\tau(\vec{\theta},\vec{\beta}) = \tau_{geom} + \tau_{grav} = \frac{1+z_d}{c}\frac{D_d D_s}{D_{ds}}\left(\frac{1}{2}(\vec{\theta}-\vec{\beta})^2 - \psi(\vec{\theta})\right). \quad (1.23)$$

This time delay surface is a function of the image geometry $(\vec{\theta},\vec{\beta})$, the two-dimensional gravitational potential ψ and the angular diameter distances D_d, D_{ds} and D_s. The first part, the geometrical timed delay (τ_{geom}) is proportional to the square of the angular offset between β and θ and reflects the extra traveling distance compared to the unperturbed null geodesic. The second part, the gravitational time delay (τ_{grav}) is the delay due to gravitational potential of the lensing mass, i.e., the speed of light is reduced in a gravitational field. In the case of a circularly symmetric deflector, the source, the lens and the images will lie on a straight line on the sky. Therefore it is sufficient to consider the section along this line of the time delay surface. Fig. 1.8 illustrates the geometrical and gravitational time delays for this case. The top panel shows τ_{geom} for a slightly offset source. The curve is a parabola centered on the position of the source. The central panel displays the τ_{grav} for an isothermal sphere mass distribution with a softened core. This curve is centered on the lens. The bottom panel shows the total time delay. According to Fermat's principle, lensed images will occur at stationary points of τ. For the case illustrated in Fig. 1.8 there are three stationary points marked by dots, and the corresponding values of θ give the image positions.

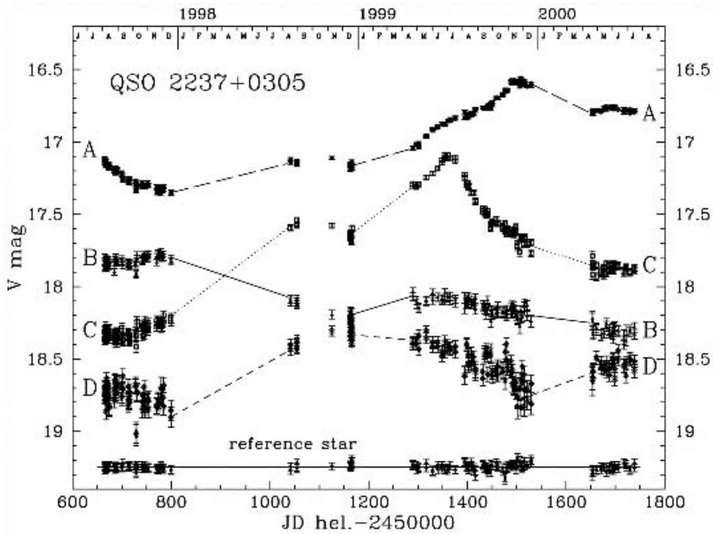

Figure 1.7: Light curve of QSO 2237+0305. A total of 212 photometric points are shown for each of the four quasar images AD, with the lines connecting the observing seasons. (Figure from Wosniak et al. 2000).

The height difference between two stationary points on $\tau(\theta, \beta)$ gives the relative time delay between corresponding images. Any variability in the source is observed first in the image corresponding to the lowest point on the surface, followed by extrema located at successively larger values of τ. In Fig. 1.8 we see that the first image to vary is the one that is farthest away from the center of the lens. Although this example is for a circularly symmetric mass profile, this property usually carries over even for lenses that are not perfectly circular.

The curvature of $\tau(\theta, \beta)$ indicates the magnification of the images. When the curvature along one coordinate direction is small, the image is strongly magnified along that direction, while if $\tau(\theta, \beta)$ has a large curvature the magnification is small. The time delay surface also has several other useful properties, as described by Narayan & Bartelman (1995).

Now how can this be used to measure H_0 ? We see from (Eq. 1.23) that the time delay depends on angular-diameter distances which themselves depend on H_0 and the redshift z_i of object i. The angular diameter distance D_{ij} from object i to j is defined as

$$D_{ij} = \frac{2c}{H_0} \frac{(1 - 2q_0)(G_i - G_j) + (G_i G_j^2 - G_i^2 G_j)}{(2q_0)^2 (1 + z_i)(1 + z_j)^2} \qquad G_i = \sqrt{1 + 2q_0 z_i} \tag{1.24}$$

where q_0 is the "deceleration parameter" of the Universe which in the case of zero cosmological constant is equal to $\frac{1}{2}\Omega_m$. If the gravitational potential and the source position are known, we can solve the lens equation (Eq. 1.13) for the image positions $\vec{\theta_A}$ and $\vec{\theta_B}$. Then with a measured time delay $\tau_A - \tau_B$ and measured redshifts of source and lens we obtain an angular diameter distance from Eq. 1.23 and hence an estimate of H_0. The angular diameter distance does not only depend on H_0 and on the redshifts, but also on

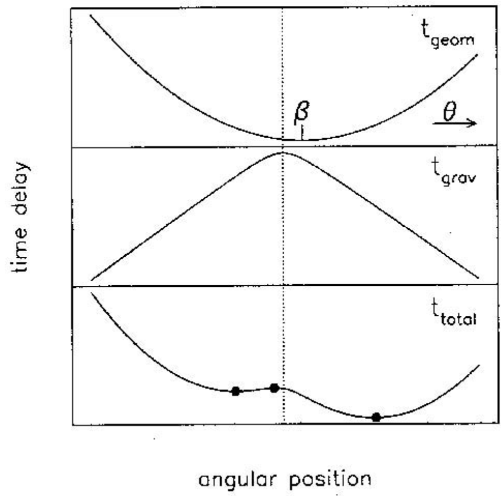

Figure 1.8: Geometric (top), gravitational (middle) and total time delay of a circularly symmetric lens for a source that is slightly offset from the symmetry axis. The dotted line shows the location of the center of the lens, and β shows the position of the source. Images are located at points where the total time delay function is stationary. The image positions are marked with dots in the bottom panel. (Figure from Narayan & Bartelman (1995)).

the cosmological density parameters. For quasars at small redshifts this will have a negligible effect, but for large redshifts the chosen values for Ω_m and Ω_Λ must be considered. Schematically we can write:

$$\begin{aligned} timedelay &= H_0^{-1} < image\ separation >^2 \\ &\times < weak\ dependence\ on\ z_{lens},\ z_{qso}\ and\ cosmology > \\ &\times < lens\ mass\ distribution - dependent\ factor > \end{aligned} \tag{1.25}$$

In practice, the challenging parts for a determination of H_0 from gravitational lensing are (i) a measurement of the time delay between two lensed images and (ii) a model for the two-dimensional gravitational potential. The first can be measured on light curves obtained from long-term monitoring of the targets. The latter can in principle be determined from the deflection and distortions of the observed images. I will in the following sections describe how such H_0 determinations are being conducted.

1.2.8 Constraints on Ω_m and Ω_Λ from gravitational lensing

Gravitational lensing does not only depend on H_0 but also on the cosmological density parameters. It therefore offers a means of determining Ω_m and Ω_Λ by comparing expectations from different models with observations. In general one can derive constraints on Ω_m and Ω_Λ from gravitational lensing when there is more than one source plane involved (e.g. Golse et al. 2000). This is the case in most examples of weak lensing and cluster lensing. Another possibility is provided by higher-order effects in measuring H_0 through lensed quasars. The time delay is inversely proportional to H_0 and as can be seen in Eq. 1.24, there is also a weak, non-linear dependence on Ω_m and Ω_Λ. Finally, statistical analysis of gravitational lens surveys provides a potentially powerful method of measuring the cosmological parameters. The volume element as a function of redshift ($\frac{dV}{dz}$) depends on the cosmological model. If one fixes the space density of galaxies at $z = 0$, varying Ω_m and Ω_Λ can vary the number of potential lens galaxies per redshift interval at higher redshifts. Falco et al. (1998) obtain $\Omega_\Lambda < 0.62$ for a flat Universe ($k = 0$) using this method. Preliminary results from the CLASS (Cosmic Lens All-Sky Survey) give $0.1 < \Omega_\Lambda < 0.65$, thus favouring a Universe with a positive cosmological constant (Helbig 2000).

1.3 H_0 from lensed QSOs: advantages and limitations

The advantages of using gravitationally lensed quasars to determine H_0 are (i) the measurements are at large redshift which avoid confusion of peculiar velocities with global expansion; (ii) it is a one-shot procedure which avoids propagation of errors along the "distance ladder"; (iii) the methodology is grounded on well understood physics (general relativity in the weak field limit) and not on empirical models and calibrations.

When the first lensed quasar Q0957+561 was discovered (Walsh et al. 1979) it was immediately monitored both at radio and optical wavelengths with the aim of measuring its time delay and to determine the Hubble constant. However there were for many years a controversy between two different time delay estimates by different groups (Pelt et al. 1996; Press et al., 1992; Schild & Thomson 1995; Vanderriest et al., 1989). Only in 1997 did Kundić et al. succeed in pinning down the time delay to 417±3 days. Moreover, once the time delay is well determined, an accurate model of the mass distribution is needed to derive an H_0 estimate, which also turned out challenging for Q0957+561. A cluster of galaxies has to be included in the gravitational potential, which introduces a degeneracy in the value of H_0. Attempts to resolve this degeneracy were conducted (i) by measurements of the velocity dispersion of the central galaxy (Falco et al. 1991; Grogin & Narayan 1996) and (ii) by estimating the cluster mass from weak lensing analysis (Fischer et al. 1997). An H_0 estimate of 64 ± 13 kms^{-1}Mpc^{-1} was obtained by Kundić et al. (1997) using the mass model from Grogin & Narayan (1996).

This example of the first well-studied lensed quasar system clearly illustrates that neither an accurate time delay measurement, nor a well constrained model of the gravitational potential are trivial to obtain. Both, and in particular the latter, tend to introduce systematic errors in the inferred values of H_0.

1.3.1 Time delay measurements

Measuring a time delay is, for several reasons, not a trivial task. Intensive monitoring of multiply imaged quasars during the last years has shown that the typical difference in the travel time from lensed quasar images is of the order of $10^{-11}/H_0$ and is measured in weeks or months. Furthermore, a typical intrinsic quasar variation on such a timescale is of the order of 10% (although some quasars are atypically variable and others atypically stable). Consequently, both long-term monitoring, on time spans of years, and high photometric accuracy are needed to measure time delays. In addition, most targets lie below the horizon up to several months a year which introduces gaps in the light curves. Other objects are so faint that they can only be observed during dark time, or they have very small angular separation requiring excellent seeing conditions.

Microlensing by compact objects along the line of sight, (e.g., individual stars in the lens galaxy) is yet another obstacle to time delay measurements, implying that variations in lensed quasars may not only be due to intrinsic fluctuations of the quasar. The microlensing signal itself, depending on its timescale and amplitude, can be used to constrain (i) the size of the continuum and the line emitting region in the quasar, and (ii) the distribution of compact matter in the lens galaxy (Paczyński 1986, Kayser et al. 1986). However, as long as these external variations are not perfectly distinguished from the intrinsic variations, microlensing remains unwanted noise for time delay measurements.

After the long and debated time delay measurement of Q0957+561 the enthusiasm for H_0 determination from gravitational lensing faded out for several years. However, in 1997, Schechter et al. very impressively measured the time delays in the quadruple lens system PG1115+080. This measurement inspired many subsequent monitoring campaigns. Considerable effort has been invested during the last years and time delays have now been measured for 10 systems (including the results in this thesis), thanks to new techniques for observations and data analysis and to flexible scheduling of several telescopes.

1.3.2 Modelling the gravitational potential

Analytical models

Models of the gravitational potential are often based on isothermal galaxies, since such models are simple and consistent with individual lenses, lens statistics, stellar dynamics and X-ray galaxies (Witt et al. 2000). The simplest model of such galaxies is the singular isothermal sphere (SIS). In this model, the stars and other mass components in the galaxy are considered to behave like particles of an ideal gas and this "stellar gas" is assumed isothermal. In thermal equilibrium, the temperature is related to the one-dimensional velocity dispersion σ_v of the stars. It can be demonstrated (e.g., Narayan & Bartelman 1995) that the projected surface mass distribution in the lens plane for a SIS is:

$$\Sigma(\xi) = \frac{\sigma_v^2}{2G}\frac{1}{\xi} \tag{1.26}$$

Referring to Eq. 1.10, one obtains the deflecting angle:

$$\hat{\alpha}(\xi) = 4\pi\frac{\sigma_v^2}{c^2} \tag{1.27}$$

which is independent of ξ, the distance from the centre of the two-dimensional profile. Witt et al. (2000) systematically used simple analytic isothermal lens models to infer H_0 from systems with a measured time delay. They find that even with moderate ellipticities in the galaxy the time delay predictions are well approximated by the isothermal models, with the exception of close image pairs since these are near the lensing critical curve and hence more sensitive to the particular model.

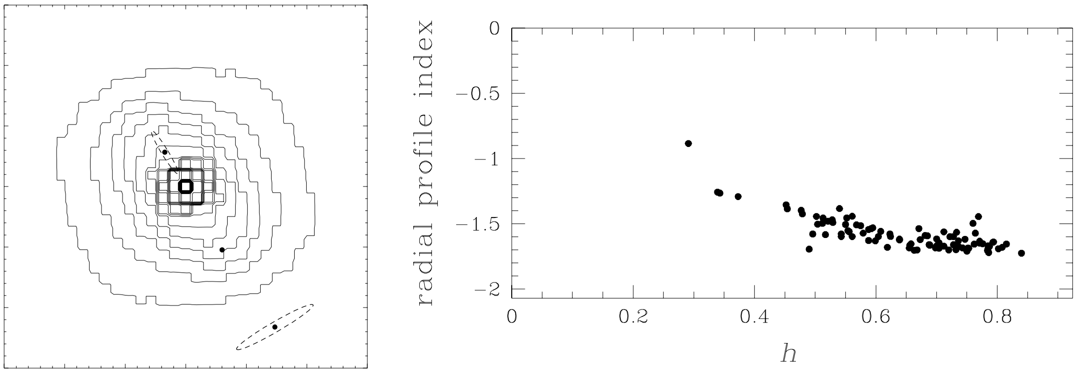

Figure 1.9: *Left*: Pixelated density contours of HE2149-2745 with a cosmology $\Omega = 0.3$, $\lambda = 0.7$. The dashed ellipses around the quasar images represent the magnification matrix, i.e., the axes are proportional to the eigenvalues and the orientation corresponds to the eigenvectors. The spot between the quasar images is the position of the lensed source. *Right*: Radial index profile vs. H_0 for one hundred different non-parametric models. The median value for H_0 is 65kms^{-1}Mpc^{-1}.

The isothermal sphere model is commonly generalized to include solutions with finite cores, which are more realistic for spiral galaxies, and for slightly elliptical solutions. A commonly used analytic model is the truncated "Pseudo-Isothermal-Elliptical-Mass-Distribution" (PIEMD) (Kneib et al. 1996, Kassiola & Kovner 1993). Truncated PIEMDs are elliptical mass distributions smoothly truncated at a radius r_{cut}. For radius smaller (respectively larger) than r_{cut}, the projected surface mass density profile is varying as r^{-1} (respectively r^{-3}). The interest of such profile is their ability of characterizing any ellipticity in the mass distribution as well as having a total finite mass.

Free form lens models

Even if analytical mass models such as the isothermal models can reproduce the image properties, many argue that it is also necessary to use general galaxy mass distributions, not restricted to any particular form, in order to explore all the classes of models and to obtain the true uncertainty in H_0. One way to explore such a general model is to build a model from a large number of small components, e.g., pixels. In a pixelated galaxy, each pixel is an independent mass element (Saha & Williams 1997, Williams & Saha 2000). Fig. 1.9 (left) shows the pixelated reconstruction of HE2149-2745 (cf. Section 8.2.3). The derived H_0 value is plotted versus to the profile slope of the lens galaxy in Fig. 1.9 (right) and the median value of H_0 is 65 km s^{-1}Mpc^{-1} . The mass profile index in the figure is defined as $ind(r) = dln\kappa/dln\theta$ (Williams & Saha 2000). An isothermal profile has $ind(r) = -1$ and, from the figure, yields $H_0 \sim 30$ km s^{-1}Mpc^{-1} with this method. Steeper mass profiles give decreasing values of $ind(r)$.

1.3.3 Model degeneracies and the need for numerous H_0 determinations

In many systems, several mass models reproduce the observed image configuration and these degeneracies lead to systematic errors in H_0 estimates. Often such a degeneracy is caused by a cluster of galaxies inducing a shear in the gravitational potential. The shear is characterized by a direction (determined by the centre of the cluster relative to the lensed system) and a strength γ. A group of galaxies that extends beyond the lens projects a sheet of uniform surface mass density onto it with the potential $\psi_{sheet} = \kappa\theta^2$ (κ is the dimensionless surface density cf. 1.15). Adding a mass sheet to a lens produces an image configuration which is consistent with a scaled version of the original lens potential. The time delays predicted by this scaled potential are longer than those predicted by the actual lens plus sheet potential by a factor $1/(1-\kappa)$. The relative magnification however remains unchanged and unless one knows the intrinsic size (or luminosity) of the lensed object one cannot tell from the observed deflections, distortions or delays whether a mass sheet is present or not (Saha 2000).

The mass-sheet degeneracy due to shear from a cluster of galaxies can be solved by independent estimates of the cluster mass surface density, such as velocity dispersion measurements (Angonin-Willaime et al. 1994) and weak lensing analysis (Fischer et al. 1997). However, one should keep in mind that there is also a degeneracy in the measured velocity dispersion in the way that similar velocity dispersion measurements can be obtained for very different mass profiles (cf. Saha (2000), Romanowsky & Kochanek (1999)).

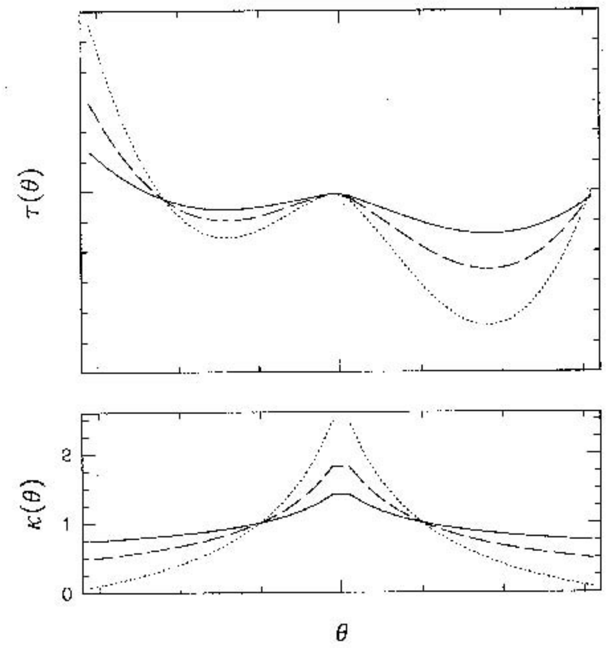

Figure 1.10: Illustration of the degeneracy in the mass modelling. The arrival time (top panel) shows three stationary points. Surface densities are shown in the lower panel. The dashed curves correspond to a non-singular isothermal lens. Stretching the time scale amounts to making lens profile steeper (dotted curves) and shrinking the time scale amounts to making the lens profile shallower (solid curves). (Figure from Saha 2000.)

Degeneracies are also present in the mass profiles of a single lensing galaxy. In a circularly symmetric mass model we will have a deflection of the type:

$$\hat{\alpha} \propto |\xi|^{\epsilon - 1} \tag{1.28}$$

where ϵ is a parameter describing the mass profile of the lens. A SIS profile is obtained for $\epsilon = 1$, and a point mass lens for $\epsilon = 0$. In many systems both isothermal and point mass models can reproduce the image configuration within the measurement errors. Fig. 1.10 displays the time delay surface for different mass profiles. A stretching of the time delays surface occurs for steeper mass profiles, but the image configuration remains unchanged. Only in a few lensed systems can the radial mass profiles be constrained by the image configuration.

Whereas some seek a few "golden" lenses outstandingly constrained by their image configuration, others are willing to take advantage of a "prior" information obtained from nearby galaxies, which allows them to work with images that are less constrained by their configuration. Rusin & Ma (2000) point out that the absence of a third image in lensed double quasar systems can be used to constrain the mass profile. The results from Witt et al. (2000), that isothermal mass models yield coherent results for most systems, suggest that galaxies have a common density profile. If such is the case, H_0 estimates obtained by applying isothermal models to numerous lenses will show little scatter. Clearly more systems and more and better data are required to better understand the errors and to confirm whether or not galaxies have common mass profiles.

1.3.4 Using time delays to constrain mass models

Given the large uncertainties in the mass models of certain systems, it can be argued that they are unsuited for H_0 determination. However, time delays will provide important constraints on the mass distribution in the lensing galaxies once H_0 is known from other methods. In this point of view, systems with a complex gravitational potential e.g., spiral lensing galaxies and clusters of galaxies, are particularly interesting to study in order to learn more about how dark matter is distributed. We should therefore keep in mind that although a system may seem to be a poor candidate to determine H_0 it is important to measure its time delay for the study of the mass profile.

Since we do not yet have an exact value of H_0 I will in this work concentrate on the use of time delays to determine H_0. However, given the rapid progress in new measurements and methods, there are reasons to believe that we will soon know the value of H_0 to a few percent. I therefore also stress the importance of the use of time delays as a tool to study mass distributions and in particular to probe dark matter in the Universe.

Chapter 2

Methods for data analysis

2.1 High resolution imaging and spectroscopy by deconvolution.

Optimally constraining a mass model requires an accurate geometry of the lensed system, and a good understanding of the light distribution of the lensing galaxy(ies). Consequently, the detailed study of individual systems requires high resolution imaging, which has been obtained both by the CASTLEs group using the NICMOS (Near Infrared Camera and Multi Object Spectrometer) on HST (Hubble Space Telescope) (Kochanek et al.), and through deconvolution of ground based observations using the MCS deconvolution technique (Magain, Courbin & Sohy 1998). Given the central role played by this technique in my research I briefly describe its basic principles.

On the basis of an observation $d(\vec{x})$ and of the instrumental profile $t(\vec{x})$ (total Point Spread Function, PSF), a deconvolution consists in inverting the equation

$$d(\vec{x}) = t(\vec{x}) * f(\vec{x}) + n(\vec{x}) \tag{2.1}$$

in order to recover the signal from the source $f(\vec{x})$. Being an inverse problem, deconvolution is also an ill-posed problem, and no unique solution can be found, especially in the presence of noise $n(\vec{x})$ which is unknown. Many light distributions are, after convolution with the Point Spread Function (PSF), compatible within the error bars with the observed image. Therefore, regularization techniques have to be used in order to select a plausible solution amongst the family of possible ones and a large variety of deconvolution methods have been proposed, depending on the way this particular solution is chosen, e.g., the maximum entropy method (Narayan & Nityananda 1986, Skilling & Bryan 1984), the Richardson-Lucy method (Richardson 1972, Lucy 1974) and the MCS method (Magain, Courbin & Sohy 1998).

The MCS method is based on the principle that the resolution of a deconvolved image must be compatible with its sampling, and thus limited by the Nyquist frequency. The PSF of the deconvolved image $r(\vec{x})$ is chosen by the user so that it obeys the sampling theorem, and a deconvolved point source will have a shape with $r(\vec{x})$, generally chosen as a Gaussian distribution. The deconvolution should therefore not be performed with the observed PSF $t(\vec{x})$, but a narrower one $s(\vec{x})$ so that:

$$t(\vec{x}) = s(\vec{x}) * r(\vec{x}) \tag{2.2}$$

The deconvolved image thus has an *improved* but not *infinite* resolution.

Since the profile of a point source in the deconvolved image is known and chosen by the user, the deconvolved image, $f(\vec{x})$, can be decomposed into a number M of point sources, for which the program returns positions $\vec{c}_k$ and intensities a_k, plus a deconvolved numerical image of all the extended sources $h(\vec{x})$.

$$f(\vec{x}) = h(\vec{x}) + \sum_{k=1}^{M} a_k\, r(\vec{x} - \vec{c}_k) \tag{2.3}$$

An analytical De Vaucouleurs, or an exponential disk galaxy profile can also be included in order to determine morphological parameters of galaxies in the fields, e.g., lensing galaxies.

In the "background" $h(\vec{x})$, smoothing is imposed at the length scale of $r(\vec{x})$. This means that all frequencies higher than the chosen resolution are smoothed.

Deconvolving a sampled image will finally result in minimizing the following function (see Magain et al. 1998):

$$\begin{aligned} F &= \sum_{i=1}^{N} \frac{\lambda}{\sigma_i^2} \left[\sum_{j=1}^{N} s_{ij} \left(h_j + \sum_{k=1}^{M} a_k r(\vec{x}_j - \vec{c}_k) \right) - d_i \right]_i^2 \\ &+ \sum_{i=1}^{N} \left[h_i - \sum_{j=1}^{N} r_{ij} h_j \right]^2 \end{aligned} \tag{2.4}$$

where N is the number of pixels (sampling points), d_i represents the intensity of the data image at pixel i and σ_i is the error in the pixel i. A Lagrange smoothing parameter λ adjusts the value of the χ^2 so that the model matches the data in a statistically correct way. The quality of the results is checked from residual maps. These maps represent the residual in each pixel, i.e., the match between the deconvolved model image (reconvolved with the PSF) and the data.

2.1.1 Optimal image combination

The MCS algorithm can be used to deconvolve a single stacked image or to simultaneously deconvolve several individual images of a field. The advantage of the latter is to derive an optimally constrained deconvolved frame which is simultaneously compatible with several images of a given object. From n data frames, each with its own PSF ($s_1(\vec{x})$, $s_2(\vec{x})$, ... $s_n(\vec{x})$) we obtain n deconvolved model images. The extended sources and the positions of the point sources are forced to be equal in all n images. This means that the total signal-to-noise (S/N) from all the frames will be used to constrain these parameters. The intensity of the point sources are on the other hand allowed to vary from image to image.

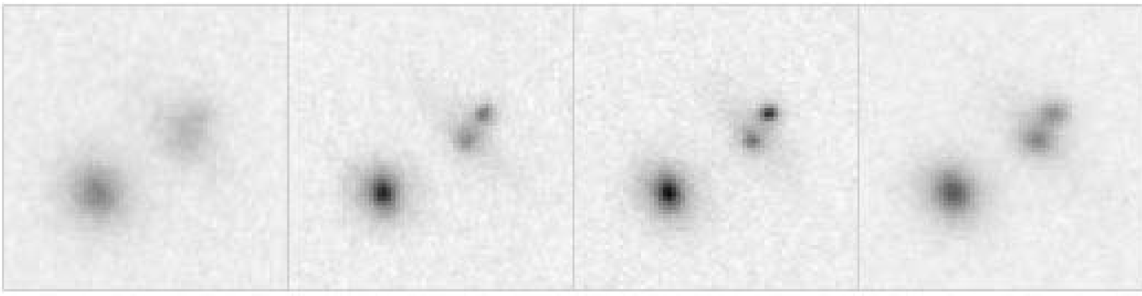

Figure 2.1: Data of the lensed quasar B1600+434 obtained at the NOT. The four images were obtained on four different nights under different observing conditions.

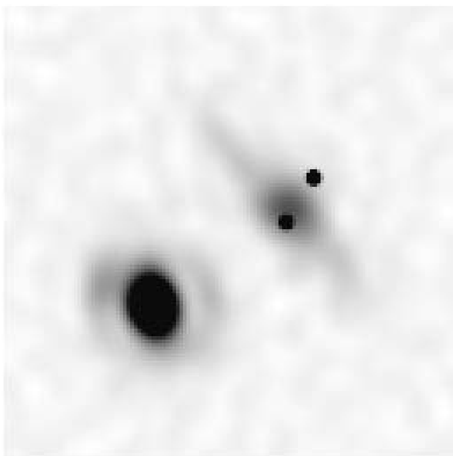

Figure 2.2: Result image obtained by simultaneous deconvolution of 44 frames of B1600+434 obtained on different nights at the NOT.

The minimization performed during the simultaneous deconvolution can then be expressed as follows:

$$
\begin{aligned}
F \; = \; & \sum_{i=1}^{N} \frac{\lambda_1}{\sigma_{1,i}^2} \left[\sum_{j=1}^{N} s_{1,ij} \left(\alpha_1 h(\vec{x_j} + \vec{\delta_1}) + \beta_1 + \sum_{k=1}^{M} a_{1,k} r(\vec{x}_j - \vec{c}_k + \vec{\delta}_1) \right) - d_{1,i} \right]_i^2 \\
+ \; & \sum_{i=1}^{N} \frac{\lambda_2}{\sigma_{2,i}^2} \left[\sum_{j=1}^{N} s_{2,ij} \left(\alpha_2 h(\vec{x_j} + \vec{\delta_2}) + \beta_2 + \sum_{k=1}^{M} a_{2,k} r(\vec{x}_j - \vec{c}_k + \vec{\delta}_2) \right) - d_{2,i} \right]_i^2 \\
& \vdots \\
+ \; & \sum_{i=1}^{N} \frac{\lambda_n}{\sigma_{n,i}^2} \left[\sum_{j=1}^{N} s_{n,ij} \left(\alpha_n h(\vec{x_j} + \vec{\delta_n}) + \beta_n + \sum_{k=1}^{M} a_{n,k} r(\vec{x}_j - \vec{c}_k + \vec{\delta}_n) \right) - d_{n,i} \right]_i^2 \\
+ \; & \sum_{i=1}^{N} \left[h_i - \sum_{j=1}^{N} r_{ij} h_j \right]^2
\end{aligned}
\tag{2.5}
$$

Three new parameters (α, β and δ) are included when deconvolving several frames. The "background" h, common for all the images, is for each image adjusted with a multiplicative factor α, and an additive term β. The factor α is introduced in order to correct for effects due to different exposure times or varying tranparency of the atmosphere. The additive constant β can correct for errors in the sky-subtraction. A shift δ in position may occur between different exposures, which is often recommended in order to (i) better remove cosmic rays or bad pixels on the frames and (ii) to improve the sampling of the data. The latter is obtained by a technique known as "drizzling" and is commonly used on HST-images to improve the sampling of the combined frames compared to the individual frames (Hook 1994). The basic idea is that if an object is centered on different places on the detector we can measure its intensity on a grid of "virtual" pixels with smaller sampling steps than the real CCD pixels. This technique is also implemented in the deconvolution method. The simultaneous deconvolution of many dithered frames thus results in a more accurate decomposition of the data than the deconvolution of one single combined frame. The technique is therefore well suited to detect underlying diffuse objects such as lensing galaxies (Burud et al. 1998) and QSO host galaxies (Fynbo et al. 2000). Moreover, by deconvolving simultaneously all the images of a given field at different epochs we get both the time dependent light curve of the point sources and a high S/N image of the extended sources as output of the algorithm. Hence it is possible to derive precise light curves of variable point sources that are superimposed on a complicated background, e.g., the lensed images of QSOs, supernovae or optical transients of gamma ray bursts.

2.1.2 Spectroscopy

The MCS algorithm has also been extended to spectral deconvolution (Courbin, Magain, Sohy & Kirkove 2000). High spatial resolution spectra are often needed to determine the redshift of the lensing galaxies. Redshift estimates for lens galaxies are often limited by observational difficulties arising from the fact that the light from these galaxies is often heavily blended with the light from one of the QSO images, the latter generally being several magnitudes brighter. Using spatial deconvolution of spectra, it is possible to separate the galaxy spectrum from the quasar spectra and hence measure the lens redshift (see Courbin et al. 2000a for a successful application of this technique).

2.2 Time series analysis

Advanced methods for analysing light curves are needed in order to measure an accurate time delay from quasar light curves. Several methods have been developed for this purpose (e.g., Pelt 1996, Press et al. 1992, Pijpers 1997). Each of these methods has its advantages and drawbacks. We have developed a new method for times series analysis which has the advantage of being simple and easy to use. In the next chapter it is shown that this methods works well both on simulated light curves and a real data set. Moreover, it is clear that by running the method in an iterative way we are able to correct for high order microlensing effects in the light curves. This is a considerable advantage since microlensing effects seem to be frequent in optical light curves form lensed quasars.

2.3 Article presenting a new method to estimate time delays

A novel approach for extracting time-delays from lightcurves of lensed quasar images

I. Burud, P. Magain, S. Sohy, J. Hjorth

Submitted to Astronomy & Astrophysics

Astronomy & Astrophysics manuscript no.
(will be inserted by hand later)

A novel approach for extracting time-delays from lightcurves of lensed quasar images

Ingunn Burud[1], Pierre Magain[1], Sandrine Sohy[1], and Jens Hjorth[2]

[1] Institut d'Astrophysique et de Géophysique, Université de Liège, Avenue de Cointe 5, B–4000 Liège, Belgium
e-mail: burud@astro.ulg.ac.be, magain@astro.ulg.ac.be, sohy@astro.ulg.ac.be

[2] Astronomical Observatory, University of Copenhagen, Juliane Maries Vej 30, DK–2100 Copenhagen Ø, Denmark
e-mail: jens@astro.ku.dk

Abstract. We present a new method to estimate time delays from light curves of lensed quasars. The method is based on χ^2 minimization between the data and a numerical model light curve. A linear variation can be included in order to correct for slow long-term microlensing effects in one of the lensed images. An iterative version of the method can be applied in order to correct for higher order microlensing effects. The method is tested on simulated light curves. When higher order microlensing effects are present the time delay is best constrained with the iterative method. Analysis of the a published data set for the lensed double Q 0957+561 yields results in agreement with other published estimates.

Key words. Methods: data analysis – Gravitational lensing

1. Introduction

The time delay between light rays from gravitationally lensed quasar images is a measurable parameter directly related to the gravitational potential and to the Hubble constant H_0 (Refsdal 1964). Accurate time delays obtained from multiply lensed QSOs can hence be used i) to determine H_0 providing that the lens mass distribution is known, or ii) to constrain the mass distribution in a given lens, once H_0 has been determined from other methods (or other lensed QSO systems). Much effort has therefore been devoted to observations of lensed QSOs during the last years, and in particular to the photometric monitoring of lensed QSO images.

Measuring the time delay between the images of lensed quasars is, for several reasons, not a trivial task. First it requires regular monitoring of a target over a long period (substantially longer than the time delay). Second, the sampling is crucial and has to be determined on basis of the intrinsic variations in the quasar and the estimated time delay. Third, most objects are not observable during the whole year, i.e., they will be below the horizon for certain periods. Fourth, there are nights with bad weather conditions when no data are obtained. Finally, variations in lensed quasars may not only be due to intrinsic fluctuations of the quasar, but also to microlensing by compact objects along the line of sight. Such a microlensing signal, depending on its timescale and amplitude, can be used to constrain the size of the continuum and the line emitting regions in the quasar, and the distribution of compact matter in the lens galaxy (Paczyński 1986, Kayser et al. 1986). However, as long as these external variations are not clearly distinguished from the intrinsic variations, microlensing remains unwanted noise for time delay measurements. For these reasons, light curves are often poorly sampled and advanced statistical methods have to be used to measure the time delays.

We have developed a method based on χ^2 minimization of the data and a numerical model light curve. The aim was to develop a method based on simple principles, and to be able to properly detect and correct for possible microlensing effects. It has already been successfully applied to several time delay measurements (Burud et al. 2000; Hjorth et al. 2001). In this paper we will present the principles of the algorithm (Sect. 2) apply it to various simulated light curves (Sect. 3) and to a public dataset of QSO 0957+561 from Serra-Ricart et al. (1999) (Sect. 4).

2. Method

Let us assume that we have light curves for two images, A and B, of a lensed quasar. There are N data points in each of the time dependent light curves $a(t)$ and $b(t)$ with measurement errors σ_a and σ_b. The two curves are identical except for a shift in time, Δt, and in magnitude, Δm. It is therefore possible to model the two curves with one model curve $g(t)$, and the parameters representing the

Send offprint requests to: I. Burud

time delay and the magnitude shift. In some cases the light from one or both of the images may be microlensed by individual stars in the lensing galaxy. Except for the cases of high amplification events, which are of short duration, microlensing effects are often slow variations that can be modeled to first order as a linear variation with slope α.

As model curve we choose an arbitrary curve with a fixed number of equally spaced sampling points, M. This model may be χ^2 minimized to the two observed light curves. The minimization is done only for the N observed data points. In this way only the model curve is interpolated and not the data. We thus minimize the following function:

$$\mathcal{F} = \sum_{i=1}^{N} \left[\frac{a(t_i) - g(t_i)}{\sigma_{a_i}}\right]^2 + \sum_{i=1}^{N} \left[\frac{(b(t_i - \Delta t) - (\Delta m + \alpha t_i)) - g(t_i)}{\sigma_{b_i}}\right]^2 \quad (1)$$

Since intrinsic quasar variations are continuous in time, we avoid discontinuities in the model curve $g(t)$ by adding a smoothing term to the function we wish to minimize. More specifically, we force the model to be smooth on a certain length scale τ by minimizing the square of the difference between the original model and the same model convolved with a Gaussian r whose Full Width at Half Maximum (FWHM) is τ. In this way, all the epochs without data points are smoothed out on the model curve so that gaps in the observed light curves will not contribute significantly to the result. The smoothing term is multiplied by a Lagrange parameter λ. This parameter can be chosen so that the model curve matches the data correctly in a statistical sense (i.e., we get the correct χ^2). In practice however, excessive smoothing will prevent the minimization from converging. Therefore the smoothest possible solution which allows the minimization to converge is usually adopted.

A weight W_i, is given to each data point in order to take into account the fact that the data points are unequally spaced in time. This weight can be expressed as For a data point at a time t_i we calculate the relative distance $t_i - t_j$ to all the other points in the curve. A Gaussian function with a FWHM= $2\sqrt{2ln(2)}\tau_2$ chosen by the user is centered at t_i. The sum of the ordinates of the Gaussian for each of the points t_j will give the weight for the point t_i. The expression of W_i can be written:

$$W_i = \frac{1}{\sum_{j=1}^{N} exp(-\frac{t_i - t_j}{\tau_2})^2} \quad (2)$$

The weight is normalised so that the maximum allowed weight for a data point is 1, and this will occur only when one point is present within the time interval defined by τ_2. In this way, isolated points in the light curve will be highly weighted whereas in a cluster of nearby points, each of the individual points will have a lower weight. The ideal choice of τ_2 is the approximate time scale of variations in the quasar. For some systems this time scale will be long, e.g., several hundred days, for other systems it can be shorter e.g., 50 days. We can now write the final function to be minimized:

$$\mathcal{F} = \sum_{i=1}^{N} W_i \left[\frac{a(t_i) - g(t_i)}{\sigma_{a_i}}\right]^2 + \sum_{i=1}^{N} W_i \left[\frac{(b(t_i - \Delta t) - (\Delta m + \alpha t)) - g(t_i)}{\sigma_{b_i}}\right]^2 + \lambda \sum_{i=1}^{M} [g(t_i) - [r * g](t_i)]^2 \quad (3)$$

where $r * g$ signifies a convolution between r and g.

2.1. Microlensing effects and iterative version of the algorithm

Slow microlensing variations in one of the light curves are modeled as a linear term with the parameter α. If higher order variations are present we can use the method in an iterative way. This is done by splitting the light curves into several parts and analyzing them separately. The χ^2 method is applied to determine the amount of linear external variations (α) for each separate part and for a range of input time delay values. First we run the programme with the first time delay dt_1 in the chosen range and we estimate α in each of the separate parts. We then correct each part with the corresponding α and add the parts back together in order to obtain a set of microlensing-corrected light curves for the given input time delay dt_1. We can now run the χ^2 method to measure the time delay for these "corrected" curves. This procedure is repeated for all the input time delay values $dt_2, dt_3, ... dt_n$ in the range to be studied. We finally obtain a time delay measurement for each of the n input values, and all these measurements will generally converge towards the real time delay value.

3. Time delay measurement on simulated light curves

3.1. Data simulations

We apply the method to simulated light curves in order to understand and estimate the errors on the measured values. Various real quasar light curves were used as models for typical time variations and sampling of data points. The measurement errors in the curves represent simulated photon noise errors, so that the faint component will have larger errors than the bright one. We present the results from two sets of simulated light curves. The first set (1a, b and c in Table 1) consists of two curves, A and B, each of 60 points, dispersed over a time interval of 2 years (see Fig. 1 (top) and 2 (top)). The B curve is shifted by 145 days in time and has a magnitude offset of 1.95 mag. In set 1b we have added a slow linear time dependent variation with a slope α (Eq. 3) in the B curve in order to simulate long-time-scale microlensing effects (Fig. 1 middle). A higher order microlensing variation ($\alpha t + \beta t^2$) is added to the B curve in set 1c (Fig. 1 bottom). In the second set (2a, b, and c) we have simulated another kind of intrinsic variation and sampling. The curves span an interval of two years and they have 36 data points each. The time delay is 110 days and the magnitude offset is 0.67 mag (see Fig. 3 top). In sets 2b and c, we added linear (b) and higher order (c) variations in the A curve (see Fig. 1 middle and bottom).

3.2. Time delay measurements

The χ^2 algorithm was applied to all the simulated sets of light curves. The fit was performed several times in order to check for the influence of various parameters such as: (i) the number of data points in the model curve (M in Eq. 3), (ii) the FWHM (τ) of the Gaussian used to smooth the model curve ($r(t)$ in Eq. 3), (iii) the FWHM ($2\sqrt{2ln(2)}\tau_2$) of the Gaussian that defines the time scale of the variations in the curve (used to determine the weight W_i in Eq. 3), and (iv) the Lagrange parameter (λ in Eq. 3). All these parameters interact in the total smoothing of the curve modeled during the simulation. In the case of too much smoothing the model curve will not have large enough variations to fit the data, whereas in the case of too little smoothing the model curve is too "noisy". We therefore choose the smoothest solution which allows the minimization to converge. The results are shown in Table 1.

We performed Monte Carlo simulations to estimate the errors in the results. Sets of 1000 light curves were simulated with error bars determined randomly from a Gaussian distribution with a σ equal to the measurement errors (σ_a and σ_b). One set was made with the same sampling as the original curves (the simulated examples) and another set of 1000 curves was created with the same number of sampling points as the original, but randomly distributed.

When applying the iterative algorithm it is natural to think that the choice of the number of individual parts n is important for the results. Various tests on our simulated curves indicate that if n is too small, there is little difference from the total curve and higher order microlensing effects can not be properly corrected for. If on the other hand n is too high, each part will contain very few data points and for some parts (depending on the sampling) the overlap between the two curves will be too small to determine the external variations. The choice of n will thus depend on the number of data points and on how they are distributed (e.g., presence of gaps in the curves). The optimal values for the curves in the simulated curves, i.e., the values resulting in the best convergence of Δt, were found to be 3 and 2 in sets 1 and 2 respectively. The results shown in Table 1 correspond to the mean and standard deviation of the values obtained.

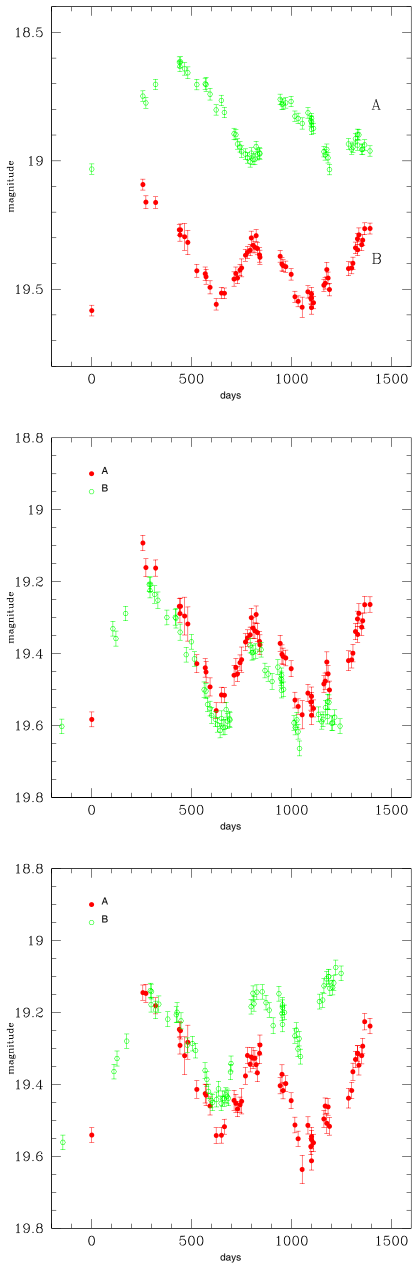

Fig. 1. *Top*: The simulated light curves of two quasar components in set 1a (see text and Table 1). *Middle*: The time delay and magnitude shifted curves in set 1b. The remaining difference between the two curves corresponds to the linear microlensing variation. *Bottom*: The light curves in set 1c, shifted in time delay and magnitude. The remaining difference between the two curves is the higher order microlensing variation.

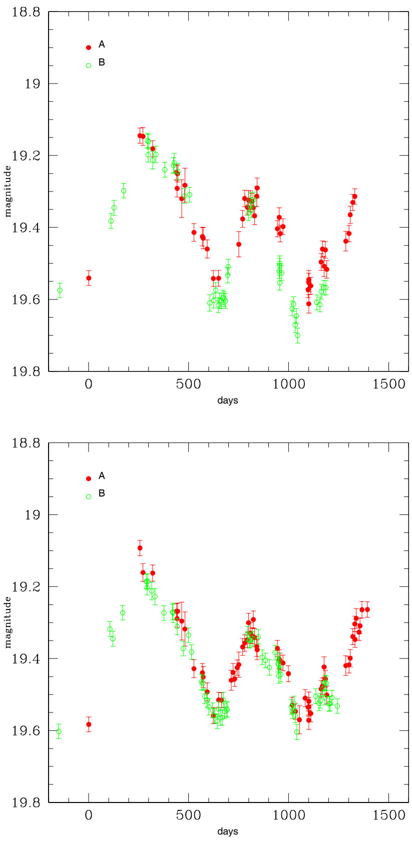

Fig. 2. *Top*: The time delay and magnitude shifted light curves form set 1a. *Bottom*: The microlensing-corrected light curves derived by the iterative run on the curves in set 1c.

3.3. Results

All the time delay measurements obtained in sets 1a, b and 2a, b are very well determined within the estimated errors (see Table 1). As expected, the results depend on the sampling of the light curves and the error estimates from the Monte Carlo simulations with random sampling are larger than the ones obtained with a fixed sampling. In sets 1b and 2b where a slow linear variation is added in one of the curves, the time delay is still well determined whereas in sets 1c and 2c where higher order variations are added there are small systematic errors in the time delay estimated with the direct method. In these cases, the iterative method gives more accurate results with smaller uncertainties. Fig. 2 displays how the microlensing effects in data set 1c are corrected for with the iterative method. In the sets with no microlensing (1a and 2a) we note that the iterative method yields larger errors than the direct method. When no external variations (simulated microlensing effects) are present the best constrained time

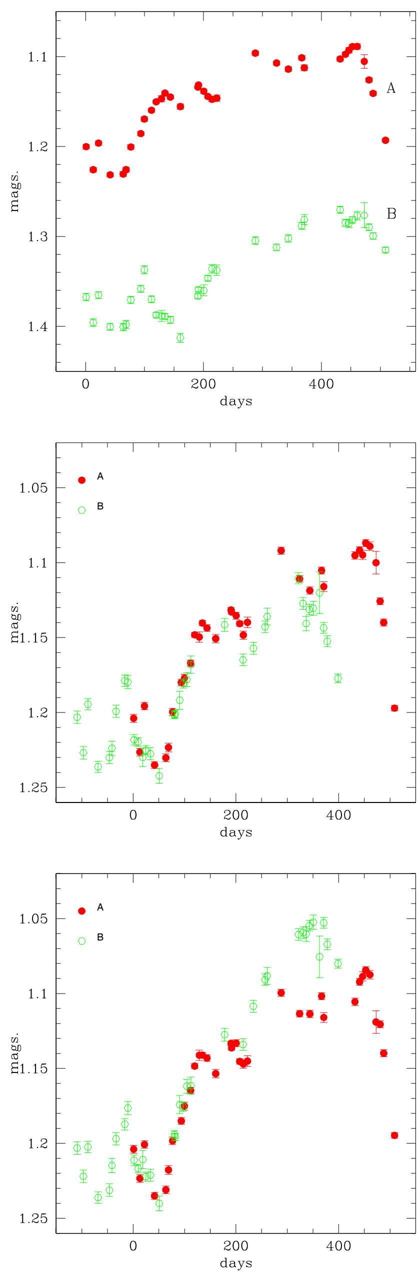

Fig. 3. *Top*: The simulated light curves of two quasar components in set 2a (see text and Table 1). *Middle*: The time delay and magnitude shifted curves in set 2b. The remaining difference between the two curves corresponds to the linear microlensing variation. *Bottom*: The light curves in set 2c, shifted in time delay and magnitude. The remaining difference between the two curves is the higher order microlensing variation.

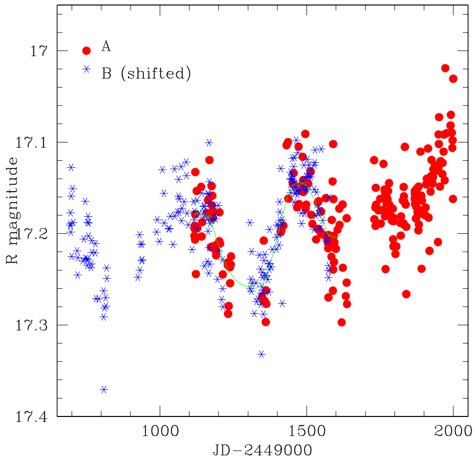

Fig. 4. The R-band light curves of QSO 0957+561. The curve is shifted by 423 days and 0.0625 mag. The solid line shows the model curve derived by the χ^2 algorithm.

delay value is obtained by setting $\alpha = 0$, hence removing one of the free parameters. The iterative method should therefore preferably only be applied where external variations are clearly present.

The magnitude shifts between the two curves are very well determined in sets 2a, b and c whereas in example 1a, b and c there are small systematic errors of $0.01 - 0.05$ mag.

4. Application to light curves of QSO 0957+561

Our method was also applied to a public data set of QSO 0957+561 published by Serra-Ricart et al. (1999) (see Fig. 4). The R-band lightcurves contain 214 data points and span the time interval from February 1996 to July 1998. We removed eight points that deviate by more than 0.05 mag from neighbouring points in both components. We applied our χ^2 algorithm to the data and, as was done for the simulated data, we estimated the error bars using Monte Carlo simulations. A time delay estimate $\Delta t = 423 \pm 9$ days and a magnitude shift $\Delta m = 0.063 \pm 0.007$ were obtained. Considering the two gaps in the data set, JD 2450242 to 2450347 and JD 2450637 to 2450729, Serra-Ricart et al. have divided the data set into two parts, DS I and DS II. Since the second part (DS II) show the largest activity they have determined a time delay value on DS II only, corresponding to the autumn 1997/spring 1998 season. They measure a time delay value of 425±4 days and a magnitude shift of 0.06 mag on these curves. Measurements with two other methods, the dispersion spectra and discrete cross-correlation techniques give values of 426 ± 12 and 428 ± 8 days respectively on the same data set (Serra-Ricart et al. 1999). In order to compare the results we therefore also apply our method to DS II. On the curves in DS II we measure $\Delta t = 424 \pm 22$. Both time delay values, the one measured on the entire data set and the one measured on DS II, are compatible with the results from Serra-Ricart et al. However our errors are larger than the ones found by Serra-Ricart et al. In particular we note that our errors are considerably larger when using only DS II than when using the entire data set. Serra-Ricart et al. do not give any time delay measurement from the total curve but their method seems to be well suited for time delay measurements on a continuous curve (DS II), even when the time span of observation is only of the order of the time delay value. With our method the time delay is better constrained with longer time series, even if gaps are present in the curves.

An additional reason for the differences in the results might be that whereas we have discarded 8 points form the total light curve, Serra-Ricart et al. have discarded 23 points. Given our limited knowledge of the data points we found no reason to exclude more points.

5. Conclusion

We have developed a method to determine time delays between light rays from lensed quasar images from their respective light curves. As other χ^2 based methods (e.g., Press et al. (1992) and Barkanna (1997)) we assume that the statistics of the measurement errors are Gaussian, and we require smoothness for nearby points in the light curves. In our method we have included an additional weight to each of the data points, depending on the relative distance to neighbouring points. In this way one point isolated in time will receive more weight than each individual point in a cluster of nearby points.

Since microlensing effects are often encountered in real light curves of lensed quasars we have adapted our method in order to correct for such variations. A linear term in one of the curves is included to correct for slow long-term variations. Realistic simulations show that the time delay and the magnitude shift between two light curves are determined to within a few percent for cases with no or slow microlensing effects. For faster microlensing variations we find that running the algorithm in an iterative way yields better time delays. This confirms what was proposed in the time delay measurement of B1600+434 (Burud et al. 2000) when the iterative method was first introduced.

An application to a real data set of QSO 0957+561 gives results in agreement with the already published time delay for this data set.

Acknowledgements. IB and SS are supported by contract Pôle d'Attraction Interuniversitaire, P4/05 (SSTC, Belgium). JH is supported by the Danish Natural Science Research Council (SNF).

References

Barkanna, R., 1997, ApJ, 489, 21

Table 1. Results from the analysis of the simulated light curves. The sets (a, b and c) correspond to simulations with respectively no, linear and higher order external variations in one of the components. These variations simulate microlensing effects (see the text for more details).

light curves	1a	1b	1c	2a	2b	2c
true Δt	145	145	145	110	110	110
derived Δt:						
direct method	143±5	151±5	132±5	109±5	119±7	119±4
M.C. fixed sampling	146±5	148±5	135±5	109±5	114±7	115±4
M.C. random sampling	155±23	149±16	147±18	118±40	117±32	118±24
Iterative method	145±7	145±2	143±9	108±7	111±3	114±8
true Δm	1.950	1.950	1.950	0.670	0.670	0.670
derived Δm:						
direct method	1.923±0.002	1.968±0.004	1.868±0.004	0.667±0.001	0.667±0.003	0.647±0.004
M.C. fixed sampling	1.927±0.002	1.964±0.004	1.885±0.004	0.667±0.001	0.665±0.003	0.678±0.004
M.C. random sampling	1.921±0.005	1.963±0.036	1.905±0.08	0.672±0.017	0.65±0.04	0.65±0.02
Iterative method	1.90−2.0	1.91−2.01	1.95−2.31	0.64−0.67	0.65−0.69	0.65−0.69

Burud I., Hjorth J., Jaunsen A. O., et al., 2000 ApJ 544, 117
Hjorth, J., Burud, I., Jaunsen, A. O. et al., 2001, in Gravitational Lensing: Recent progress and future goals, ASP Conf. Ser., eds. T. Brainerd and C. Kochanek, in press
Kayser, R., Refsdal, S., Stabell, R. 1986, A&A, 93, 297
Paczyński, B., 1986, ApJ, 301, 503
Press, W. H., Rybicki, G. B. & Hewitt, J. N. 1992, ApJ, 385, 404
Refsdal S. 1964, MNRAS, 128, 307
Serra-Ricart, M., Oscoz, A., Sanchís, et al., 1999, ApJ, 526, 40

Chapter 3

High resolution imaging of selected systems

With the aim of studying the mass to light distribution of lensing galaxies I have conducted a detailed study of lensed systems at the Nordic Optical Telescope (NOT) (see Burud et al. 1998b). With the MCS image deconvolution technique, high resolution images were extracted from these ground based observations. I present a short summary of the results obtained for three of these targets: MG 0414+05 (Fig. 3.1), SBS1520+530 (Fig. 3.2) and RX J0911+0550 (Section 3.1).

The well-confirmed gravitational lens MG 0414+05 was observed at the NOT in December 1997. No flux variations have been detected in this system so far, which makes it a poor candidate for deriving H_0. However, the quasar is highly reddened and the lensed system (visible almost only in I and longer wavelengths) can be used to study the extinction law in the lensing galaxy and in the quasar host galaxy. The latter is seen as a lensed arc, first detected by HST (Falco et al. 1997), and fully recovered on our deconvolved NOT images. It offers a unique opportunity to study a QSO host galaxy at z=2.6, (see Angonin-Willaime et al. 1998)

The double BAL QSO SBS 1520+530 was observed in I band at the NOT in April 1998. The very faint lens galaxy in this system was detected in the H band by Crampton et al. (1998) with an adaptive optics system. MCS deconvolution gave similar resolution on deep optical images from the NOT and the lens galaxy is clearly resolved. This image provides photometry of the lensing galaxy at near optical wavelength, out of reach of current adaptive optics systems. This object is also variable and a time delay has been measured (see Chapter 8).

RX J0911+0550 was first discovered as a gravitational lens candidate by Bade et al. (1997). By deconvolving high resolution optical images from the NOT and near infra-red images from the New Technology Telescope (NTT) we found the object to be quadruply lensed and revealed the lensing galaxy. Moreover, we found a candidate cluster of galaxies that should be included in the gravitational potential and could explain the non-symmetric configuration of the quasar images. The presence of the cluster of galaxies has later been confirmed by Kneib et al. (2000). With regular monitoring of the target we have recently been able to measure its time delay and to derive a value of H_0 (see Chapter 7).

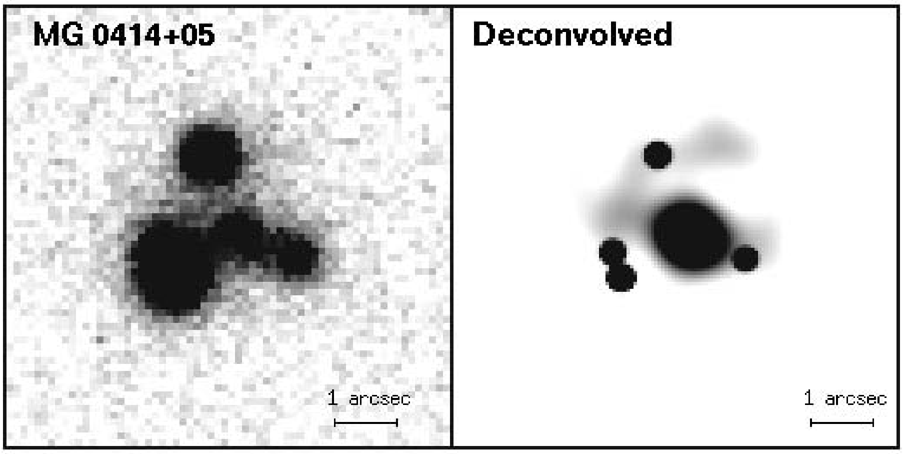

Figure 3.1: [*Left*:] Stack of eight 600s exposures in the I band from the NOT with a seeing of $\sim 0.55''$. North is up and East to the left. [*Right*:] Simultaneous deconvolution of the eight individual frames. The resolution is now $0.16''$. Note the faint lensed arc joining the double SE component and the upper NE component.

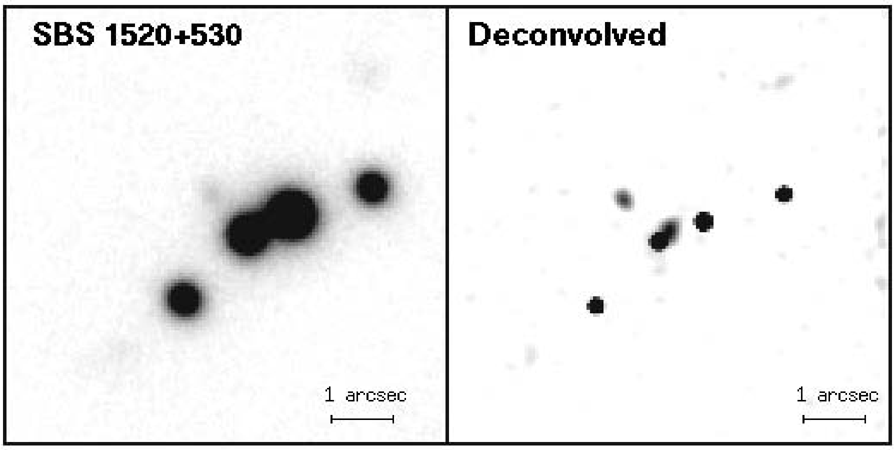

Figure 3.2: [*Left*:] Stack of 16 I band images (total exposure time of 4800s) of the double quasar SBS 1520+530 obtained at the NOT with a seeing seeing of $\sim 0.8''$. The figure displays the double QSO with stars SE and NW of the object. North is up and East to the left. [*Right*:] Simultaneous deconvolution of the 16 individual frames, with a resolution of $0.16''$. The very faint galaxy responsible for the lensing effect is clearly visible.

3.1 Article presenting high resolution imaging of RX J0911+0550

High resolution optical and near-IR imaging of the quadruple quasar RX J0911.4+0551

I. Burud, F. Courbin, C. Lidman, A.O. Jaunsen, J. Hjorth, R. Østensen, M.I. Andersen, J.W. Clasen, O. Wucknitz, G. Meylan, P. Magain, R. Stabell, S. Refsdal

Astrophysical Journal, 1998, 507, L5

High resolution optical and near-IR imaging of the quadruple quasar RX J0911.4+0551[1]

I. Burud

Institut d'Astrophysique et de Géophysique, Université de Liège, Avenue de Cointe 5, B–4000 Liège, Belgium

F. Courbin

Institut d'Astrophysique et de Géophysique, Université de Liège, Avenue de Cointe 5, B–4000 Liège, Belgium
URA 173 CNRS-DAEC, Observatoire de Paris, F–92195 Meudon Principal Cédex, France

C. Lidman

ESO, Casilla 19001, Santiago 19, Chile

A.O. Jaunsen

Institute of Theoretical Astrophysics, University of Oslo, Pb. 1029 Blindern, N-0315 Oslo, Norway
Centre for Advanced Study, Drammensvn. 78, N-0271 Oslo, Norway

J. Hjorth

NORDITA, Blegdamsvej 17, DK-2100 Copenhagen Ø, Denmark
Centre for Advanced Study, Drammensvn. 78, N-0271 Oslo, Norway

R. Østensen

Institut d'Astrophysique et de Géophysique, Université de Liège, Avenue de Cointe 5, B–4000 Liège, Belgium
Department of Physics, University of Tromsø, N-9037 Tromsø, Norway

M.I. Andersen, J.W. Clasen

Nordic Optical Telescope, Apartado 474, E-38700 St. Cruz de La Palma, Canary Islands, Spain

O. Wucknitz

Hamburger Sternwarte, Gojenbergsweg 112, D-21029 Hamburg, Germany

[1]Based on observations obtained at NOT and ESO La Silla

G. Meylan
ESO, Karl-Schwarzschild-Strasse 2, D-85748, Garching bei München, Germany

P. Magain[2]
Institut d'Astrophysique et de Géophysique, Université de Liège,
Avenue de Cointe 5, B–4000 Liège, Belgium

R. Stabell
Institute of Theoretical Astrophysics, University of Oslo, Pb. 1029 Blindern, 0315 Oslo, Norway
Centre for Advanced Study, Drammensvn. 78, N-0271 Oslo, Norway,

S. Refsdal
Hamburger Sternwarte, Gojenbergsweg 112, D-21029 Hamburg, Germany
Institute of Theoretical Astrophysics, University of Oslo, Pb. 1029 Blindern, N-0315 Oslo, Norway
Centre for Advanced Study, Drammensvn. 78, N-0271 Oslo, Norway

ABSTRACT

We report the detection of four images in the recently discovered lensed QSO RX J0911.4+0551. With a maximum angular separation of 3.1″, it is the quadruply imaged QSO with the widest known angular separation. Raw and deconvolved data reveal an elongated lens galaxy. The observed reddening in at least two of the four QSO images suggests differential extinction by this lensing galaxy. We show that both an ellipticity of the galaxy ($\epsilon_{\rm min} = 0.075$) and an external shear ($\gamma_{\rm min} = 0.15$) from a nearby mass has to be included in the lensing potential in order to reproduce the complex geometry observed in RX J0911.4+0551. A possible galaxy cluster is detected about 38″ from RX J0911.4+0551 and could contribute to the X-ray emission observed by ROSAT in this field. The color of these galaxies indicates a plausible redshift in the range of 0.6-0.8.

Subject headings: galaxies: clusters: general — gravitational lensing — quasars: individual (RX J0911.4+0551)

[2] Maître de Recherches au Fonds National Belge de la Recherche Scientifique

1. Introduction

RX J0911.4+0551, an AGN candidate selected from the ROSAT All-Sky Survey (RASS) (Bade et al. 1995, Hagen et al. 1995), has recently been classified by Bade et al. (1997; hereafter B97) as a new multiply imaged QSO. B97 show that it consists of at least three objects: two barely resolved components and a third fainter one located 3.1″ away from the other two. They also show that the spectrum of this third fainter component is similar to the combined spectrum of the two bright components. The lensed source is a radio quiet QSO at $z = 2.8$. Since RASS detections of distant radio quiet QSOs are rare, B97 pointed out that the observed X-ray flux might originate from a galaxy cluster at $z \geq 0.5$ within the ROSAT error box. We present here new optical and near-IR high-resolution images of RX J0911.4+0551 obtained with the 2.56m Nordic Optical Telescope (NOT) and the ESO 3.5m New Technology Telescope (NTT). Careful deconvolution of the data allows us to clearly resolve the object into four QSO components and a lensing galaxy. In addition, a candidate galaxy cluster is detected in the vicinity of the four QSO images. We estimate its redshift from the photometric analysis of its member galaxies.

2. Observations and reductions

We first observed RX J0911.4+0551 in the K-band with IRAC 2b on the ESO/MPI 2.2m telescope on November 12, 1997. In spite of the poor seeing conditions ($\sim 1.3''$), preliminary deconvolution of the data made it possible to suspect the quadruple nature of this object. Much better optical observations were obtained at the NOT (La Palma, Canary Islands, Spain). Three 300s exposures through the I filter, with a seeing of $\sim 0\farcs8$ were obtained with ALFOSC under photometric conditions on November 16, 1997. Under non-photometric, but excellent seeing conditions ($\sim 0\farcs5 - 0\farcs8$), three 300s I-band exposures, three 300s V-band and five 600s U-band exposures were taken with HIRAC on the night of December 3, 1997. The pixel scales for HIRAC and ALFOSC are $0\farcs1071$ and $0\farcs186$, respectively. RX J0911.4+0551 was also the first gravitational lens to be observed with the new wide field near-IR instrument SOFI, mounted on the ESO 3.5m NTT. Excellent K and J images were taken on December 15, 1997, and January 19, 1998 respectively. The 1024 $\times$ 1024 Rockwell detector was used with a pixel scale of $0\farcs144$.

The optical data were bias subtracted and flat-field corrected using sky-flats. Fringe-correction was also applied to the I-band data from ALFOSC. Sky subtraction was carried out by fitting low-order polynomial surfaces to selected areas of the frames. Cosmic ray removal was finally performed on the data. The infrared data were processed as explained in Courbin, Lidman & Magain (1998), but in a much more efficient way for SOFI than for IRAC 2b data, since the array used with the former instrument is cosmetically superior to the array used with the latter.

3. Deconvolution of RX J0911.4+0551

All images were deconvolved using the new deconvolution algorithm by Magain, Courbin & Sohy (1998; hereafter MCS). The sampling of the images was improved in the deconvolution process, i.e. the adopted pixel size in the deconvolved image is half the pixel size of the original frames. The final resolution adopted in each band was chosen according to the signal-to-noise (S/N) ratio of the data, the final resolution improving with the S/N.

Our NOT HIRAC data were deconvolved down to the best resolution achievable with the adopted sampling (2 pixels FWHM, i.e. $0\farcs1$), whereas the NOT/ALFOSC frames were deconvolved to a resolution of 3 pixels FWHM, i.e. $0\farcs29$. Although of very good quality, the near IR-data have a lower S/N than the optical data. The resolution was therefore limited to 5 pixels FWHM in both J and K ($0\farcs36$) in order to avoid noise enhancement.

The MCS algorithm can be used to deconvolve simultaneously a stack of individual images or to deconvolve a single stacked image. The results from the simultaneous deconvolutions are displayed in Fig. 1. The four QSO images are labeled A1, A2, A3, and B. The quality of the results was checked from the residual maps, as explained in Courbin et al. (1998). The deconvolution procedure decomposes the images into a number of Gaussian point sources, for which the program returns the positions and intensities, plus a deconvolved numerical background. In the present case, the deconvolution was also performed with an analytical De Vaucouleurs, and exponential disk galaxy profile at the position of the lensing galaxy, in order to better describe its morphology.

3.1. Results

Table 1 lists the flux of each QSO component, relative to A1, as derived from the simultaneous deconvolutions. Although the HIRAC U, V and I band data were taken during non photometric conditions, they can still be used to determine the relative fluxes between the four images of the QSO. The errors in the relative fluxes are determined from the simultaneous deconvolutions and represent the 1-σ standard deviation in the peak intensities.

When flux calibration was possible, magnitudes were calculated and the results are displayed in Table 2, which also contains the positions of the four QSO components relative to A1. The astrometric errors are derived by comparing the positions of the components in the different bands.

The deconvolved numerical background is used to determine the galaxy position from the first order moment of the light distribution. A reasonable estimate of the error on the lens position was derived from moment measurements through apertures of varying size and on several images obtained by running deconvolutions with different initial conditions. I, J, and K magnitudes for the galaxy were also estimated from the deconvolved background image by aperture photometry ($\sim 1.2''$ aperture in diameter). The numerical galaxy is elongated in all three bands and the position angle of its major axis is $\theta_G \simeq 140 \pm 5°$. In the near-IR, the galaxy looks like it is composed of a bright sharp nucleus plus a diffuse elongated disk. However we can not exclude that the observed elongation is due to an unresolved blend of two or more intervening objects. None of our two analytical profiles fit perfectly the galaxy. The De Vaucouleurs profile (e $= 1 -$ b/a $= 0.31 \pm 0.07$, $\theta_G = 130 \pm 10°$) fits slightly better than the exponential disk light distribution, but still produces residual maps with values as large as 1.5-2 per pixel, compared with a χ^2 of 2.5-5 per pixel for the exponential disk profile. The ellipticity and the position angle derived this way are very uncertain due to the low S/N of the data. Much deeper observations will be required to perform precise surface photometry of the lens(es) and to draw a definite conclusion about its (their) morphology.

3.2. Field photometry

In order to detect any intervening galaxy cluster which might be involved in the overall lensing potential and contributing to the X-ray emission observed by ROSAT, we performed I, J, and K band photometry on all the galaxies in a $2.5'$ field around the lensed QSO. A composite color image was also constructed from the frames taken through these 3 filters, in order to directly visualize any group of galaxies with similar colors, and therefore likely to be at the same redshift. The color composite is presented in Fig. 2.

Aperture photometry was carried out using the SExtractor package (LINUX version 1.2b5, Bertin & Arnouts, 1996). The faintest objects were selected to have at least 5 adjacent pixels above $1.2\sigma_{sky}$, leading to the limiting magnitudes 23.8, 21.6, and 20.0 mag/arcsec^2 in the I, J, and

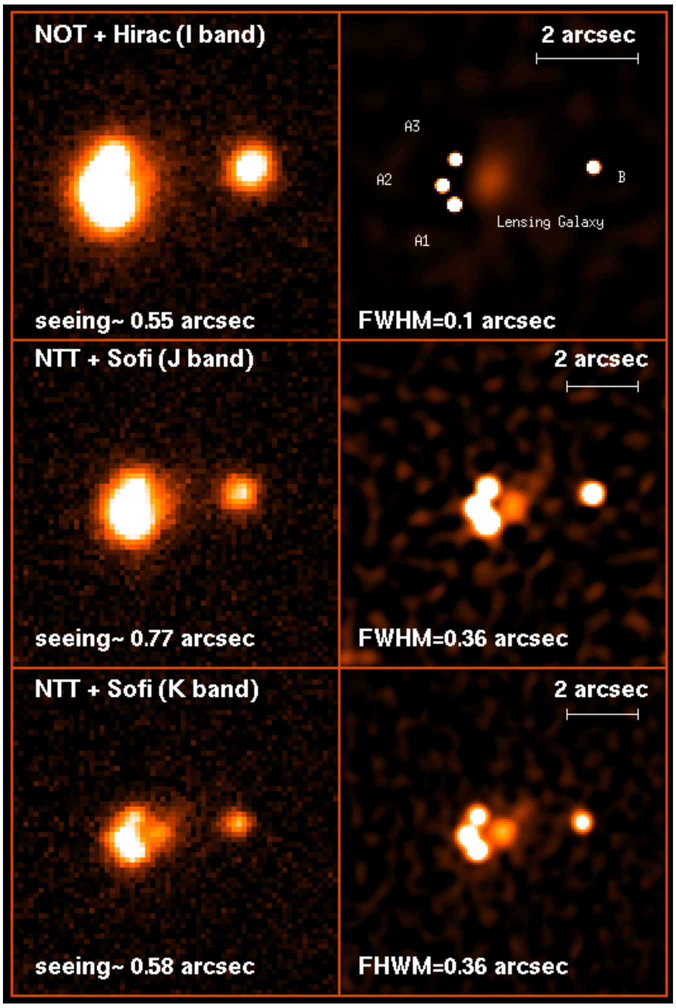

Fig. 1.— High resolution images of RX J0911.4+0551 are displayed in the left panels with, in the right panels, their corresponding deconvolved versions with improved resolution and sampling. In each band, the individual data frames are deconvolved simultaneously. [Top:] Stack of 3 NOT+HIRAC I-band image. The total exposure time is 900s. [Middle:] Stack of 9 NTT+SOFI J-band frames. The total exposure time is 1080s. [Bottom:] Stack of 19 NTT+SOFI K-band with a total exposure time of 2400s. For all the three bands the object is clearly resolved into four QSO images, labeled A1, A2, A3, and B, plus the elongated lensing galaxy. The field of the optical and near IR data are respectively $7''$ and $9''$ on a side. North is to the top and East to the left in all frames.

K bands, respectively. The faintest extended object measured in the different bands had magnitudes 23.0, 22.0, and 20.3 in I, J, and K, respectively. The color-magnitude diagram of the field was constructed from the I and K band data which give the widest wavelength range possible with our photometric data. Since the seeing was different in the two bands, particular attention was paid to the choice of the isophotal apertures fitted to the galaxies. They were chosen to be as large as possible, still avoiding too much contamination from the sky noise, as an oversized isophotal aperture would introduce. The color-magnitude diagram of the galaxies in the 2.5′ field is displayed in Fig. 3 . Stars are not included in this plot. Note that, because of their proximity, the magnitudes of the two blended members of the cluster candidate (center of the circle in Fig. 2) might be underestimated by as much as 0.3-0.4 magnitudes in both I and K.

4. Models

In a first attempt to model the system we chose an elliptical potential of the form

$$\psi = \psi(r_{\mathrm{e}}), \tag{1}$$

$$r_{\mathrm{e}}^2 = \frac{x'^2}{(1+\epsilon)^2} + \frac{y'^2}{(1-\epsilon)^2}, \tag{2}$$

where the coordinates x' and y' are measured along the principal axes of the galaxy, whose position angle θ_{G} is a free parameter. For small ellipticities ϵ, this potential is a good approximation for elliptical mass distributions (Kassiola & Kovner 1993). Additionally, an external shear γ with direction ϕ is included. Even without assuming an explicit potential ψ, we can determine the minimal γ and ϵ needed to reproduce the observed image positions, by applying the methods given by Witt & Mao (1997). Their methods eliminate the unknown parameters of the model to find constraints for the ellipticity of the galaxy and the external shear. For the shear we predict a minimum of $\gamma_{\min} = 0.15 \pm 0.07$, while $\epsilon_{\min} = 0.075 \pm 0.034$ (both with 1σ errors). Therefore, neither ellipticity nor shear should be omitted from the modeling. To keep models simple, we used a pseudo-isothermal potential corresponding to an apparent deflection angle of

$$\boldsymbol{\alpha} = \frac{\alpha_0}{r_{\mathrm{c}} + \sqrt{r_{\mathrm{c}}^2 + r_{\mathrm{e}}^2}} \left(\frac{x}{(1+\epsilon)^2}, \frac{y}{(1-\epsilon)^2} \right), \tag{3}$$

which degenerates to a singular isothermal sphere for vanishing core-radius r_{c} and ellipticity ϵ.

The model's parameters are determined by minimizing the χ^2 given by the observed and predicted positions of the images and the galaxy. The best model leads to $\chi^2 = 0.65$ and has parameters as given in Table 3. This value is reasonable for a model with one degree of freedom (r_{c} can not be counted as a free parameter here, because without the restriction of $r_{\mathrm{c}} \geq 0$ it would become negative in the fit). The positions of the images and the galaxy in Table 3 are parameters of the model and have to be compared with the observed positions in Table 2.

As shown above, no elliptical potential without a shear, and no spherical potential with shear can reproduce the observational data. For our pseudo-isothermal model, this results in large χ^2 values of 50.5 and 63.7, respectively. These values are much too high for the two degrees of freedom.

5. Discussion

Thanks to our new high-resolution imaging data, the QSO RX J0911.4+0551 is resolved into four images. In addition, deconvolution with the new MCS algorithm reveals the lensing galaxy, clearly confirming the lensed nature of this system. The image deconvolution provides precise photometry and astrometry for all the components of the system.

Reddening in components A2 and A3 relative to A1 is observed from our U, V, and I frames that were taken within three hours on the same night. The absence of reddening in component

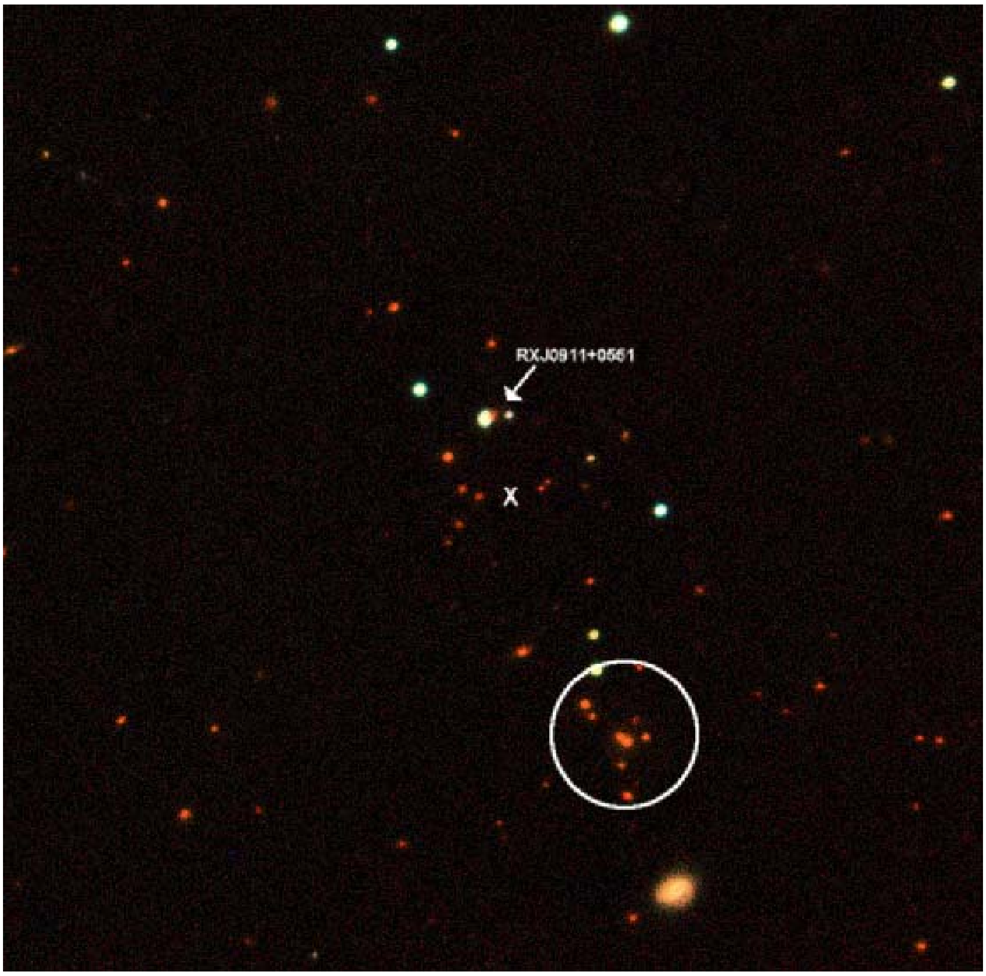

Fig. 2.— Composite image of a 2′ field around RX J0911.4+0551. The frame has been obtained by combining our I, J and K-band data. North is up and East to the left. Note the group of red galaxies with similar colors, about 38″ SW of the quadruple lens (circle) and the group of even redder galaxies 10″ SW of the lens (cross).

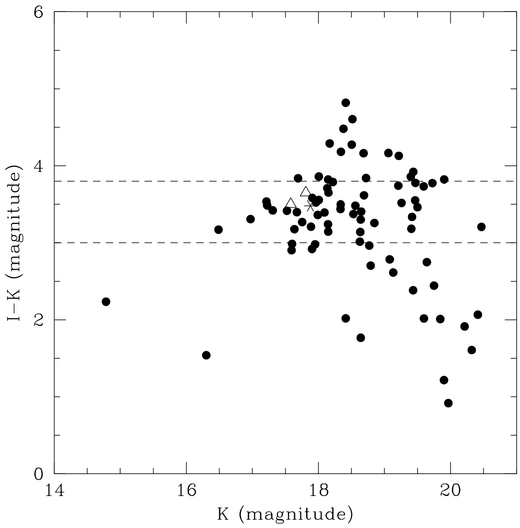

Fig. 3.— Color magnitude diagram of the 2.5′ field around RX J0911.4+0551. The lensing galaxy and many of the cluster members form the overdensity around $I - K \sim 3.3$. The lensing galaxy in RX J0911.4+0551 is marked by a star and the two blended galaxies in the center of the cluster candidate are plotted as triangles. Stars are not plotted in this diagram.

B and the difference in reddening between components A2 and A3 suggest extinction by the deflecting galaxy. Note that although our near-IR data were obtained from 15 days to 6 weeks after the optical images, they appear to be consistent with the optical fluxes measured for the QSO images, i.e. flux ratios increase continuously with wavelength, from U to K, indicating extinction by the lensing galaxy.

We have discovered a good galaxy cluster candidate in the SW vicinity of RX J0911.4+0551 from our field photometry in the I, J, and K bands. Comparison of our color-magnitude diagram with that of a blank field (e.g., Moustakas et al. 1997) shows that the galaxies around RX J0911.4+0551 are redder than field-galaxies at an equivalent apparent magnitude. In addition, the brightest galaxies in Fig. 3 lie on a red sequence at $I - K \sim 3.3$, typical for the early type members of a distant galaxy cluster. The two dashed lines indicate our ± 0.4 color error bars at $K \sim 19$ around $I - K \sim 3.3$. Most of these galaxies are grouped in the region around a double elliptical at a distance of $\sim 38''$ and a position angle of $\sim 204°$ relative to A1. This can also be seen in Fig. 2 which shows a group of red galaxies with similar colors centered on the double elliptical (in the center of the circle).

Consequently, there is considerable evidence for at least one galaxy cluster in the field. The redshift of our best candidate cluster (the one circled in Fig. 2) can be estimated from the I and K band photometry. We have compared the K-band magnitudes of the brightest cluster galaxies with the empirical K magnitude vs. redshift relation found by Aragón-Salamanca et al. (1998). We find that our cluster candidate, with its brightest K magnitude of about ~ 17.0, should have a redshift of $z \sim 0.7$. A similar comparison has been done in the I-band without taking into account galaxy morphology. We compare the mean I magnitude of the cluster members with the ones found by Koo et al. (1996) for galaxies with known redshifts in the Hubble

Deep Field and obtain a cluster redshift between 0.6 and 0.9. Finally, comparison of the $I - K$ color of the galaxy sequence with data and models from Kodama et al. (1998) confirm the redshift estimate of 0.6-0.8.

In order to calculate physical quantities from the model parameters found in section 4, we assume a simple model for the cluster which may be responsible for the external shear. For an isothermal potential, the true shear and convergence are of the same order of magnitude. As the convergence is not explicitly included in the model, the deduced shear is a reduced shear leading to an absolute convergence of $\kappa = \gamma/(1+\gamma) = 0.241$. For a cluster redshift of $z_{\rm d} = 0.7$ and with cosmological parameters $\Omega = 1$, $\lambda = 0$ this corresponds to a velocity dispersion of about $1100\,{\rm km\,s^{-1}}$ if the cluster is positioned at an angular distance of $40''$. See Gorenstein, Falco & Shapiro (1988) for a discussion of the degeneracy preventing a direct determination of κ. From the direction of the shear ϕ, (see Table 3) we can predict the position angle of the cluster as seen from the QSO to be 12° or 192°. The latter value agrees well with the position of our cluster candidate SW of the QSO images. Note also the good agreement between the position angle $\theta_{\rm G}$ derived from the observed light distribution, and the predicted position angle corresponding to our best fitting model of the lensing potential. Interestingly, this is in good agreement with Keeton, Kochanek & Falco (1998) who find that projected mass distributions are generally aligned with the projected light distributions to less than 10°.

The color of the main lensing galaxy is very similar to that of the cluster members, suggesting that it might be a member of the cluster. Using the same model for the cluster as above, assuming the galaxy at the same redshift as the cluster, and neglecting the small ellipticity of $\epsilon < 0.05$, the velocity dispersion of the lensing galaxy can be predicted from the calculated deflection angle α_0 to be of the order of $240\,{\rm km\,s^{-1}}$. Since the galaxy profile is sharp towards the nucleus in K, we cannot rule out the possibility of a fifth central image of the source, as predicted for non-singular lens models. Near-IR spectroscopy is needed to get a redshift determination of the lens and to show whether it is blended or not with a fifth image of the (QSO) source.

Some $10''$ SW from the lens, we detect a small group of even redder objects. These red galaxies can be seen in Fig. 2 a few arcseconds to the left and to the right of the cross. They might be part of a second galaxy-group at a higher redshift, and with a position in better agreement with the X-ray position mentioned by B97. However, since the measured X-ray signal is near the detection limit, and the 1-σ positional uncertainty is at least $20''$, the X-ray emission is compatible with both the QSO and these galaxy groups in the field. Furthermore, this second group, at $z > 0.7$, would most likely be too faint in the X-ray domain to be detected in the RASS. In fact, even our lower redshift cluster candidate would need to have an X-ray luminosity of the order of $L_{0.1-2.4\rm keV} \sim 7.10^{44}{\rm erg\,s^{-1}}$ (assuming a 6 keV thermal spectrum, $H_0 = 50\,{\rm km\,s^{-1}\,Mpc^{-1}}$, $q_0 = 0.5$), in order to be detected with 0.02 ${\rm cts\,s^{-1}}$ by ROSAT. This is very bright but not unrealistic for high redshift galaxy clusters (e.g., MS 1054-03, Donahue, Gioia, Luppino et al. 1997).

RX J0911.4+0551 is a new quadruply imaged QSO with an unusual image configuration. The lens configuration is complex, composed of one main lensing galaxy plus external shear possibly caused by a galaxy cluster at redshift between 0.6 and 0.8 and another possible group at $z > 0.7$. Multi-object spectroscopy is needed in order to confirm our cluster candidate/s and derive its/their redshift and velocity dispersion. In addition, weak lensing analysis of background galaxies might prove useful to map the overall lensing potential involved in this complex system.

The authors would like to thank A. Moorwood and J.G. Cuby for making available to us the NTT/SOFI data and the referee E.E. Falco for useful comments. We also thank S. Sohy for her help with the preliminary data analysis, T. Kodama for providing his model results for our photometric system, T.J. Broadhurst, C.R. Keeton, G. Rauw for helpful discussions and R. Sip for help in improving the figures. IB, FC and RØ are supported in part by contract ARC94/99-178 "Action de Recherche Concertée de la Communauté Française (Belgium)" and Pôle d'Attraction Interuniversitaire, P4/05 (SSTC, Belgium).

REFERENCES

Aragón-Salamanca, A., Baugh, C.M., Kauffmann, G., 1998, preprint astro-ph/9801277

Bade, N., Fink, H.H., Engels, D., et al., 1995, A&AS, 110, 469

Bade, N., Siebert, J., Lopez, S., et al., 1997, A&A, 317, L13

Bertin, E., Arnouts, S., 1996, A&AS, 117, 393

Courbin, F., Lidman, C., Magain, P., 1998, A&A, 330, 57

Donahue, M., Gioia, I., Luppino, G., et al. 1997, preprint astro-ph/9707010

Gorenstein, M.V., Falco, E.E., Saphiro, I.I., 1988, ApJ, 327, 693

Hagen, H.-J., Groote, D., Engels, D., Reimers, D., 1995, A&AS, 111, 195

Kassiola, A., Kovner, I., 1993, ApJ, 417, 450

Keeton, C.R., Kochanek, C.S., Falco, E.E., 1998, preprint astro-ph/ 9708161

Kodama, T., Arimoto, N., Barger, A.J., et al., 1998, preprint astro-ph/9802245

Koo, D.C., Vogt, N.P., Phillips, A.C., et al., 1996, ApJ, 469, 535

Magain, P., Courbin, F., Sohy, S., 1998, ApJ, 494, 452

Moustakas, L.A., Davis, M., Graham, J.R., et al., 1997, ApJ, 475, 445

Witt, H.J., Mao, S., 1997, MNRAS, 291, 211

This 2-column preprint was prepared with the AAS LaTeX macros v4.0.

Table 1: Flux ratios for all four QSO components, relative to A1

	A2	A3	B
F_K	0.965 ± 0.013	0.544 ± 0.025	0.458 ± 0.004
F_J	0.885 ± 0.003	0.496 ± 0.005	0.412 ± 0.005
F_I	0.680 ± 0.013	0.398 ± 0.002	0.420 ± 0.003
F_V	0.587 ± 0.009	0.334 ± 0.004	0.413 ± 0.006
F_U	0.590 ± 0.013	0.285 ± 0.007	0.393 ± 0.004

NOTE.—Results obtained from our non-photometric data. All measurements are given along with their 1-σ errors.

Table 2: Photometric and astrometric properties of RX J0911.4+0551 and the lensing galaxy.

	A1	A2	A3	B	G
K	17.137 ± 0.020	17.308 ± 0.035	17.933 ± 0.074	18.119 ± 0.010	17.88 ± 0.12
J	17.794 ± 0.030	17.927 ± 0.029	18.556 ± 0.038	18.757 ± 0.020	19.85 ± 0.12
I	18.310 ± 0.084	18.728 ± 0.096	19.305 ± 0.133	19.197 ± 0.083	21.36 ± 0.13
$x('')$	0.000 ± 0.004	-0.259 ± 0.007	$+0.013 \pm 0.008$	$+2.935 \pm 0.002$	$+0.709 \pm 0.026$
$y('')$	0.000 ± 0.008	$+0.402 \pm 0.006$	$+0.946 \pm 0.008$	$+0.785 \pm 0.003$	$+0.507 \pm 0.046$

NOTE.—The astrometry is given relative to component A1 with x and y coordinates defined positive to the North and West of A1. All measurements are given along with their 1-σ errors. The 1-σ errors on the photometric zero points are 0.02 in all bands.

Table 3: Parameters of the best-fit model.

α_0	r_c	ϵ	θ_G	γ	ϕ	$\boldsymbol{\theta}_0$	$\boldsymbol{\theta}_S$
$1''.1061$	0	0.0476	$140^\circ.5$	0.3176	$102^\circ.3$	$+0''.7078$	$+1''.1459$
						$+0''.5440$	$+0''.5452$

image	x	y	amplification
A_1	$+0''.0000$	$-0''.0004$	-4.45
A_2	$-0''.2590$	$+0''.4019$	$+8.59$
A_3	$+0''.0130$	$+0''.9456$	-3.70
B	$+2''.9350$	$+0''.7850$	$+1.79$

NOTE.—$\boldsymbol{\theta}_0$ and $\boldsymbol{\theta}_S$ are the position of the galaxy and the source, respectively. The core radius r_c was a free parameter constrained to $r_c \geq 0$ in the modeling. The best fit lead to $r_c = 0$. Position angles θ_G and ϕ are measured from N to E. Negative amplification is due to odd parity of the image.

Chapter 4

Optical monitoring

I have been conducting long-term photometric monitoring of a number of lensed quasars, both in the northern and southern hemispheres, with the goal of measuring time delays in as many systems as possible, in order to study the mass distribution in the lensing galaxy(ies) and to determine H_0. The deep images are also used to constrain the light distribution in the lens galaxies. Moreover, complementary data are obtained to study extinction effects and to determine redshifts of sources and lensing galaxies.

In the northern hemisphere a programme was started by J. Hjorth et al. in April 1998 at the NOT (2.56m) situated at La Palma (Canary Islands). The programme is a collaboration between Copenhagen, Liège and Oslo. Observations are currently obtained on a weekly basis. Three detectors are being used: ALFOSC (Andalucía Faint Object Spectrograph), HiRAC (High Resolution Adaptive Camera) and the stand-by camera StanCam, equipped with detectors yielding pixel scales of 0.188 arcsec, 0.107 arcsec and 0.176 arcsec respectively. As about 95% of the observations are obtained with ALFOSC, the data sets are very homogeneous. The seeing ranges from 0.5 arcsec to 2.0 arcsec with 0.9 arcsec as the most frequent value.

In the southern hemisphere we have ongoing monitoring programmes at the 1.5m Danish telescope and at the NTT (New Technology Telescope 3.6m run by Europan Southern Observatory, ESO) both situated at La Silla, Chile. Both programmes are collaborations between Liège, Copenhagen and Santiago (PI: P. Magain). The programme at the 1.5m Danish telescope was started in October 1998 and weekly observations are obtained with the DFOSC (Danish Faint Object Spectrograph Camera) instrument (0.39 arcsec pixel scale). The seeing of the images used to range from 1.0 to 2.5 arcsec with 1.3 arcsec being the most frequent value. Since the arrival of the new chip on the detector in October 2000, the seeing has improved and is now most often 1.0 arcsec. The monitoring at the 1.5m Danish was extended to the NTT in October 1999 in order to monitor faint and/or compact systems that could not be observed with the 1.5m Danish. Two instruments, SUSI (Superb Seeing Imager) and EMMI (ESO Multi Mode Instrument) are used, with pixel scales of 0.08 (0.161 arcsec in the 2x binned mode) and 0.27 arcsec respectively. The seeing in the NTT frames ranges from 0.5 to 1.8 arcsec.

These programmes have been made possible thanks to the great enthusiasm and collaboration efforts of NOT staff, NTT team, the 2.2m team and the observers at the three telescopes. Very little observing time has been lost in spite of the non-conventional scheduling of such a project. I shall in the following chapters present the results obtained for four lensed quasars: B1600+434, RX J091+0550, HE 2149-2745 and SBS1520+530.

Chapter 5

Article presenting the time delay measurement in B1600+434

An optical time delay for the double gravitational lens system B1600+434

I. Burud, J. Hjorth, A.O. Jaunsen, M.I. Andersen, H. Korhonen, J.W. Clasen, J. Pelt, F. P. Pijpers, P. Magain and R. Østensen

Astrophysical Journal, 1998, 544, 117

An optical time-delay estimate for the double gravitational lens system B1600+434 [1]

I. Burud

Institut d'Astrophysique et de Géophysique de Liège, Avenue de Cointe 5, B-4000 Liège, Belgium

J. Hjorth

Astronomical Observatory, University of Copenhagen, Juliane Maries Vej 30, DK–2100 Copenhagen Ø, Denmark

A. O. Jaunsen

Institute of Theoretical Astrophysics, University of Oslo, Pb. 1029 Blindern, N0315 Oslo, Norway

M. I. Andersen, H. Korhonen

Division of Astronomy, University of Oulu, P.O. Box 3000, FIN–90014 Oulun Yliopisto, Finland

J. W. Clasen

Nordic Optical Telescope, Apartado 474, E–38700 St. Cruz de La Palma, Canary Islands, Spain

J. Pelt

Tartu Astrophysical Observatory, Tõravere, 61602, Estonia

F. P. Pijpers

Theoretical Astrophysics Center, University of Aarhus, DK–8000 Århus C, Denmark

P. Magain

Institut d'Astrophysique et de Géophysique de Liège, Avenue de Cointe 5, B-4000 Liège, Belgium

and

R. Østensen

Department of Physics, University of Tromsø, Tromsø, Norway

ABSTRACT

We present optical I-band light curves of the gravitationally lensed double QSO B1600+434 from observations obtained at the Nordic Optical Telescope (NOT) between April 1998 and November 1999. The photometry has been performed by simultaneous deconvolution of all the data frames, involving a numerical lens galaxy model. Four methods have been applied to determine the time delay between the two QSO components, giving a mean estimate of $\Delta t = 51 \pm 4$ days (95% confidence level). This is the fourth optical time delay ever measured. Adopting a $\Omega = 0.3$, $\Lambda = 0$ Universe and using the mass model of Maller et al. (2000), this time-delay estimate yields a Hubble parameter of $H_0 = 52^{+14}_{-8}$ km s^{-1} Mpc^{-1} (95% confidence level) where the errors include time-delay as well as model uncertainties. There are time-dependent offsets between the two (appropriately shifted) light curves that indicate the presence of external variations due to microlensing.

Subject headings: cosmology: observations — gravitational lensing: individual (B1600+434) — distance scale — galaxies: spiral

1. Introduction

Intensive observational studies of gravitationally lensed QSOs have been conducted in the last few years with the aim of determining cosmological parameters, e.g., the Hubble constant, H_0, and to study the dark-matter distribution in lens galaxies. In particular, there has been a significant effort to measure time delays between lensed QSO components to derive H_0 with the method described by Refsdal (1964). Following a more than decade-long monitoring of the double QSO 0957+561 by Schild and coworkers (Schild 1990; Schild & Thomson 1995), Schild & Thomson (1997) and Kundić et al. (1997) succeeded in pinning down its time delay in 1997. The same year saw an even more impressive accomplishment of Schechter et al. (1997) to determine multiple time delays in the 'triple QSO' PG1115+080 from a peak-to-peak variation of barely 0.15 mag. Following this demonstration of the feasibility of measuring time delays of multiply imaged QSOs an ongoing photometric monitoring was initiated at the Nordic Optical Telescope (NOT) in April 1998. The program involves measuring time delays between lensed QSO components in as many systems as possible. Our main target during the first year of monitoring was the doubly imaged radio source QSO B1600+434 (Jackson et al. 1995) at redshift $z = 1.59$ (Fassnacht & Cohen 1998), which is gravitationally lensed by an edge-on late-type galaxy at $z = 0.41$ (Jaunsen & Hjorth 1997; Fassnacht & Cohen 1998). The $1.39''$ angular separation between the two QSO images (labeled A and B in Fig. 1), together with the observed large flux variations in the system (Jaunsen & Hjorth 1997), makes it well suited for time-delay measurements. Given the poor knowledge of the mass distribution in dark-matter halos of spiral galaxies, a time-delay measurement in B1600+434 may not provide a firm determination of H_0. However, once H_0 has been determined from other lensed systems or using other methods, the time delay of B1600+434 can provide new constraints on the distribution of mass in the various components of spiral galaxies in general (Maller et al. 2000).

B1600+434 is very faint, with $I \sim 22$ for the faintest QSO component and $I = 20.3$ for the lensing galaxy. Furthermore, the B-component is substantially obscured by the lens (see Fig. 1) and photometry of the image is non-trivial. The data have therefore been analyzed with advanced deconvolution techniques both in order to model the light distribution of the lensing galaxy and to achieve accurate photometry of the QSO component blended with the lens nucleus. The time delay we present using the deconvolution technique is the fourth one measured at optical wavelengths, and it is the first of our monitoring program. A preliminary report was presented in Hjorth et al. (1999). The results presented here include more data points and supercede this report. Independently, a time delay has been measured at radio wavelengths with the VLA during the same observing season (Koopmans et al. 2000).

2. Observations and Data Reduction

Weekly observations of B1600+434 were carried out at the NOT from April 1998 to November 1999, except for a short period (i.e., from December 1998 to February 1999) where the object was below the horizon at the NOT. Three different instruments were used: ALFOSC (Andalucía Faint Object Spectrograph), HiRAC (High Resolution Adaptive Camera) and the stand-by camera StanCam, equipped with detectors yielding pixel scales of $0\farcs188$, $0\farcs107$ and $0\farcs176$ respectively. The I band was chosen to minimize the effect of the extinction of the B component by the lensing galaxy. The total exposure times for each data point were adjusted according to the moon phase and typically ranged from 20 to 40 min, divided into three dithered exposures. The seeing usually varied from $0\farcs7$ to $1\farcs4$, with $0\farcs9$ being the most frequent value. A typical signal-to-noise ratio (S/N) of 100 was reached for the A component and 50 for the B component. Color terms were determined for the three detectors in order to match the light curves obtained with the three instruments.

An automated pipeline employing routines in the IRAF/NOAO/CCDRED package has been developed in order to pre-process the CCD frames in an efficient and homogeneous way. Fringe-correction and cosmic-ray removal were performed

[1] Based on observations made with the Nordic Optical Telescope, operated on the island of La Palma jointly by Denmark, Finland, Iceland, Norway, and Sweden, in the Spanish Observatorio del Roque de los Muchachos of the Instituto de Astrofisica de Canarias.

on the individual frames before combination.

3. Photometry

The photometric data consist of one stacked frame per epoch. All light curves are calculated relative to 3 stars in the field that have calibrated I band magnitudes (Jaunsen & Hjorth 1997). Two of these stars, angularly close to the QSO, labeled S1 and S2 by Jaunsen & Hjorth (1997), are used to construct the Point Spread Function (PSF).

All the combined frames, one per epoch, are deconvolved with the MCS deconvolution algorithm (Magain, Courbin & Sohy 1998). With this technique, many frames of a single object can be simultaneously deconvolved. This procedure combines the total S/N of all the frames obtained at different periods to determine the light distribution of the extended sources (galaxies) as well as the positions of the point sources (QSOs), since these parameters do not vary with time. The intensities of the point sources, however, are allowed to vary from one image to the other, hence producing the light curves. This technique is particularly well suited for the analysis of B1600+434 because of the light contamination of the faint B component by the spiral lensing galaxy. Simultaneous deconvolution of all the frames allows us to derive a high signal-to-noise numerical galaxy model (see Fig. 1). The derived galaxy is in good agreement with the images of B1600+434 obtained with the Hubble Space Telescope (HST) (Maller et al. 2000).

Maps of the residuals for each frame are used to check deconvolution results. These maps represent the χ^2 fit in each pixel; i.e., the match between the deconvolved model image (reconvolved with the PSF) and the data. By inspecting these residuals we conclude that the photometry of both components was mainly limited by photon noise.

In order to check for errors introduced by the PSF we deconvolve two fainter stars in the field that are not used in the construction of the PSF. Light curves for two of these stars, labeled S3 and S4, are displayed in Fig. 2. Assuming that these stars are not variable, we use the standard deviation around the mean value as a measure of the photometric accuracy, giving 1σ errors of 0.026 mag and 0.039 mag for S3 and S4 respectively. For each point we subtract the photon noise in quadrature and attribute the residual error to the PSF. For the QSO images these estimated PSF errors are added in quadrature to the photon noise in order to model the total errors in the photometry.

4. Light curves

The I-band light curves (Fig. 2) contain 41 data points for each component. As predicted by lens theories, these light curves show that A is the leading component. A feature in A observed at JD 2451050 (September 1998) is repeated in B about 50 days later. In June 1999 ($\sim$ JD 2451300) there is an increase in the flux from both components. This increase is particularly strong in the B component and represents more than one magnitude in less than 100 days. After the intensity increase both A and B display several sharp short-term variations. Unfortunately our light curves are not sufficiently well-sampled during this period to recover the exact variations. This suggests that there are variations on time scales faster than the sampling frequency.

The features in the light curves are sufficiently distinct that a rough eye-ball estimate directly yields an approximate time delay of about 50 days. Although 41 brightness measurements are a fairly small amount of data, application of standard techniques to measure time delays yield fairly robust results. We analyzed the light curves with the four methods described below.

5. Time delay measurements

5.1. The SOLA method

The method of subtractive, optimally-localized averages (SOLA) was originally developed for solving inverse problems in helioseismology (Pijpers & Thompson 1994). The basic idea of this method is to construct an optimal solution, taking into account measurement errors, of any linear inverse problem by taking linear combinations of the measured data. After having been applied successfully in helioseismology the SOLA method has found application in image reconstruction (Pijpers 1999), in the reverberation mapping of active galactic nuclei (Pijpers & Wanders 1994), and in the determination of time delays between lensed QSOs (Pijpers 1997).

In the case of lensed quasar images, a transfer

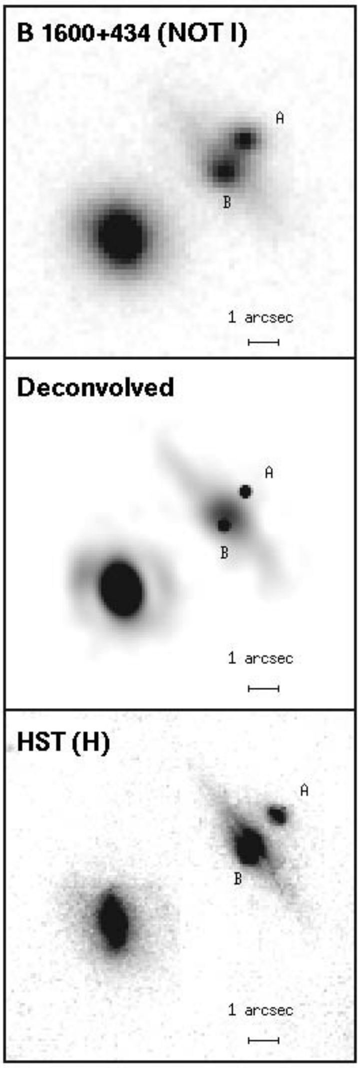

Fig. 1.— *Top*: Stacked I-band images of 12×12 arcsec around B1600+434 with a total of ~ 3.5 hours of exposure and a seeing FWHM = $1''.13$. *Middle*: The image (FWHM = $0''.38$) as obtained from the simultaneous deconvolution of 33 frames. The main lensing spiral galaxy can be seen between the two QSO components A and B. A neighbor galaxy is seen to the south east of the system. North is up and East is to the left. *Bottom*: The HST H band image.

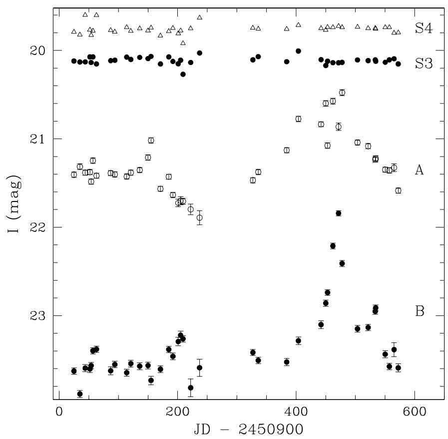

Fig. 2.— I-band light curves for B1600+434 (A and B component) and two reference stars in the field. The plotted value for B is I(mag)+1.5, and for S4 I(mag)+0.4. The magnitudes are calculated relative to calibrated stars in the field. The error bars represent photon noise and PSF errors measured as described in the text (§ 3).

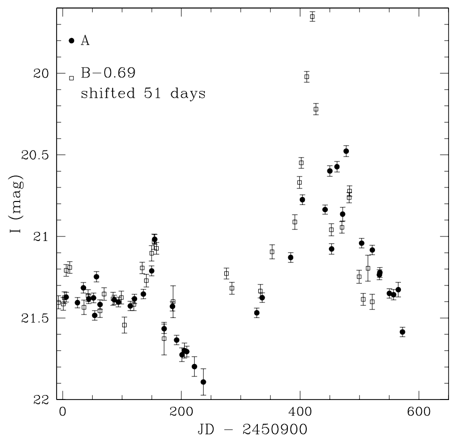

Fig. 3.— Combined lightcurve from both components of B1600+434. The curve from the B component is shifted forward in time by 51 days and scaled with −0.69 mag. The magnitudes are calculated relative to calibrated stars in the field. The error bars represent photon noise and PSF errors measured as described in the text (§ 3).

function which is a Dirac delta function is positioned at the time delay. With this method both the delay and the relative magnification of a pair of images are determined. Applied to B1600+434 a time delay of 55 days and a flux ratio of 0.79 is found. Also determined is a relative offset, for instance due to a contribution of the lensing galaxy or a foreground object which has not been subtracted, and a (linear) drift between the images which could occur due to microlensing events with long time scales. Problems can occur if there are higher order relative drifts such as short time-scale microlensing events which cannot easily be accounted for within this method which just uses determinations of low order moments of the transfer function.

The errors are obtained by assuming that the photometric errors are uncorrelated and follow a Gaussian distribution. These propagated errors give a conservative error estimate of ±10 days on the time delay value, i.e., $\Delta t = 55 \pm 10$ days.

5.2. The minimum dispersion method

For the combined data set generated from the A light curve and the shifted B light curve, we estimate the dispersion of the scatter around the unknown mean curve. The true time delay between the images should be manifested as a minimum in the dispersion spectrum (see Pelt et al. (1996) for definitions and notation). Both the simplest string length type statistic D_2^2 and the smoothed dispersion spectrum D_3^2 (smoothing parameter $\delta = 10$ days) give a clear global minimum at $\Delta t \approx 48$ days.

The precision of this time delay value is estimated using a bootstrap procedure. We first construct the combined light curve from A and the time-delay shifted B curve ($\Delta t = 48$). This yields a reference curve by median smoothing. From the reference curve we build bootstrap samples by adding randomized errors. For each sample (altogether 1000) we compute D_3^2 dispersion spectra and find corresponding dispersion minima. The scatter of the dispersion minima for the different bootstrap runs is significant (see Fig. 4), with a formal 1σ error estimate of ±16 days.

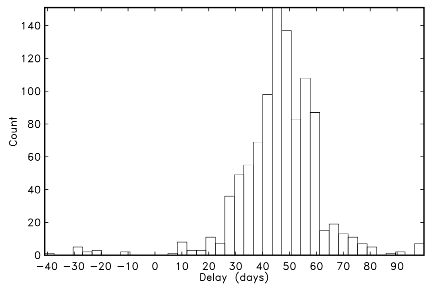

Fig. 4.— Distribution of the time delays for 1000 bootstrap runs with the minimum dispersion method (see § 5.2).

5.3. Model fit method

We model the data with an arbitrary continuous light curve with a fixed and constant sampling. For a given time delay value Δt, we use χ^2 minimization to compare the model curve to the A curve and the appropriately time delay shifted and magnitude offset B curve. Additionally, a linear term in one of the curves can be included to model long term microlensing effects such as observed in QSO 0957+561 (Schild & Smith 1991). The minimization procedure is repeated for a range of time delay values (0 to 100) and the χ^2 minimum is obtained with $\Delta t = 49$ days and $\Delta m = 0.66$ magnitudes (i.e., a flux ratio of 0.54). An additional small positive linear term for the A component further improves the χ^2 value.

A bootstrap method is used to estimate the errors. Two sets of 1000 curves are constructed with the same number of data points as in the data. One set is constructed with the same time sampling as that of our measured data, and the other with a random time sampling. Running the program on these simulated curves results in a 1σ standard deviation of 2 days on the set of curves with the same sampling as our measured data, and of 7 days on the curves with random sampling. We could interpret this as an error of 2 days internal to the method since the sampling stayed the same for each simulated data set, and an error of 7 days on the measured time delay independently of the sampling of the data, but this needs to be investigated further.

5.4. Iterative modeling

Assuming that the additional time dependent offsets between the time-delay shifted curves are caused by microlensing, a fourth method based on iterative correction of the flux ratios is applied to the data. We split the light curves into several parts (bins). In one case we chose three bins with lengths determined according to the apparent lengths of the offsets in a certain directions (positive or negative compared to the other curve). In three other cases we separate the curves into 2,3 and 4 bins with an equal number of data points. For a range of time-delay values (40 – 65 days) we first fit a model (using the χ^2 model fit method described above) independently to the separate bins. For each bin and time delay value, an additional constant or linear offset is determined to improve the fit. Finally, new time delay values are determined on these modified curves. The time delays determined in this way turn out to show very little sensitivity to the input values used, and to the different splitting of the curves. The results converge towards a mean value of 51 days with a standard deviation (1σ) of 2 days and magnitude offsets varying from 0.6 – 0.87 mag in the different bins.

5.5. Results

The four time-delay estimates obtained from the different methods are consistent with one another (see Table 1). An average of the results gives a time delay estimate of 51 days and a flux ratio $A/B = 1.50$. The flux ratio at radio wavelengths has been measured to be 1.21 (Koopmans et al. 2000). If we assume that the radio flux is not affected by reddening, the B-component is reddened by 0.22 magnitudes, corresponding to a factor of 1.23. At a redshift of 0.41, this corresponds to $A_V \sim 0.25$ mag, essentially independent of the assumed reddening law.

Except from the iterative modeling, the methods described above yield substantial errors in the time delay. However, the good agreement between the results in addition to the observed time dependent magnitude offsets in the time-delay shifted curves (Fig. 3) suggest that the large errors are mostly due to the presence of external variations, e.g., microlensing effects, rather than to the method used to determine the time delay.

SOLA and the model fit method correct for slow, linear variations, but not higher order effects. Let us consider a case in which the brighter of the two lensed images undergoes many microlensing events during the time of monitoring. Such short term variations would be indistinguishable from measurement noise for these methods. They may fail to converge or produce a result that is biased at a level of the order of the errors. With the iterative method however, we also correct for higher order effects. The small errors from the iterative method compared to the other three methods indicate the presence of such higher order external variations in the light curves.

If no assumptions are made on the short term offsets between the time delay shifted curves we must use the conservative error estimate of ± 10 days (1σ) on the time delay value. However, if we assume that these external variations are higher order effects we can use the 1σ error estimate of ± 2 days as found from the iterative method.

6. H_0 estimate

Assuming that microlensing effects affect our I band light curves, a time delay of 51 ± 4 (95% confidence level) days has been estimated. Applying the galaxy models from Maller et al. (2000), and assuming a $\Omega = 0.3$ and $\Lambda = 0$ Universe, our measured time delay is consistent with a Hubble parameter of $H_0 = 52^{+14}_{-8}$ km s^{-1} Mpc^{-1} (95% confidence level) where both errors on the model and the time delay are included.

In the model of B1600+434, Maller et al. (2000) assume a constant M/L for the disk and the bulge, and a dark halo that has the same center and the same orientation as the disk. In addition they include the mass associated with the companion galaxy (see Fig 1) modeled as an isothermal sphere. The dark matter is modeled as a standard Pseudo Isothermal Elliptical Mass Distribution (Kassiola & Kovner 1993, PIEMD), and the exponential profiles of the disk and the bulge are modeled by a two-point PIEMD, also called the chameleon profile (Keeton & Kochanek 1998; Hjorth & Kneib 1999). Two types of solutions are found with these models, one with a large dark-matter halo core radius, and the other with a nearly singular dark halo. Applying only the solutions with a large dark halo core radius give $H_0 = 54^{+6}_{-5}$ km s^{-1} Mpc^{-1}.

For comparison we also estimate H_0 using a simple analytical generalized isothermal galaxy model as described by Witt et al. (2000). This method depends only on the time delay and the observed images positions. Using our measured time delay and the image positions from Maller et al. (2000) measured on the HST image we obtain $H_0 = 45^{+6}_{-5}$ km s^{-1} Mpc^{-1} ($\Omega = 0.3$ and $\Lambda = 0$) where errors come only from the time delay and the image positions. This is only an indicative estimate of H_0 using a very simplified model. Possible shear from ellipticity in the lens galaxy or mass contribution from the companion galaxy is not taken into account.

Finally, as pointed out by Romanowsky & Kochanek (1999) and Witt et al. (2000), the time delay depends on the density profile of the lens galaxy. Hence if the real density profile of the spiral galaxy is different from our models the errors in H_0 will increase.

7. Discussion

The main goal of our optical monitoring program at the NOT is to measure time delays for as many lensed QSOs as possible in order to better constrain the mass distribution in lens galaxies. A robust time delay value of $\Delta t = 51 \pm 10$ (1 σ) days and a flux ratio of 0.69 have been measured from I band light curves of our first target B1600+434. Assuming that our lightcurves are affected by external variations the time delay value is constrained to 51 ± 4 days (95% confidence level). This value is consistent with a Hubble parameter $H_0 = 52^{+14}_{-8}$ km s^{-1} Mpc^{-1} ($\Omega = 0.3$, $\Lambda = 0$) using the models of Maller et al. (2000). We recall that possible systematic errors due to uncertainties in the density profiles and the degeneracy between the relative contribution of disk, bulge and halo to the mass in the spiral galaxy may increase the uncertainties in the estimated H_0.

As is evident from Fig. 3, and as measured by the various methods to determine the time delay, there are slow additional time dependent magnitude offsets between the curves. These variations are ~0.2 mag on time scales of a few months. Since the QSO images of B1600+434 pass through the lens galaxy with high optical depths for microlensing, the offsets between the two time-delay shifted curves (Fig. 3) are likely to be due to microlensing of one of the components. This interpretation is supported by the detection of microlensing in light curves obtained at radio wavelengths (Koopmans et al. 2000), and implies that a significant fraction of the mass in the dark halo consists of massive compact objects. Simulations of microlensing light curves must be carried out in order to determine the lens masses and source sizes that could reproduce the observed variations in our optical light curves (see Wambsganss & Paczyǹski (1991) and Schmidt & Wambsganss (1998)). Such a microlensing analysis will be published in a separate paper.

Microlensing could also be partly responsible for the sharp event at ~JD2451350 in the light curve of the B component. Such high magnification and short duration events may occur in cases of microlensing by stars in random motion whereas the slow variations are typical for microlensing events by the stars with velocities following the bulk motion of the galaxy (e.g., Wambsganss & Kundić 1995). We note however that much of this event must be due to intrinsic variations in the QSO since a significant peak is detected for both components.

Although the temporal sampling of our curves does not allow to fully disentangle high frequency microlensing and intrinsic variations, it is sufficient to follow lower order variations, yielding robust time delay estimates fairly independently of the statistical method used. The time delay estimates measured with the four different methods are in agreement with each other. Furthermore, the time delay value of 47^{+12}_{-9} days recently estimated from radio measurements Koopmans et al. (2000) is consistent with our optical measurement. There are thus two independent data sets, one at optical wavelengths (I band) and one at radio wavelengths, hence affected in very different ways by microlensing, yielding the same time delay value within the measurement errors.

The remarkably strong variations in this system makes it interesting to study in more detail. The observed microlensing effects may provide important constraints on the MACHO masses in the lens galaxy. Moreover, once H_0 is known independently from other lenses, or other methods, an accurate time delay can be used to constrain the mass distribution between the halo and the bulge of the spiral lens galaxy. In particular, a well determined time delay and flux ratio can contribute to determine the maximum allowed disk mass in the lens galaxy.

We thank the NOT Director Vilppu Piirola for granting us observing time for this project on a flexible basis. We are especially grateful to the dozens of visiting observers at NOT who have contributed to this project by performing the scheduled observations. This project was conceived in 1997 while JH, AOJ, and JP were visiting scientists at the Center for Advanced Study in Oslo. We thank Rolf Stabell and Sjur Refsdal for inviting us there and for their kind hospitality. We also acknowledge stimulating conversations with Frederic Courbin and the useful comments from the referee. The project was supported in part by the Danish Natural Science Research Council (SNF). IB was supported in part by contract ARC94/99-178 "Action de Recherche Concertée de la Communauté Française (Belgium)" and Pôle d'Attraction Interuniversitaire, P4/05 (SSTC, Belgium).

REFERENCES

Fassnacht, C. D. & Cohen, J. G. 1998, AJ, 115, 377

Hjorth, J., Burud, I., Jaunsen, A. O., Andersen, M. I., Korhonen, H., Clasen, J. W., Østensen, R. 1999, proceedings of the conference held in Boston 25-30 July, 1999: Gravitational Lensing: Recent progress and future goals.

Hjorth, J., & Kneib, J.-P. 1999, ApJ, submitted

Jackson, N. et al., 1995, MNRAS, 274, L25

Jaunsen, A. O. & Hjorth, J. 1997, A&A, 317, L39

Kassiola, A., & Kovner, I. 1993, ApJ, 417, 450

Keeton, C. R., & Kochanek, C. S. 1998, ApJ, 495, 157

Koopmans, L. V. E, de Bruyn, A. G, Xanthopoulos, E., & Fassnacht, C. D. 2000, A&A, 356, 391

Kundić, T. et al., 1997, ApJ, 482, 75

Magain P., Courbin F., & Sohy S. 1998, ApJ, 494, 472

Maller A. H., Simard, L., Guhathakurta, P., Hjorth, J., Jaunsen, A. O., Flores, R. A. & Primack, J. R. 2000, ApJ, 533, 194

Pelt J., Hoff, W., Kayser, R., Refsdal, S. & Schramm, T. 1994, A&A, 286, 775

Pelt J., Kayser R., Refsdal S. & Schramm, T. 1996, A&A, 305, 97

Pijpers F. P. 1997, MNRAS, 289, 933

Pijpers F. P. 1999, MNRAS, 307, 659

Pijpers F. P. & Thompson M. J. 1994,A&A, 281, 231

Pijpers F. P. & Wanders I. 1994, MNRAS, 271, 183

Refsdal S. 1964, MNRAS, 128, 295

Romanowsky, A. J. & Kochanek, C. S. 1999, ApJ, 516, 18

Schechter, P. L. et al., 1997, ApJ, 475, 85

Schild, R. E. & Thomson, D. J. 1997, AJ, 113, 130

Schild, R. E. & Thomson, D. J. 1995, AJ, 109, 1970

Schild, R. E. & Smith, R. C. 1991, AJ, 101, 813

Schild, R. E 1990 AJ, 100, 1771

Schmidt, R. & Wambsganss, J. 1998 A&A, 335, 379

Wambsganss, J. & Paczyǹski, B. 1991, AJ, 102, 864

Witt, H. J., Mao, S. & Keeton, C. R. 2000, submitted, preprint astro-ph/0004069

This 2-column preprint was prepared with the AAS LATEX macros v5.0.

Chapter 6

Article presenting the time delay measurement in HE 2149-2745

An optical time-delay for the lensed BAL quasar HE 2149-2745

I. Burud, F. Courbin, P. Magain, C. Lidman, D. Hutsemékers, J.-P. Kneib, J. Hjorth, J. Brewer, E. Pompei, L. Germany, A. O. Jaunsen, G. Letawe, G. Meylan

Submitted to Astronomy & Astrophysics

Astronomy & Astrophysics manuscript no.
(will be inserted by hand later)

An optical time-delay for the lensed BAL quasar HE 2149−2745 ⋆

I. Burud[1], F. Courbin[2], P. Magain[1], C. Lidman[3], D. Hutsemékers[3⋆⋆], J.-P. Kneib[4], J. Hjorth[5], J. Brewer[3], E. Pompei[3], L. Germany[3], A. O. Jaunsen[3], G. Letawe[1], and G. Meylan[6]

[1] Institut d'Astrophysique et de Géophysique, Université de Liège, Avenue de Cointe 5, B–4000 Liège, Belgium
[2] Universidad Católica de Chile, Departamento de Astronomia y Astrofisica, Casilla 306, Santiago 22, Chile
[3] European Southern Observatory, Casilla 19, Santiago, Chile
[4] Observatoire Midi-Pyrénées (LAS), UMR 5572, 14 avenue E. Belin, 31400 Toulouse, France
[5] Astronomical Observatory, University of Copenhagen, Juliane Maries Vej 30, DK–2100 Copenhagen Ø, Denmark
[6] Space Telescope Science Institute, 3700 San Martin Drive, Baltimore, MD 21218, USA

Abstract. We present optical V and i-band light curves of the gravitationally lensed double BAL quasar HE 2149−2745. The data, obtained at the 1.5m Danish Telescope (ESO-La Silla) between October 1998 and December 2000, are the first of a long term project aimed at monitoring selected lensed quasars in the Southern Hemisphere. A time delay of 103 ± 12 days is determined from the light curves. In addition, VLT/FORS1 spectra of HE 2149−2745 were deconvolved in order to obtain the spectrum of the faint lensing galaxy, free of any contamination by the bright nearby quasar images. By cross-correlating the spectrum with galaxy-templates we obtain a tentative redshift estimate of $z = 0.489$. Adopting this redshift, a $\Omega = 0.3$, $\Lambda = 0.7$ cosmology, and a chosen analytical lens model, our time-delay measurement yields a Hubble parameter of $H_0 = 66 \pm 6\,\mathrm{km\,s^{-1}\,Mpc^{-1}}$ with a possible systematic error of $\pm 3\,\mathrm{km\,s^{-1}\,Mpc^{-1}}$. Using non-parametric models yields $H_0 = 65 \pm 7\,\mathrm{km\,s^{-1}\,Mpc^{-1}}$ and confirms that the lens exhibits a very dense/concentrated mass profile. Finally, we note, as in other cases, that the flux ratio between the two quasar components is wavelength dependent. While the flux ratio in the broad emission lines remains constant – and equal to 3.7 – with wavelength, the continuum of the brighter component is bluer. Although the data do not rule out extinction of one quasar image relative to the other as a possible explanation, the effect could also be produced by differential microlensing by stars in the lensing galaxy.

Key words. Gravitational lensing – quasars: individual: HE 2149−2745 – cosmological parameters

1. Introduction

The time-delay between the gravitationally lensed images of a distant source is a measurable parameter. Observed as the time difference between the arrival dates of a single (lensed) wavefront emitted by a distant source, it is directly related to the Hubble parameter H_0 (Refsdal 1964). Obtaining accurate time delay measurements in multiply lensed quasars can therefore yield **(i)** a determination of H_0 provided the mass distribution in the lens is known, or **(ii)** constraints on the mass distribution in a given lens, using H_0 as inferred from other methods. Much effort has been devoted to the observations of lensed quasars during the last 20 years, and in particular to long term monitoring of selected systems. In this context, we have been conducting a photometric monitoring program at the Danish 1.5-m telescope at La Silla observatory (Chile) since October 1998, with the goal of measuring the time-delays in several well studied lensed quasars. We present here the first result from this program: the time-delay measurement in the double quasar HE 2149−2745.

The lensed nature of the BAL quasar HE 2149−2745 at $z = 2.03$ was established by Wisotzki et al. (1996). This system proves to be an easy target for monitoring: it is bright ($B = 17.3$) and the two quasar images have an angular separation of $1.7''$. The monitoring program, the light curves and the time delay are discussed in Sect. 2.

The lensing galaxy has been detected in HST NICMOS and WFPC2 images but its redshift remains unknown. With the aim of measuring this redshift, we have obtained a spectrum of HE 2149−2745 with FORS1 at UT1 (ESO-Paranal, Chile). The analysis of the spectroscopic data is described in Sect. 5. This section also includes a discussion on the spectral differences between the two quasar compo-

Send offprint requests to: I. Burud

⋆ Based on observations made with the Danish 1.5-m telescope (ESO, La Silla, Chile) and at VLT UT1 Antu (ESO-Paranal, Chile)

⋆⋆ also Research Associate FNRS at the University of Liege, Belgium

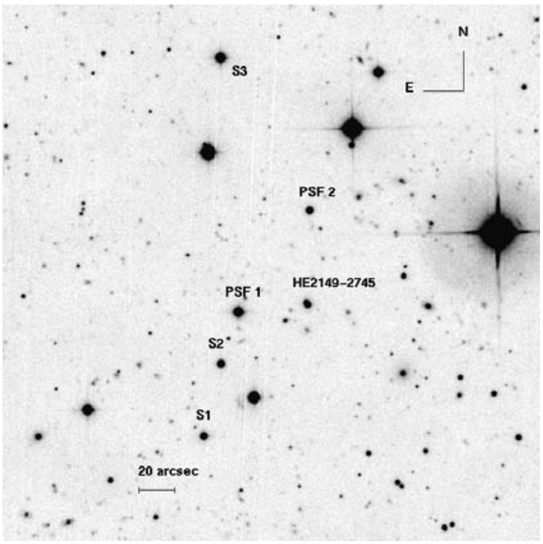

Fig. 1. Field of view of 5 arcmin centered on HE 2149−2745. The three reference stars used for the photometry and the two PSF-stars used in the spectral deconvolution are indicated. North is up and East to the left.

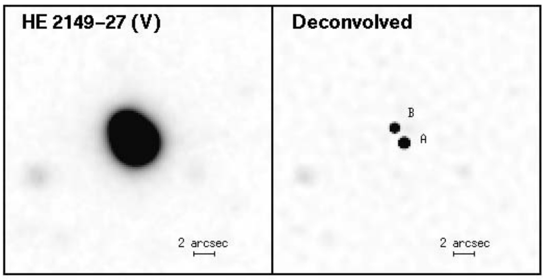

Fig. 2. *Left*: Stacked V-band image of a 9″x 9″region centered on HE 2149−2745. The seeing is ∼2″ and the total exposure time is ∼ 17 hours. *Right*: Deconvolved image (FWHM=0.″4) obtained from the simultaneous deconvolution of 57 frames. North is up and East is to the left.

Table 1. Positions of three reference stars relative to the position of the A component in HE 2149−2745.

Star	R.A. (arcsec)	DEC (arcsec)
S1	-48.126	136.268
S2	-57.126	-72.647
S3	-38.160	-4.145

nents. Mass models and estimates of the Hubble Constant are presented in Sect. 6. Finally, Sect. 7 summarises the main results.

2. Photometric Monitoring at the 1.5m Danish Telescope

2.1. Observations and Data Reduction

Weekly observations of HE 2149−2745 were carried out at the Danish 1.5-m telescope at ESO-La Silla from October 1998 to December 2000. The target is visible from the beginning of June to the end of December, which results in gaps of about ∼ 5 months in the light curves. Apart from these gaps, very few points were missed because of poor weather or technical problems. Observations were obtained in the V and *Gunn i* bands with DFOSC (Danish Faint Object Spectrograph Camera) which has a pixel size of 0.″395. Fig. 1 shows the central region of the field of view of DFOSC, i.e., 5 arcmin of the 13 available. The V-band was given priority because of the detector's better sensitivity at this wavelength, but observations were also carried out in the i-band in order to monitor possible colour changes. The exposure time was set to 900 sec during the first 6 months of observations. It was increased to 1800 sec for the rest of the observations in order to improve the photometric quality for the fainter quasar image. For each observed data point the total exposure time was divided into three dithered exposures in order to remove cosmic rays and bad pixels. The seeing varied from 0.″7 to 2.″9, with a median of 1.″6. All the imaging data were preprocessed (bias-subtracted and flat-field corrected) using standard IRAF routines.

3. Photometry

The photometry of the blended quasar images were performed by applying the MCS deconvolution algorithm (Magain, Courbin & Sohy 1998). This algorithm has already been used to analyze the data of several lensed quasars (e.g., Burud et al. 2000, Hjorth et al. 2000). Its main advantage is its ability to use all the data, even poor data, irrespective of image quality and lunar phase. The final deconvolved image is produced by simultaneously deconvolving all the individual frames of the same object from all epochs. The positions of the quasar images (two in the present case) and the shape of the lensing galaxy are the same for all the images and are therefore constrained using the total S/N of the whole data-set. The intensity of the point sources are allowed to vary from image to image, hence producing the light curves.

The two quasar components are well separated in our deconvolved image of HE 2149−2745 (see Fig. 2), but the lensing galaxy remains too faint to be detected. This is fortuitous since contamination by an extended object would complicate the analysis.

The light curves of HE 2149−2745 consist of 57 data points in the V-band and 41 points in the *Gunn i* band, as presented in Fig. 3. The points from JD 2451800 to JD 2451900 were obtained just after the installation of the new chip on DFOSC. The new chip does not have problems of charge diffusion, as the old chip had, and consequently, the seeing is now considerably improved. Our original PSF star therefore became saturated and another

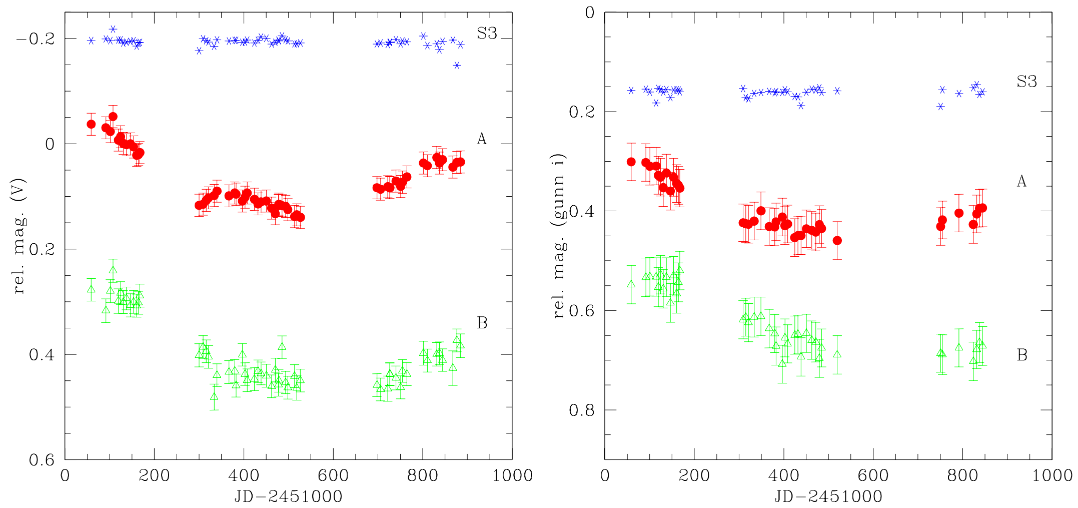

Fig. 3. Light curves of HE 2149−2745 and the comparison star S3 (Table 1). The V-band light curves are displayed on the left while the *Gunn i*-band light curves are shown on the right. The magnitudes of the quasar and star S3 are calculated relative to the reference star S2. The error bars include photon noise and PSF errors estimated from the deconvolution of a reference star. For display purposes, the B component is shifted by −1.3 mag. and −1.2 mag. in the V and *Gunn i* band respectively, with respect to their original values. Likewise, S3 is shifted by +1.1 and +0.1 mag in the V and *Gunn i* filters.

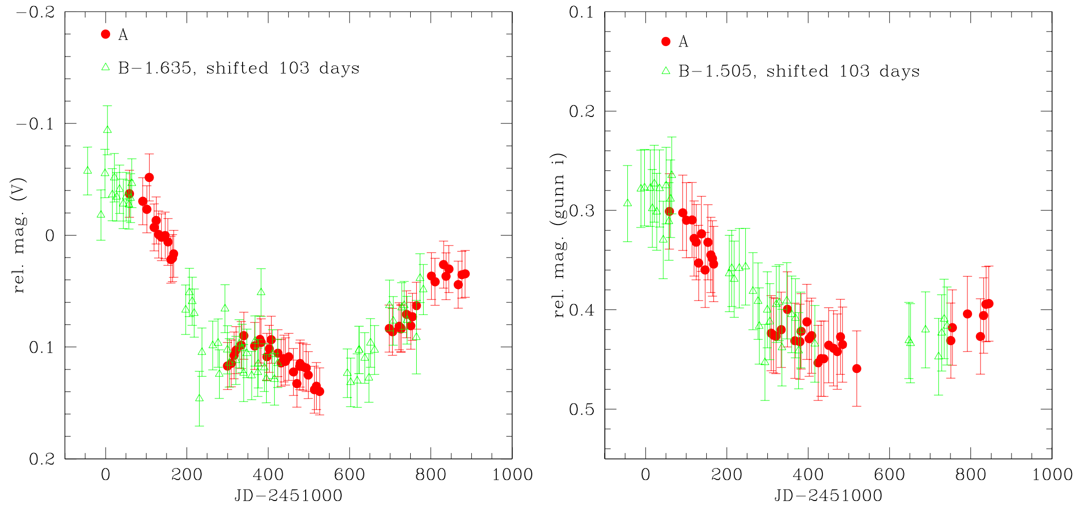

Fig. 4. The V and i-band light curves where the B curve is shifted by 103 days. The curve of component B is shifted 1.635 and 1.505 magnitude in the V and i-band respectively, with respect to their original values. The curves for the A component is as in Fig. 3

PSF star, further away from the target, had to be used on a few frames before the exposure time was adjusted to the new chip. These points are therefore more noisy than the previous points.

The data are plotted relative to a reference star common to all images, star S2 in Table 1. Two other stars were deconvolved as well, in order to check the relative photometry and to check for systematic errors (see Table 1 for the positions of the stars). The error-bars include both photon noise and additional systematic errors, e.g., PSF errors. The latter is estimated by using one of the reference stars, as explained in Burud et al. (2000).

4. time-delay measurement

By sliding the light curves across one another, one can make a rough "by eye" estimate of the time-delay of ~ 100 days, with A leading B. Using the χ^2 minimization method described in Burud et al. (2000), a more objective value of $\Delta t = 103 \pm 12$ days is found from the V-band light curves. The i-band data are noisier and have fewer data points but the measured time-delay, $\Delta t = 104 \pm 31$ days, agrees well with the delay derived from the V-band. The errors quoted here are obtained from Monte Carlo simulations of 1000 sets of light curves, assuming that the photometric errors are uncorrelated and follow a Gaussian distribution. The χ^2 minimization method was also performed on 1000 sets of curves where 5 randomly chosen data points were removed from each set. The results from these simulations yielded a time-delay of $\Delta t = 101 \pm 30$ and $\Delta t = 107 \pm 30$ in V and I respectively, confirming that the time-delay measurement is robust. The magnitude differences between the A and the B components are found to be 1.635 ± 0.001 mag in V and 1.505 ± 0.003 mag in the i-band. This corresponds to flux ratios of 4.51 and 4.00 in V and i bands respectively Although no erratic changes are detected in the light curves within the measurement errors, microlensing on long time scales may still be present as suggested by the VLT spectra presented in Sect. 5). Fig. 3 summarizes the photometric data and Fig. 4 displays the V and i-band light curves of component B shifted by 103 days. Given that the V-band data contain more points and are less noisy than the i-band data, we take the V-band estimate of the time-delay as the best one: $\Delta t = 103 \pm 12$ days.

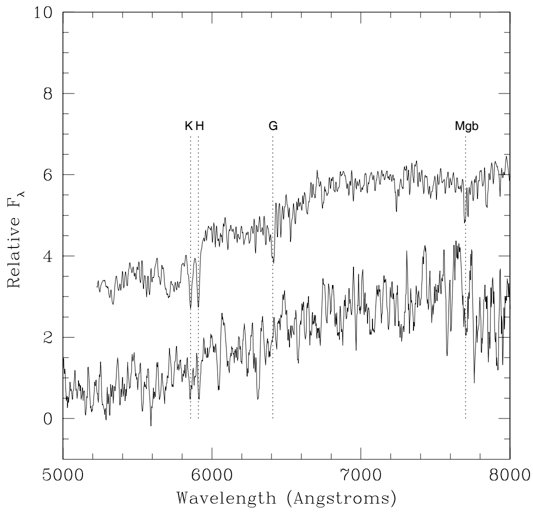

Fig. 5. Extracted spectrum of the lensing galaxy and the template spectrum from Kinney et al. (1996) used in the cross correlation. The main spectral features are indicated by the dashed vertical lines. The lens redshift is tentatively $z = 0.489$.

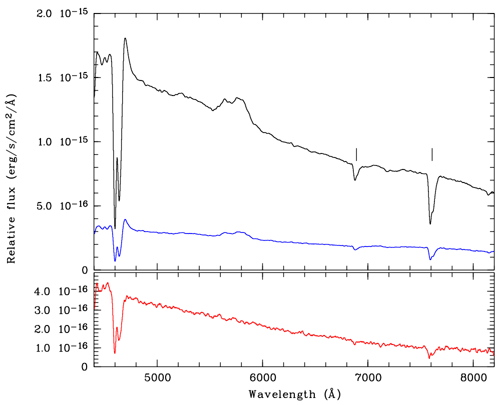

Fig. 6. *Top*: spectra of the A and B components. *Bottom*: the spectrum showing A−3.7×B. The scaling factor is chosen to best cancel the emission lines. Telluric absorption lines are indicated

5. Spectroscopy of HE 2149−2745

5.1. VLT spectroscopy

To convert the time-delay into an estimate of the Hubble Parameter, one must know the geometry of the lensing system and this includes the redshift of the lensing galaxy. For this purpose, we took an optical spectrum of HE 2149−2745 with the ESO VLT/UT1 using the Multi-Object-Spectroscopy (MOS) capability of FORS1. The observations were obtained on November 19, 2000 under fairly good seeing conditions (0.8″). The 1″ slitlets of FORS1 were aligned to obtain simultaneously the spectrum of HE 2149−2745 and of 2 PSF stars (indicated in Fig. 1) about as bright as the two quasar images. The high resolution collimator was used, resulting in a pixel size of 0.1″, in combination with the G300V grism and GG435 order sorting filter. Three exposures, each of 1000s, were taken so that cosmic rays could be removed.

5.2. Redshift of the lensing galaxy

Using the spatial information in the spectra of the two PSF stars, the spectrum was spatially deconvolved with the spectral version of the MCS deconvolution method (Courbin et al. 2000). The deconvolution process decomposes the data into the individual spectra of the two quasar images and the faint lensing galaxy (see Figs. 5 and 6), as done for example by Lidman et al. (2000) for HE 1104-1805.

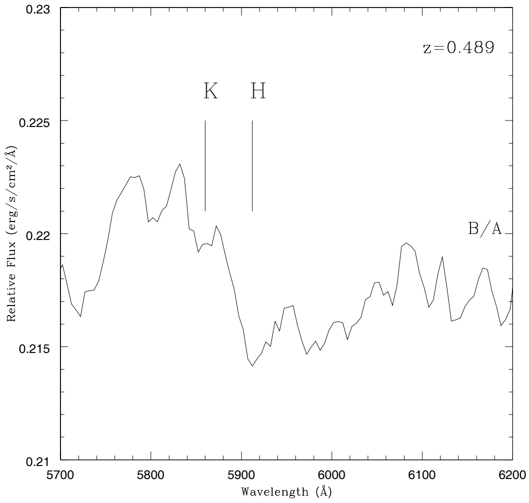

Fig. 7. Spectrum of the B component divided by that of the A component of HE 2149−2745. The plot shows a zoom on the region corresponding to possible Calcium H and K absorption due to the lens at $z = 0.489$. The bump between 5750 and 5900 Å is the residual CIII]+AlIII emission from the quasar.

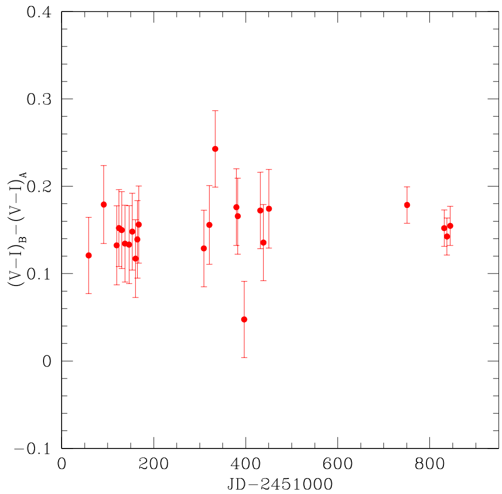

Fig. 8. Colour excess of B component relative to the A component, $(V-I)_B - (V-I)_A$ as a function of time. No significant variations can be detected over a period of 900 days.

The lens spectrum was cross-correlated with a template spectrum of an elliptical galaxy (Kinney et al. 1996. For this we used the IRAF task RVSAO v2.0 (Kurtz and Mink 1998). The redshift is $z = 0.489 \pm 0.002$, where the error incorporates the internal error reported by the cross-correlation routine. The spectrum of the lens and the template are shown in Fig. 5, where the template has been shifted vertically for clarity. The Calcium H and K lines, the G-band and the Mg triplet are labeled. A measure of the reliability of the redshift estimate is given by the r-statistic of Tonry and Davis (1979), which is the signal-to-noise ratio of the main peak in the cross correlation. We find that $r = 1.9$. A value above 3 is considered secure (Kurtz & Mink 1998).

As the lensing galaxy lies very close to the B image, we looked for evidence of absorption in the spectrum of the background quasar. In order to remove the quasar spectral features, the B spectrum was divided by that of the A component (Fig. 7). Two, possible Ca H & K candidates were found, one at $z = 0.489$ and another at $z = 0.504$. An integrated A+B spectrum at similar resolution but covering shorter wavelengths has been published by Wisotzki et al. 1996. We looked for possible MgII absorption in the quasar spectrum at the putative redshift of the lens. Unfortunately, the $z = 0.489$ line would fall in a strong absorption line of the quasar, while a candidate at $z = 0.504$ is found in the wing of a quasar emission.

Since the signal-to-noise ratio of the lens galaxy and the Ca H and K absorption features in the B component are very low, we propose a tentative redshift of $z = 0.489$ for the lensing galaxy. This is within the estimated redshift range $0.37 \leq z \leq 0.50$ which is based on the position of the lens in the fundamental plane (Kochanek et al. 2000).

5.3. Spectroscopy of the quasar images: colour differences, extinction or microlensing ?

The quasar spectra show that continuum of component A is bluer than the continuum of component B (Fig. 6). This confirms the difference in flux ratio that was found from the light curves in the V and *Gunn* i-bands (Sect. 4). We note three points of interest about these spectral differences:

1. As shown in Fig. 8 the colour difference between the quasar images does not vary during the period of our observations ($\sim$ 3 years).
2. The emission line flux ratios at the date of the observation are not wavelength dependent: all emission lines cancel in the difference spectrum of Fig. 6. This difference spectrum has been produced by multiplying the spectrum of the B component by a *constant* factor of 3.7 and by subtracting it from the spectrum of the A component. Fig. 9 gives a different representation of the same effect, where the spectra of the two quasar images are normalized to the same continuum. The equivalent widths of all emission lines (including the FeII pseudo-continuum) are smaller in A.
3. The CIV broad absorption line behaves as the continuum: its equivalent width is unchanged in the A and B spectra (Fig. 9).

The spectral differences cited above have essentially two explanations: (*i*) differential amplification due to microlensing, or (*ii*) differential reddening of the B component by the lensing galaxy.

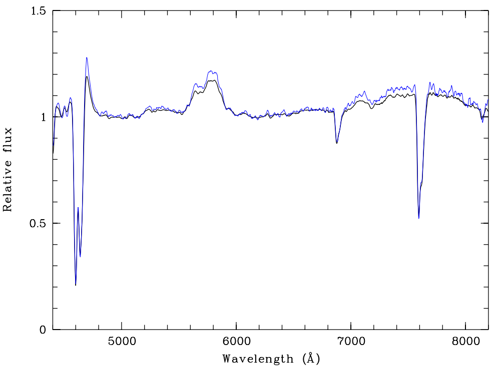

Fig. 9. The A (solid) and B (dotted) spectra normalized to a common continuum. The equivalent widths of the emission lines, including the FeII pseudo-continuum, are smaller in A. The equivalent width of the CIV broad absorption line is the same in both the A and B components.

5.3.1. Microlensing

If microlensing is present in HE 2149−2745, one expects the continuum region and the much more extended emission lines region to be affected differently. In most AGN models, the size of the continuum region depends on wavelength, and the Broad Emission Line Region (BELR) is usually believed to be larger than the continuum region by more than one order of magnitude. Since the B component is closest to the lensing galaxy we would expect that microlensing effects occur most often in the B-component. Microlensing of the A component however is also possible.

Assuming the lensed quasar in HE 2149−2745 follows the "standard" AGN model and that we are observing component A through a network of caustics produced by stars in the main lensing galaxy, one can imagine a scenario where the inner – and bluer – continuum region of the component A is being enhanced by a larger amount than the outer redder parts. As the BELR is much larger than the central AGN (even the redder parts), it remains unaffected by microlensing. This interpretation has already been proposed to explain similar spectral differences observed in the double HE1104-1805 (Wisotzki et al. 1993, 1995, Courbin et al. 2000).

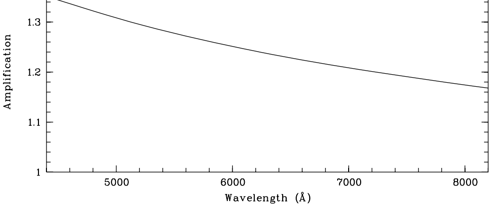

Fig. 10. The amplification μ of A relative to B as a function of wavelength. This amplification factor is derived by fitting the A/B continuum ratio after correcting the B spectrum by the constant factor 3.7 (as in the lower panel of Fig. 6)

The spatial scale for microlensing is set by the mean angular distance between the caustics in the source plane. This is close to the Einstein radius of a typical deflector in the lens plane projected onto the source plane. In HE 2149−2745 this radius is ($\Omega = 0.3$, $\Lambda = 0$):

$$R_E = \sqrt{\frac{4GM}{c^2}\frac{D_{ds}D_s}{D_d}} = 1.3 \times 10^{-3}(M/0.1M_{\odot})^{1/2}\mathrm{pc} \quad (1)$$

where D_d, D_s and D_{ds} are angular diameter distances to the deflector, the source and between deflector and source respectively, and M is the mean mass of all microlenses. The duration of a caustic crossing will be up to 10 years assuming a relative velocity between source and lens that is equal or larger than the velocity in the lensing galaxy which is the order of $\sim (100 - 400)\mathrm{kms}^{-1}$ (Mould et al. 1993). The effect may therefore be present in our data, and stable over our relatively short period of observation of 900 days, as Fig. 8 would suggest.

Assuming that the continuum of A is amplified by microlensing, we may derive the wavelength dependence of the amplification from the A/B continuum ratio. This relative amplification factor μ is given in Fig. 10. It is derived by fitting the A/B continuum ratio after correcting the spectrum of B by the constant factor 3.7. The relative amplification is directly related to the size of the continuum region as a function of wavelength (e.g. Schneider et al. 1992), the precise measurement of which requires the knowledge of the background amplification μ_0 due to other distant subimages. While μ can be estimated from Fig. 10, μ_0 can only be obtained by measuring the background amplification before and after a caustic crossing event. This can be done with a spectrophotometric monitoring. In Fig. 11, we have plotted the amplification factor – expressed as a magnitude difference – as a function of the inverse wavelength. It shows a remarkably tight wavelength dependence strikingly similar to that found by Nadeau et al. (1999) for Q2237+0305. This suggests that HE 2149−2745 presently suffers a chromatic microlensing event similar (although of much longer duration) to the 1991 high-amplification event in Q2237+0305 and which was interpreted – on the basis of its colour dependence – as evidence for the thermal accretion disk model as the source of UV-visible continuum emission in quasars (cf. Nadeau et al. 1999).

While broad emission lines should be essentially unaffected by the caustic crossing, some subtle differences may arise in the line profiles if some parts of the BELR are selectively magnified (Nemiroff 1988, Schneider & Wambsganss 1990). Looking in detail at the line profiles

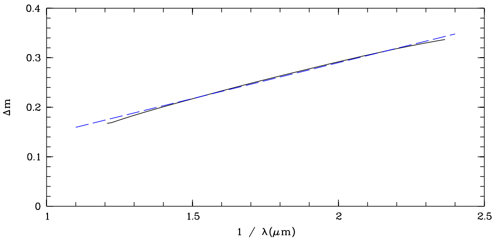

Fig. 11. The amplification of component A in magnitude (Δm = $2.5 \log \mu$) as a function of inverse wavelength. The wavelength dependence is well reproduced by Δm = $0.145 / \lambda(\mu$m) (dashed line)

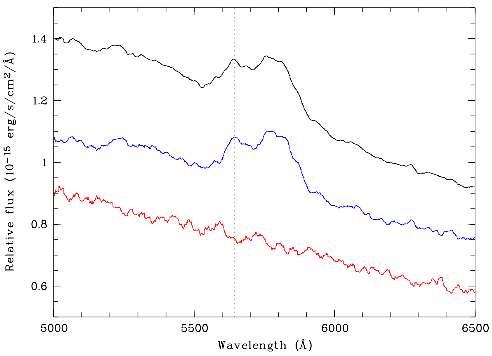

Fig. 12. An enlargement of the spectra of components A (upper) and B (middle, multiplied by 3.7), together with the difference spectrum A−3.7×B (lower, multiplied by 2). The region of the CIII] emission line is illustrated. The wavelengths of AlIII $\lambda\lambda$1855, 1863 and CIII] λ1909 are indicated at the redshift of the quasar (z= 2.03). This blend is typical of BAL quasars (Hartig & Baldwin 1986). Some subtle differences in the blue part of the line profiles may be noticed (see text).

of components A and B (Fig. 12), small differences are indeed present in the blue wing of the AlIII and CIII] emission lines. Interpreted in terms of microlensing, this could indicate that the part of the BELR is being magnified. Similar profile variations are predicted by the models of Schneider & Wambsganss (1990). Interestingly, no difference in the CIV BAL profile, like those reported for the quadruple BAL quasar H1413+117; cf. Angonin et al. 1990 and Hutsemékers 1993, is noticed.

The present findings may be of importance for investigating the inner structure of quasars. Spectroscopic data obtained at regular time intervals, e.g., spectra separated by intervals corresponding to the time-delay, will test the microlensing interpretation, cancel possible time-delay effects (see Wisotzki et al. 1995) and help to probe the innermost region of quasar structure, using microlensing amplification.

5.3.2. Reddening

An alternative explanation to the observed colour difference between quasar images is that the B image is reddened by the lensing galaxy. Assuming this is true, we can estimate the amount of reddening which would correspond to the strength of the putative Ca H & K absorption lines seen in the B spectrum (Fig. 7), if average Galactic conditions apply to the present case. From the interstellar line observations of Sembach et al. (1993), we derive a mean relation between E(B–V) and the Ca K equivalent width. With a de-redshifted equivalent width $\sim$ 100 mÅ, this would imply a colour excess E(B–V) $\sim$ 0.05, which corresponds to E(V–I) $\sim$ 0.1, using the extinction curves of Mathis (1990), after proper redshift corrections are applied. This is compatible with the measured colour difference of 0.15 (Fig. 8). The extinction can also be estimated by fitting the magnitude difference of the A and B components as a function of wavelength (Fig. 11) with a typical extinction law. In the wavelength range of interest, the Galactic and SMC extinction curves are very similar (Pei 1992) and can be reasonably well represented by

$$A_\lambda = \frac{1.75 E(B-V)}{\lambda(\mu m)} \qquad (2)$$

where A_λ is the extinction in magnitudes, and where the ratio of the total-to-selective extinction R_V is taken to be R_V = 3.1. Identifying the wavelength dependence of the magnitude difference in Fig. 11 to this extinction curve at the redshift of the lens, we have 1.75 E(B–V)(1+z_{lens}) = 0.145 i.e., E(B–V)= 0.05 which is in agreement with what is found from the Ca H & K lines.

In the case of extinction by dust in the lens we would expect the continuum and the BELR to be equally affected. This does not seem to be the case; however, the wavelength range between CIV and the CIII]-AlIII complex is small. A more sensitive test of the dust hypothesis will be to observe H-alpha in the infra-read, as this will provide a larger wavelength baseline to measure differences.

On the basis of the available data, no interpretation can be excluded, although microlensing seems a somewhat more natural explanation for the observed spectral differences.

6. Lens modeling

The time-delay measured for HE 2149−2745 can be used to infer an estimate of H_0, based on modeling of the total gravitational potential responsible for the lensing effect. This includes the main lensing galaxy and any intervening massive cluster along the line of sight to the quasar. HE 2149−2745 is a relatively easy case to model, as there is no obvious mass concentration along the line of sight to the source apart from the main lensing galaxy. Only a marginally detected galaxy concentration is seen 30″ West and 1′ North of the main lens. In addition, this lensing galaxy is almost aligned with the two quasar images (see

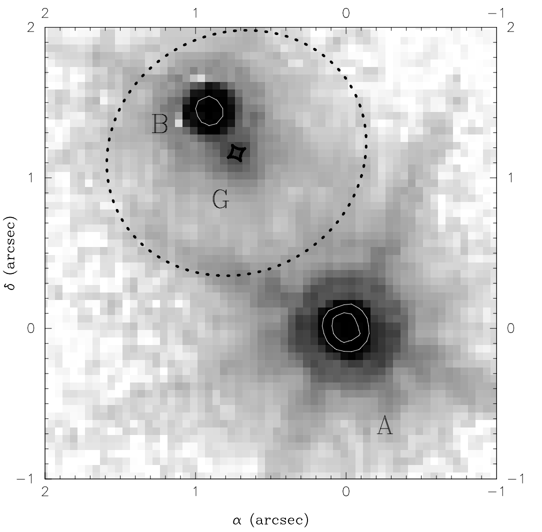

Fig. 13. Field of 3″ around HE 2149−2745, where the lensing galaxy is indicated as "G", close to the faint quasar image "B". Also indicated are the critical and caustic curves created by a single lensing galaxy and no external shear. The image has been obtained from the CASTLEs public survey of gravitational lenses. This image is an I-band HST image (PI: E. Falco).

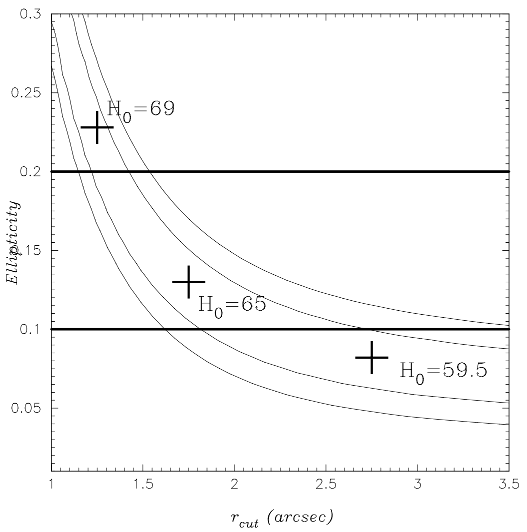

Fig. 14. Results of the model fitting when exploring the ellipticity/cut radius space. The lines show the best models, i.e., they show the area where the models fit the data at 1σ (inner lines) and 3σ (outer lines). Values for H_0 are given for different models among the most likely. The horizontal lines give the plausible range of ellipticities, given the HST images. The plot displayed here uses $\Omega = 0.3$, $\lambda = 0.7$.

Figs. 1 and 13). Two different approaches can be used to convert time delays into H_0: models that involve an analytical form for the lensing galaxy, and others that involve more degrees of freedom, e.g., a pixelated surface mass density (Saha & Williams 1997, Williams & Saha, 2000). We use both approaches.

6.1. Analytical models

Our analytic model uses the mass profile of Kneib et al. (1996): a truncated Pseudo-Isothermal-Elliptical-Mass-Distribution (PIEMD). Truncated PIEMD are elliptical mass distributions smoothly truncated at radius r_{cut}. For radii smaller (respectively larger) than r_{cut}, the projected surface mass density profile is varying as r^{-1} (respectively r^{-3}). The interest in such profile is their ability of characterizing any ellipticity in the mass distribution as well as having a total finite mass. We fit the model to the public HST/WFPC2 data (which offers better resolution and sampling than NICMOS) obtained by Falco, and use the emission line flux ratio of 3.7 calculated from our VLT spectra. During the fit, the astrometry of the quasar images relative to the lens is fixed, as well as the redshift of the source and lens. Free parameters include the velocity dispersion, ellipticity (defined as $[a^2 - b^2]/[a^2 + b^2]$ where a and b are the long and short axis of the lens) and cut radius of the lens.

A common problem in lens modeling is the mass-sheet degeneracy. In other words, several mass profiles and in particular mass profiles of different compactness, will reproduce the same time-delay. One has therefore to constrain the models using observational data and explore the widest range of physically acceptable models. A first constraint comes from the HST images: the lens is almost round. After PSF-subtraction of the quasar images we fit the shape of the lensing galaxy and obtain an ellipticity of about 0.1–0.2. Assuming that the mass distribution follows the light distribution we can restrict ourselves to this range of ellipticities. Fig. 14 shows a family of models exploring the ellipticity vs. r_{cut} space and we see that little spread in the values of H_0 is observed in the range of ellipticities 0.1–0.2. We assume ellipticity $\varepsilon = 0.15$ which implies $r_{cut} = 1.6''$ and $H_0 = 66 \pm 6$ km s^{-1} Mpc^{-1} with additional systematic errors of $\pm$3km s^{-1} Mpc^{-1} due to the limited range of ellipticity. We also try to investigate the existence of a core. For this we scan the possible value for the core radius. The lens model excludes any value of r_{core} larger than 0.02 arcsec. Within this limit, the core radius has basically no effect on the determination of H_0, so the choice of a given core radius is not critical. In our fiducial model, we use a core radius of ~ 0.002 which corresponds to $\sim$10 pc. Using this, and keeping the other parameters free, we find a lens with the parameters summarized in Table 2. We show in Table 3 the effect of a change in cosmology.

If we take the most popular cosmology, i.e., $\Omega = 0.3$, $\lambda = 0.7$, and $\Delta t = 103 \pm 12$ days, we find $H_0 = 66 \pm$

Table 2. Model parameters for HE 2149−2745. The values between brackets are *fixed* during the fit, the others are fitted. The core radius is negligible.

Parameter	Fit
Ω, λ	[0.3, 0.7]
Ellipticity	0.13 ± 0.05
P.A.	62 ± 5 *degrees*
Vel. disp.	$198 \pm 10\, km\, s^{-1}$
r_{cut}	[1.25″]
Core radius	[0.002″= 0.01 *kpc*]
time-delay	[103 days]

Table 3. Influence on the cosmology on the modeling of HE 2149−2745. Values of H_0 are listed for an Einstein–deSitter Universe (Ω = 1.0, λ = 0.), an open Universe (Ω = 0.3, λ = 0.) and a flat Universe with non-zero cosmological constant (Ω = 0.3, λ = 0.7). The models parameter are fixed and set to the ones in Table 2.

Cosmology	H_0 (km s^{-1} Mpc^{-1})
$\Omega = 0.3, \lambda = 0.7$	66 ± 6
$\Omega = 0.3, \lambda = 0.$	67 ± 6
$\Omega = 1.0, \lambda = 0.$	60 ± 6

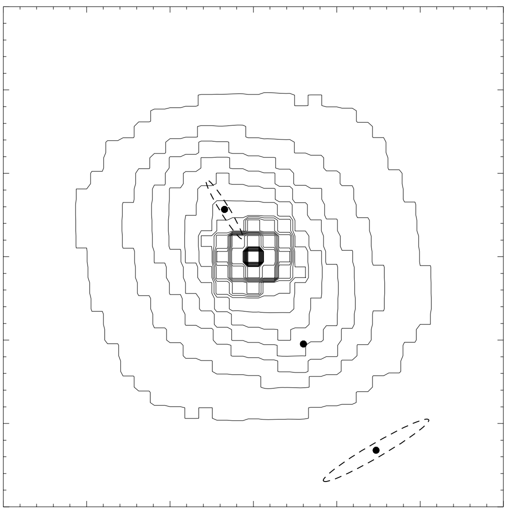

Fig. 15. Mass distribution found with the pixelated models with cosmology Ω = 0.3, λ = 0.7. Almost no ellipticity is found. The scale is 3″ on a side and the astrometry is the same as for the analytical models. The dashed ellipses around the quasar images represent the magnification matrix, i.e., the axes are proportional to the eigenvalues and the orientation corresponds to the eigenvectors. The spot between the quasar images is the position of the lensed source.

6 km s^{-1} Mpc^{-1} with an additional possible systematic error of ±3 km s^{-1} Mpc^{-1} due to parameter choices.

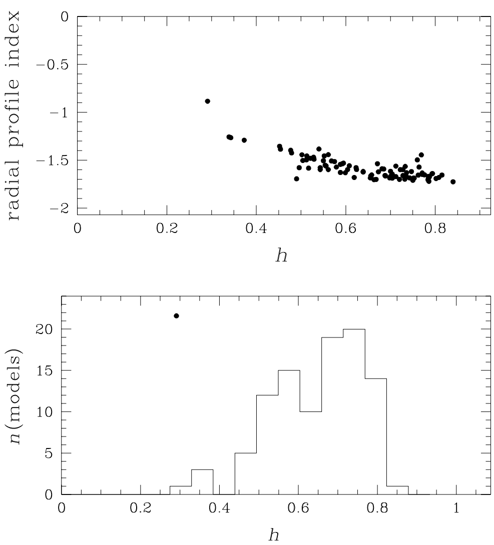

Fig. 16. *Top:* radial index profile vs. H_0 for one hundred different non-parametric models, showing that most plausible galaxies have a sharp mass profile. *Bottom:* probability density for H_0 for the same models. Units on the Y axis of both figures is in h_{100}. The median value of the distribution is 65 km s^{-1} Mpc^{-1}. The black dot marks the location of an isothermal mass profile (radial profile index = -1).

6.2. Pixelated models

The pixelated models of Saha & Williams (1997, 2000) were also applied to HE 2149−2745. While the mass distribution resulting from these models is not as well related to the physical parameters of the lens, they allow us to explore a wide range of lens shapes and to estimate the robustness of the time-delay conversion. Fig. 15 shows the mass distribution found by the models. During the fit, the ellipticity of the mass distribution was kept free. The program reconstructs almost round mass distributions, as does the analytical model (Fig. 14). We also examine the impact of a change in the compactness of the mass profile on the derived value for H_0. Fig. 16 shows the result of a Monte-Carlo simulation where 100 models were run with different indices for the lens's shape, The density index in Fig. 16 represents the logarithmic projected density gradient in the vicinity of the images (cf. Williams & Saha, 2000). The upper panel of the figure shows that most models predict relatively sharp/concentrated mass profiles.

In the lower panel of Fig. 16 we display the H_0 probability distribution. The mean of the distribution peaks at $H_0 = 65 \pm 15$ km s^{-1} Mpc^{-1} at the 2σ level and $H_0 = 65 \pm 7$ km s^{-1} Mpc^{-1} at the 1σ level.

7. Summary - conclusions

We have presented the first result of a long term photometric monitoring campaign undertaken at ESO between 1998 and 2000 at the 1.54m Danish telescope. Our two filter light curves allow us to measure a time-delay of $\Delta t = 103 \pm 12$ between the two quasar images of HE 2149−2745.

From VLT spectroscopy, we have derived a tentative estimate of the lens redshift to be $z = 0.489$. Applying both analytic and numerical lens models to the case of HE 2149−2745, we derive $H_0 = 66 \pm 6$ km s^{-1} Mpc^{-1} with an additional systematic error of ± 3 km s^{-1} Mpc^{-1} in the case of the analytic models, due the limited range of the ellipticity. The derived mass models are relatively compact, although not as compact as the light profile of the galaxy. An extra source of systematics might be introduced by the uncertainty on the lens' redshift estimate. This is however not critical so far for the determination of H_0 as the error is dominated by the uncertainty in the time-delay measurement. As HE 2149−2745 shows smooth light curves, it is likely that the situation can be improved by continued monitoring. An improved time-delay also means that the lens redshift will have to be re-determined more precisely.

Our monitoring program is the first to be carried out in two bands on such a regular basis and over such a long time scale. Given the error bars, we do not see any significant colour variation over 900 days of observation. Moreover, our spectra of the two quasar images show that the flux ratios in the broad emission lines behave differently to the continuum flux ratio, and that the flux ratio measured in the BAL structure of the source follows the behavior as the continuum region. Such behavior can be explained both by microlensing or by extinction by the lensing galaxy (or both). So far, the data do not allow us to distinguish between the two possible explanations. In order to confirm microlensing, one would need for example to know the time-scale of the putative event, i.e., to measure the absolute amplification of the event and its duration. This would not only allow us to confirm microlensing, but also to use it to map the radial structure of the central AGN in the source. Expected time scales are long, of the order of 10 years, and time-delay effects have to be canceled out. This means that using microlensing to probe AGNs may require very long term spectrophotometric monitoring. In the case of HE 2149−2745 one would need for example to obtain light curves over a 10-15 years period, sampled with one point every 103 days.

Acknowledgements. We thank IJAF and ESO for granting us observing time for this project on a flexible basis. We are very grateful to the 2.2m-team for their support and enthusiasm. Most of the monitoring observations presented here have been carried out during short periods of time allocated during the scheduled runs of regular observers. We appreciated very much the enthusiasm of all the observers who accepted to perform the observations for us. Some of them, present at the telescope for long periods, contributed a lot to our program. It is a pleasure to thank in particular J. Pritchard, B. Milvang-Jensen, L. Fogh-Olsen, S. Frandsen, L. Hansen, H. Kjeldsen, J. Knude and G. Israel. We thank Lutz Wisotzki for letting us use his EFOSC spectrum and Prasenjit Saha for help with the non-parametric models. IB is supported in part by contract ARC94/99-178 "Action de Recherche Concertée de la Communauté Française (Belgium)" and Pôle d'Attraction Interuniversitaire, P4/05 (SSTC, Belgium). FC acknowledges financial support through Chilean grant FONDECYT/3990024. Additional support from the European Southern Observatory, through ECOS/CONICYT grant C00U05 and through a CNRS/CONICYT grant are also gratefully acknowledged. JH is supported by the Danish Natural Science Research Council (SNF). JPK thanks CNRS for support.

References

Angonin M.C., Remy, M., Surdej J., Vanderriest C. 1990, A&A 233, L5

Burud I., Hjorth J., Jaunsen A. O., et al., 2000, ApJ, 544, 117

Courbin F., Magain P., Kirkove M., Sohy S. 2000a, ApJ, 539, 1136

Courbin, F., Lidman, C., Meylan, G., Kneib, J.-P., Magain, P. 2000b, A&A, 360, 853

Hartig G.F., Baldwin J.A. 1986, ApJ, 302, 64

Hjorth, J., Burud, I., Jaunsen, A. O. et al., 2001, in Gravitational Lensing: Recent progress and future goals, ASP Conf. Ser., eds. T. Brainerd and C. Kochanek, in press

Hutsemékers D. 1993, A&A, 280, 435

Kinney, A.L., Calzetti, D., Bohlin, R.C., McQuade, K. et al., 1996, ApJ, 467, 38

Kneib, J.-P., Ellis, R. S., Smail, I., Couch, W. J., Sharples, R. M., 1996, ApJ 471, 643

Kochanek C. S., Falco E. E., Impey C. D., et al., 2000, ApJ, 543, 131

Krolik J., 1999, In: Ostriker J.P. (ed.) Active galactic nuclei: From the central black hole to the galactic environment. Princeton Series in Astrophysics, Princeton University Press

Kurtz, M. J., Mink, D. J. 1998, PASP, 110, 934

Lidman, C., Courbin, F., Kneib, J.-P. et al. 2000, A&A, 364, L62

Magain P., Courbin F., Sohy S. 1998, ApJ, 494, 452

Mathis J.S. 1990, ARA&A, 28, 37

Mould, J. R., Akeson, R. L., Bothun, G. D. et al., 1993, ApJ, 409, 14

Nadeau D., Racine R., Doyon R., Arboit G. 1999, ApJ, 527, 46

Nemiroff R.J. 1988, ApJ, 335, 593

Osterbrock, D. E. 1989, Astrophysics of Gaseous Nebulae and Active Galactic Nuclei, Universtiy Science Books

Pei, Y. C. 1992, ApJ, 395, 130

Refsdal S. 1964, MNRAS, 128, 307

Saha, P., Williams, L. L. R. 1997, MNRAS, 292, 148

Schneider P., Wambsganss J. 1990, A&A, 237, 42

Schneider P., Ehlers, J., Falco E.E 1992, Gravitational lenses, Springer, Berlin

Sembach K.R., Danks A.C., Savage B.D. 1993, A&AS 100, 107

Tonry, J., Davis, M. 1979, AJ, 84, 1511

Wambsganss J., Schneider P., Paczynski B. 1990, ApJ, 358, L33

Williams, L.L.R., Saha, P. 2000, AJ, 119, 439

Chapter 7

The time delay of the quadruple quasar RX J0911+05

In this chapter I present the observations, data analysis and time delay of the second survey target at the NOT, the quadruple quasar RX J0911+0550 (z = 2.80) which is lensed by a galaxy and cluster at $z = 0.77$.

RX J0911+0550 was discovered by Bade et al. (1997) in the ROSAT All Sky Survey. Burud et al. (1998) (cf. Chapt. 3) found optical and near infra-red (NIR) evidence that RX J0911+0550 is a quadruply lensed quasar with an unusual image configuration requiring a large external shear. The origin of this shear was attributed to a possible nearby cluster at a photometric redshift $z = 0.7 \pm 0.1$. Recently, Kneib et al. (2000) confirmed the existence of a massive cluster and measured its redshift (z = 0.769) and its velocity dispersion ($\sigma = 836^{+180}_{-200}$ km s^{-1}).

The three A (A1, A2, A3) components of RX J0911+0550 are very close (A1$-$A2=0.478 and A2$-$A3=0.608 arcsec, see Fig. 7.1) and the time delays between them are expected to be short, of the order of a few days. Hence, we first focused on determining the time delay between A and B, separated by 3.1 arcsec, which is expected to be of the order of several months. The images are fairly bright with mean I magnitudes of 17.5 and 19.4 for A and B respectively. Early observations showed that the QSO is strongly variable with a time delay of about 200 days Hjorth et al. (2001).

7.1 Observations, image analysis and photometry

I band images were obtained at the Nordic Optical Telescope (NOT) about once a week between September 1998 and April 2001. These regular monitoring data were supplemented with a few data points obtained at the NOT, the MDM, the Magellan Telescope and the 1.5m Danish Telescope. The object is below the horizon at the NOT in July and August. There were additional gaps in the lightcurves due to periods with bad weather or Spanish and international time allocation. Three different instruments were used: ALFOSC (Andalucía Faint Object Spectrograph), HiRAC (High Resolution Adaptive Camera) and the stand-by camera StanCam, equipped with detectors yielding pixel scales of 0.189, 0.107 and 0.176 arcsec respectively. The I band was chosen to minimize the sensitivity to lunar phase. One data point typically consists of 3 exposures of 3–5 minutes each. The seeing varied from 0.6 to 1.5 arcsec, with 0.9 arcsec being the most frequent value. We typically obtained a signal-to-noise ratio (S/N) of 200-300 for the integrated light of the

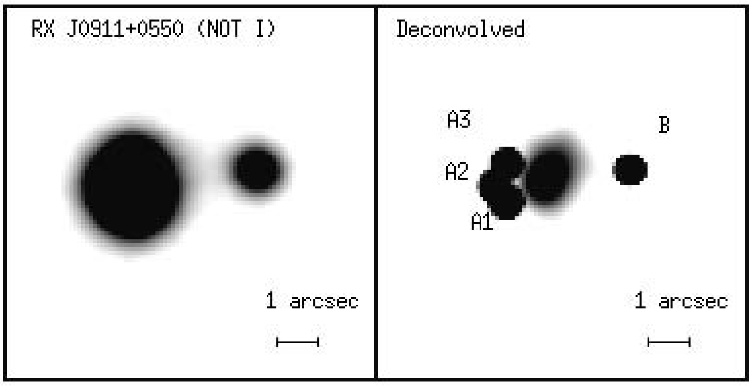

Figure 7.1: *Left*: Stacked I-band images of RX J0911+0550 from a total of 11 hours of exposure and a seeing of 0.9 arcsec. *Right*: The deconvolved image (FWHM = 0.28 arcsec). The main lensing galaxy can be seen close to the three A components. North is up and East is to the left. The field is 12×12 arcsec.

A components and 50-100 for the B component.

The data were reduced and analyzed as described by Burud et al. (2000). Preprocessing was done by dedicated pipelines while fringe correction and cosmic-ray removal were performed manually. Data from different detectors were brought onto the same photometric reference system (cf. Burud et al. 1998) via appropriate colour terms. The combined frames were deconvolved simultaneously with the MCS deconvolution algorithm. Three reference stars with known magnitudes were used to calibrate the photometry (see Table 7.1 for their coordinates and magnitudes). Images of RX J0911+0550 and the resulting light curves are shown in Fig. 7.1 and Fig. 7.2 respectively.

Table 7.1: Coordinates and I band magnitudes for three reference stars in the field surrounding RX J0911+0550.

	R.A.	DEC	I mag
S1	137.859	5.845	17.34±0.01
S2	137.860	5.862	16.30±0.02
S3	137.871	5.825	17.07±0.01

7.2 Time delay

The I-band lightcurves (Fig. 7.2) contain 74 data points for each component. As predicted by theory, these lightcurves show that B is the leading component. A pronounced V-shaped feature at JD 2451300 (May/June 1999) is seen in the A component followed by several decreases and upturns. These are preceded by similar features in the B component which

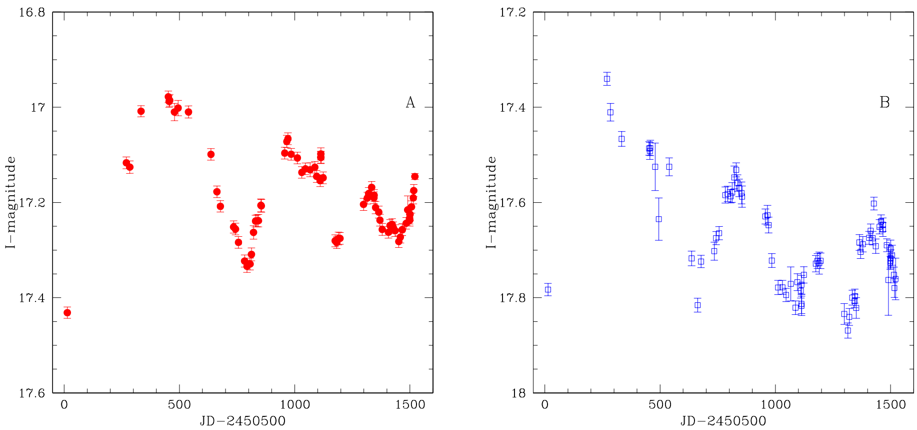

Figure 7.2: *I*-band lightcurves for RX J0911+0550 A (A1+A2+A3) and B. The magnitudes are calculated relative to calibrated stars in the field. The error bars represent photon noise and estimated PSF errors as described by Burud et al. (2000).

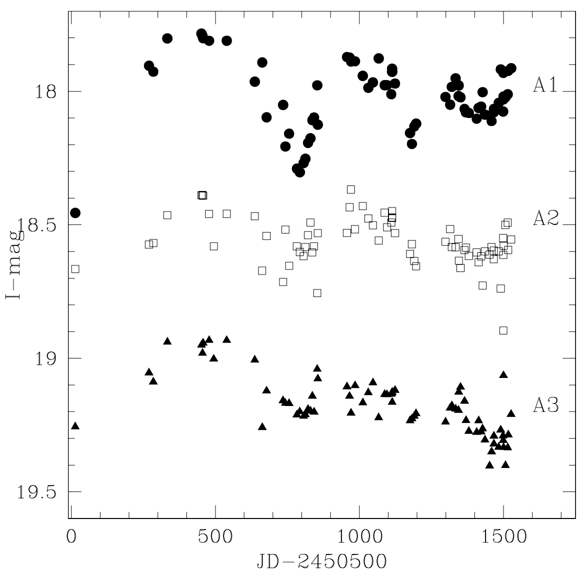

Figure 7.3: *I*-band lightcurves for A1, A2 and A3 in RX J0911+0550. Note the different shape in the A3 curve due to microlensing effects.

allow the determination of a rough time delay of about 150 days. However, it can also be seen that no simple time translation will turn the A curve into the B curve, probably mostly due to external variations (e.g., microlensing effects) and gaps in the light curves.

A quantitative analysis of the light curves was performed using three methods: the minimum dispersion method (Pelt 1996), the recently developed χ^2-based minimization algorithm and its iterative version (Chapt. 2). In all methods a correction for external variations had to be applied in order to measure a time delay. The results, summarized in Table 7.2, show that the value obtained by the minimum dispersion technique is slightly higher than the one obtained with the two other methods. These differences are probably due the different ways of correcting for the external variations.

Our analysis of the individual A1, A2 and A3 curves confirms the presence of external variations in the light curves. We see on Fig. 7.3 that the three curves have slightly different shapes. Unfortunately the S/N in the individual A lightcurves is not high enough to perform a detailed analysis of their variations. The 'external' variations, due e.g. to microlensing are best taken into account by the iterative method (see Chapt. 2). We conclude that the time delay between A and B in RX J0911+0550 is 150 ± 6 days.

Table 7.2: Estimated time delays and I-band magnitude differences for RX J0911+0550 calculated with the three different methods (described in Burud et al. (2000)).

	Δt (days)	Δm (mag)
Minimum dispersion	153±3	$--$
χ^2 fit	147±4	1.88 ± 0.01
Iterative fit	146±4	$1.95 - 2.05$

7.3 Discussion

In modelling the system we used a cosmology with $\Omega_0 = 0.3$, $\Omega_\Lambda = 0.7$, and $H_0 = 100\ h$ km s^{-1}Mpc^{-1}. Adopting an open Universe with $\Omega_0 = 0.3$, $\Omega_\Lambda = 0$ increases the time delay by about 4 percent, whereas an Einstein–de Sitter Universe with $\Omega_0 = 1.0$, $\Omega_\Lambda = 0$ leads to a decrease of about 11 percent. Note however that these effects are smaller than the uncertainties in the mass model.

In the adopted cosmology, the isothermal "yardstick" model of Schechter (2000) predicts a time delay of $111h^{-1}$ with a mass model uncertainty of $\pm 22\ h^{-1}$ days. Kneib et al. (2000) measured a velocity dispersion $\sigma_{obs} = 836^{+180}_{-200}$ km s^{-1} for the galaxy cluster, based on redshift measurements for 24 member galaxies. The predicted time delay for an isothermal cluster with this velocity dispersion is $112.5 \pm 17.5\ h^{-1}$ (Kneib et al. 2000). Adopting this model, our time delay measurement $\Delta t = 150 \pm 6$ days yields an H_0 estimate of 75 ± 12 km s^{-1}Mpc^{-1}. There are additional uncertainties in the determination of the velocity dispersion due to the relatively small number of redshift measurements. Moreover, as pointed out by Saha (2000): (i) for an isothermal lens mass distribution with given "formal" velocity dispersion σ_v, there is a considerably range of allowed line-of-sight velocity dispersions σ_{obs} and (ii) even if the measured velocity dispersion has the expected

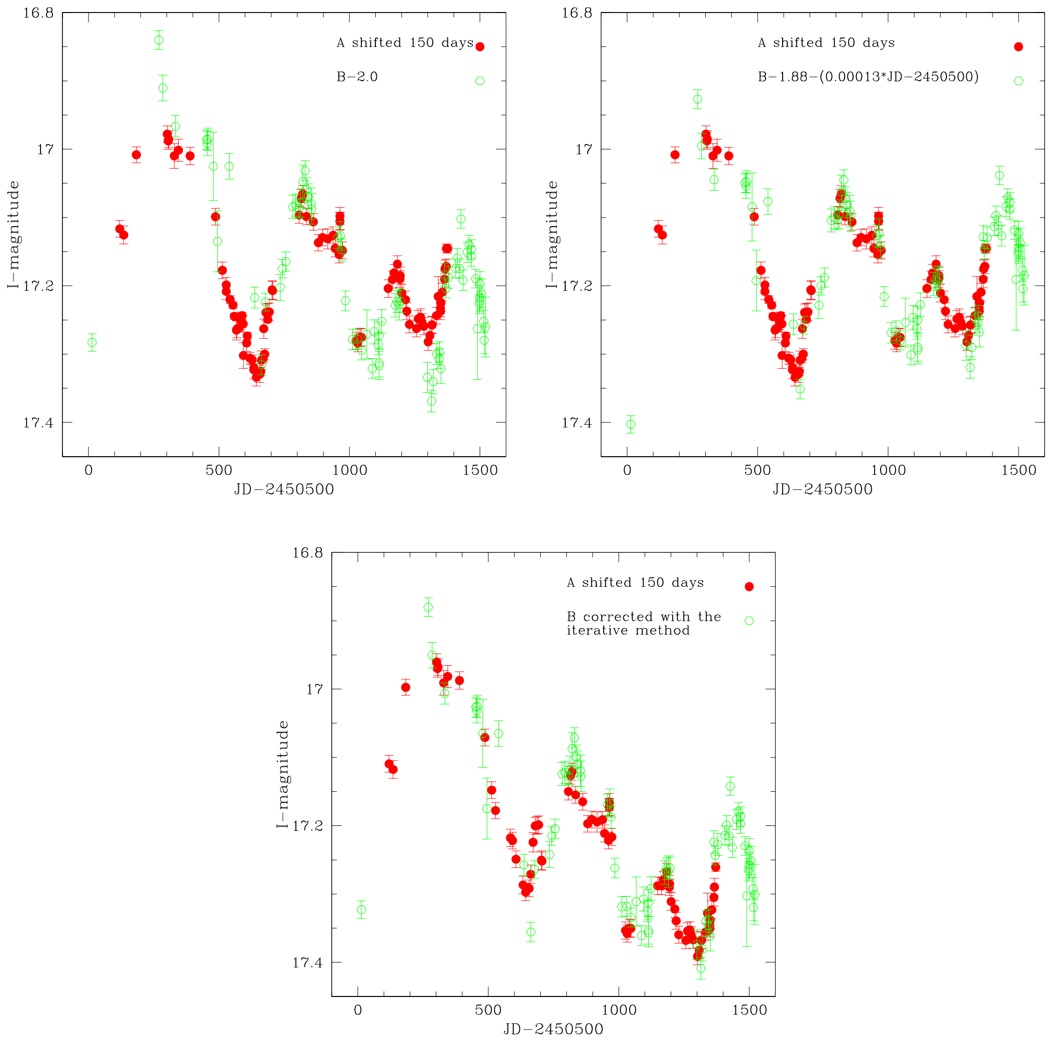

Figure 7.4: *Top left*: Combined lightcurve from both components of RX J0911+0550. The A curve is shifted in time by 150 days and the B curve is scaled with −2.0 mag. *Top right*: Combined lightcurve with the linear correction for external variations. *Bottom*: Combined lightcurve with corrections for external variations derived from the iterative method. The magnitudes are calculated relative to calibrated stars in the field. The error bars represent photon noise and PSF errors as described by Burud et al. (2000).

isothermal value $\sigma_{obs} = \sigma_v$, it does not follow that the lens is isothermal. Due to this degeneracy, there is some freedom in how much mass one can put in the cluster, given the lens configuration and velocity dispersion.

A mass estimate has also been obtained from X-ray observations by the Chandra Observatory (Morgan et al. 2000). These results also suffer from large uncertainties but are in agreement with the results obtained from the velocity dispersion measurements (Kneib et al. 2000).

In this system, the time delay together with a value of H_0 should rather be used to constrain the mass in the cluster. Assuming $H_0 = 65$ km s^{-1}Mpc^{-1} as suggested by measurements from other lensed systems, our measured time delay $\Delta t = 150 \pm 6$ days yields $\sigma_v \simeq 1100$ km s^{-1} for the cluster, a slightly higher value than originally indicated by the velocity dispersion measurement.

Microlensing effects, probably in one of the A components, are present in our light curves. Since the time delay between the three A components is only a few days it will be easy to distinguish microlensing effects form intrinsic variations by conducting regular monitoring with accurate photometry of the three A components. Moreover, the variability of RX J0911+0550 is sufficiently strong and erratic that the prospects for measuring the time delays between A1, A2, and A3 appear within reach from intensive optical or X-ray monitoring. Finally, further mapping of the cluster potential towards RX J0911+0550 to be undertaken from existing HST data and from planned XMM-Newton observations will help to bring down the systematic model uncertainties by determining the cluster convergence so as to make RX J0911+0550 a very useful lens system for further studies.

Chapter 8

Optical time delay measurement in the double SBS1520+530

8.1 Introduction

In this section I present the time delay measurement recently obtained for the double BAL SBS1520+530. The quasar is at redshift 1.86 and was discovered by Chavushyan et al. (1997) as a double gravitational lens system with an angular separation of $1.56''$. The lensing galaxy was detected by Crampton et al. (1998) on near-infrared H band images using the adaptive optics system at the Canada-France-Hawaii Telescope. SBS1520+530 is very well suited for adaptive optics observations given the very near and bright star that can be used as a guide star to correct for the atmospheric turbulence (see Fig. 8.1). The lensing galaxy was also perfectly resolved on images from ordinary ground based images from the NOT using the MCS deconvolution algorithm (cf. Chapt. 3). In addition to the main lensing galaxy, a cluster candidate is detected in the field around SBS1520+530 on V, R and I-band images obtained at the NOT. This cluster should be included when modelling the gravitational potential for the lens. The redshift of the lensing galaxy was unknown until very recently, mostly due to the difficulty of obtaining a spectrum of the faint galaxy severely blended with the much brighter quasar image. Absorption systems along the line of sight are observed in the quasar spectra at redshifts $z = 0.82$ and 0.71 (Chavushyan et al. 1997). However, a redshift estimate $z \sim 0.49$ has been obtained by Falco et al. (1999) by studying differential extinction in the quasar images due to absorption in the lensing galaxy. This redshift estimate does not fit with any of the observed absorption systems. We recently obtained a spectrum of SBS1520+530 at the Keck II telescope with the aim of measuring the redshift of the lensing galaxy. By deconvolving the spectra, the spectrum of the galaxy was detected and a redshift estimate obtained. These spectra are presented in Sect. 8.3. The target shows regular variability and a well constrained time delay has been determined. The monitoring data and the time delay measurement are presented in Sect. 8.2. The spectra are presented in Sect. 8.3.

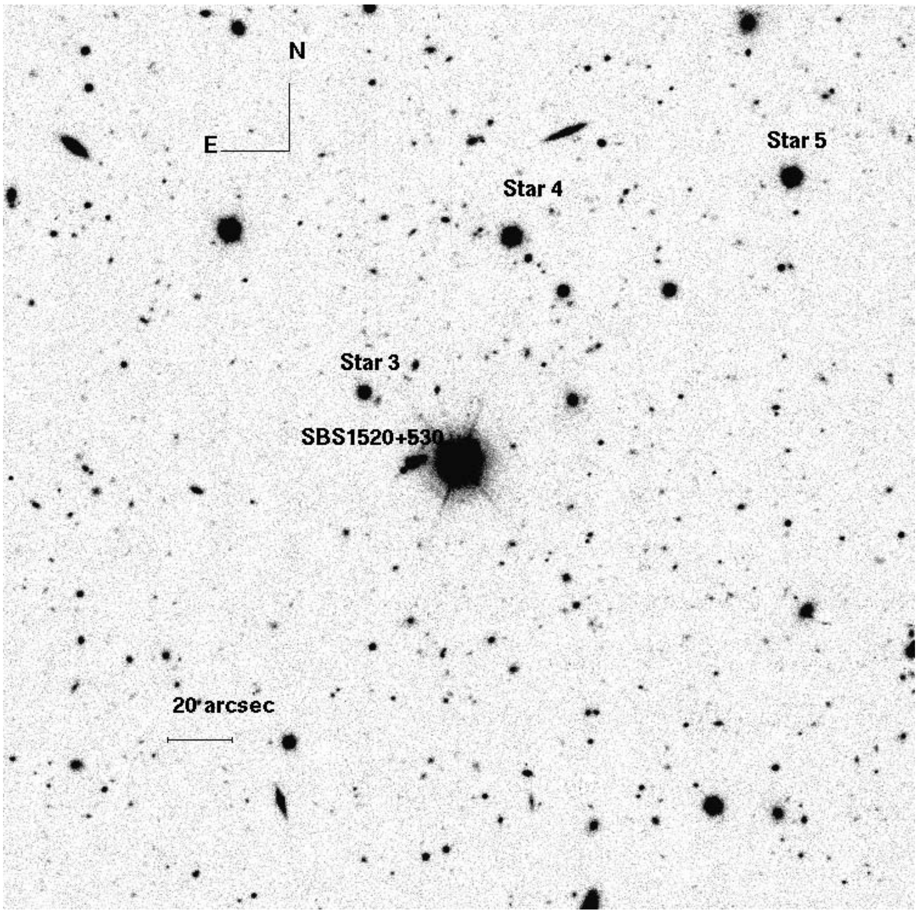

Figure 8.1: The field (~5x5 arcmin) around SBS1520+530 observed with ALFOSC at the NOT. North is up and East to the left. Note the large number of galaxies in the field revealing the presence of a cluster.

8.2 Photometric monitoring at the NOT

8.2.1 Observations and data reduction

Weekly observations of SBS1520+530 were carried out at the NOT from February 1999 to April 2001. The detector ALFOSC (Andalucía Faint Object Spectrograph) with a pixel size of 0.188 arcsec was used for 95% of the frames obtained, the remaining 5% being obtained with HiRAC (High Resolution Adaptive Camera) and the stand-by camera StanCam with pixels sizes of 0.107 and 0.176 arcsec respectively. The target is relatively bright and an exposure time of 300 sec in the R-band was sufficient to obtain a S/N $\sim$ 100 for the quasar images. The seeing varies from 0.5 to 2.2 arcsec with 1.0 arcsec as the most frequent value. Our automated pipeline, employing routines in the IRAF/NOAO/CCDRED package, was used in order to pre-process the CCD frames in an efficient and homogeneous way.

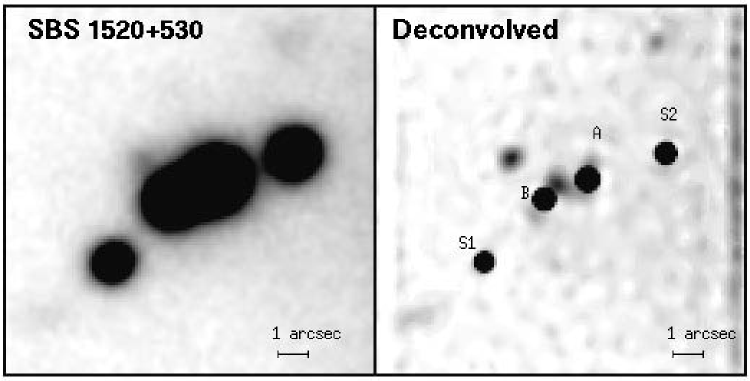

Figure 8.2: *Left*: R-band image of 12″ x 12″ around SBS1520+530. The seeing is 0.9 arcsec. *Right*: Deconvolved image (FWHM=0.28 arcsec) obtained from the simultaneous deconvolution of 59 frames. We see the two stars, S1 and S2, the quasar components A and B, the lensing galaxy close to B and an additional galaxy NE of the lens. North is up and East is to the left.

8.2.2 Photometry and lightcurves

As for the other systems studied in this project, the photometry of the blended quasar images was performed by applying the MCS deconvolution algorithm. The main advantage of this method is its ability to deconvolve simultaneously all the frames from different epochs, hence constraining the astrometry of the two quasar images and the shape of the lensing galaxy using the total S/N of the whole data set. The intensity of the point sources are however allowed to vary from image to image, hence producing the light curves.

The two quasar components are well distinguished on our deconvolved image (see Fig. 8.2), and the lensing galaxy is resolved. Photometry of the quasar images can thus be performed without contamination from the lensing galaxy. Another nearby galaxy is also seen North-East of the lens. The detection of this galaxy has later been confirmed by HST observations.

The light curves of SBS1520+530 consist of 59 data points in the R-band as presented in Fig. 8.3. In addition to the two stars just NW and SE of the quasar (Fig. 8.2), three other reference stars in the field were deconvolved, in order to check the relative photometry and for possible systematic errors (see Fig. 8.1). The photometry is calculated relative to Star 3 in Fig. 8.1. The error bars include both photon noise and additional systematic errors, e.g., PSF errors. The latter are estimated by using the reference stars, as explained in Burud et al. (2000).

8.2.3 Time delay measurement

By sliding "by eye" the light curves across one another we can estimate a rough time delay of $\sim$ 125 days. As predicted by gravitational lens theory, A is the leading component. Using the χ^2 minimization method described in Chapt. 2, a time delay value of 129 $\pm$ 3

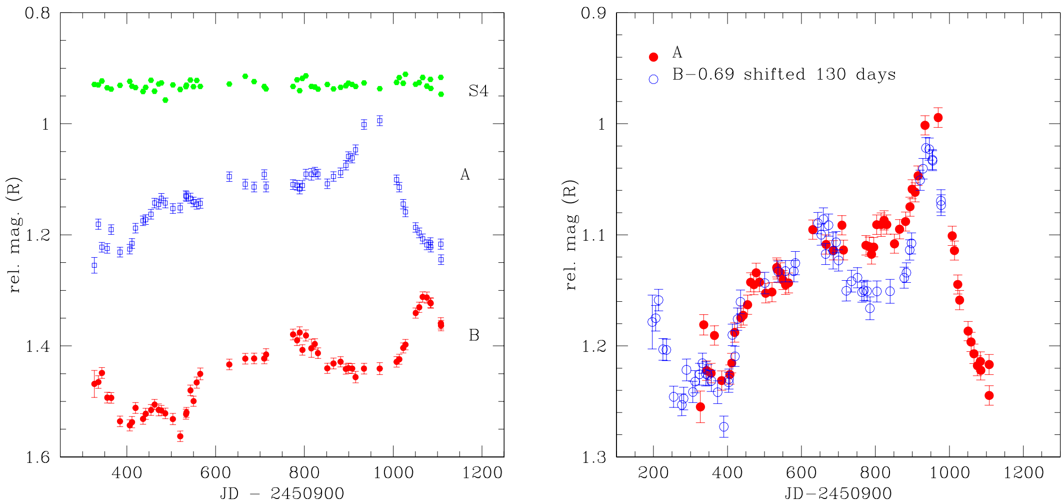

Figure 8.3: *Left*: R-band lightcurves of SBS1520+530 and a reference star S4. The magnitudes are calculated relative to the reference star S3 (Fig. 8.1). The error bars include photon noise and PSF errors estimated from the deconvolution of a reference star. The B component is shifted by -0.4 mag and S4 is shifted by $+0.5$ mag on the plot. *Right*: The light curve of the B component is shifted by 130 days in time and 0.69 mag. No correction for external variations is applied.

(1σ) days is measured on the R-band light curves. The magnitude difference between the A and the B components is found to be 0.692 ± 0.003 mag, corresponding to a A/B flux ratio of 1.892 ± 0.002. The errors are obtained with Monte Carlo simulations of 1000 sets of light curves, assuming that the photometric errors are uncorrelated and follow a Gaussian distribution. When shifting the two curves in time and magnitude (Fig. 8.3) we see that external variations, probably due to microlensing effects, are present in one of the components. Indeed, the best χ^2-fit is obtained when a slow microlensing effect modelled as a linear term with slope determined by the algorithm is included in one of the components. With this external variation the shifted magnitude of the B component plotted in Fig. 8.4 becomes $B = B - 0.692 - 0.000067 \times (JD - 2451226)$. By inspecting the figure we see that the linear correction does not remove all the external variations. Faster variations on time scales of $50 - 100$ days are still present. The iterative version of the algorithm was therefore also applied as an attempt to correct for these external variations. This method yielded $\Delta t = 130 \pm 3$ days, slightly higher than the value found with the direct method but still well within the error bars. Even with the iterative method, some of the fastest variations are not corrected for (Fig. 8.4), notably the small peak in the A curve at ~JD 2451750.

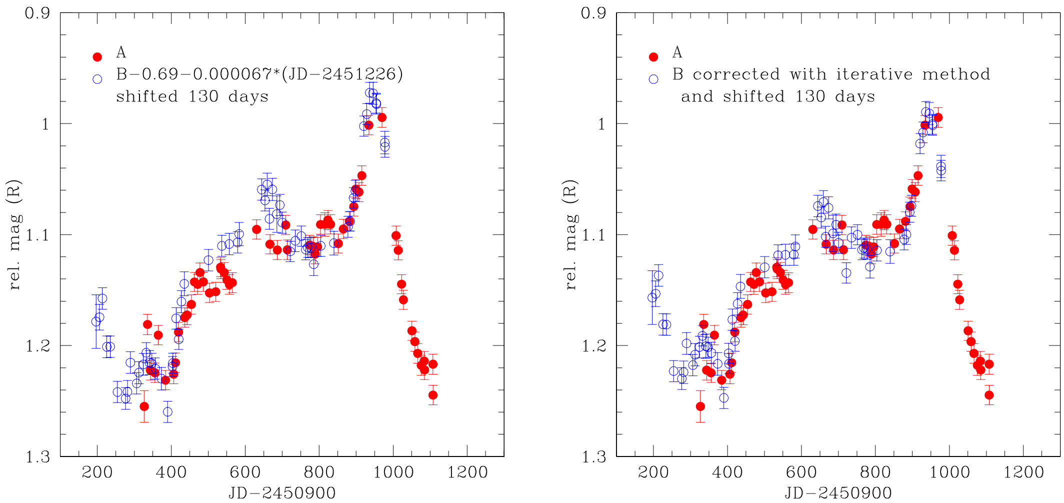

Figure 8.4: Time delay shifted light curves of SBS1520+530 with corrections for external variations. *Left*: B is shifted by 0.69 mag and a linear correction for the external variations is applied. *Right*: The curves are corrected for external variations with the iterative method (cf. Sect. 8.2.3).

8.3 Spectroscopy of SBS1520+530

8.3.1 Keck II spectroscopy

To convert the time delay into an estimate of the Hubble constant, one must know the geometry of the lensing system and this includes the redshift of the lensing galaxy. For this purpose, we obtained an optical spectrum of SBS1520+530 with the Keck II telescope using the ESI (Echelle Spectrograph and Imager). The observations were obtained by J. Cohen on May 23, 2001 under good seeing conditions ($0.6''$). The $1''$ slit was aligned to obtain simultaneously the spectrum of SBS1520+530 and of star S2 (indicated on Fig. 8.2). Four 900s exposures were taken so that cosmic rays could be efficiently removed.

8.3.2 Redshift of the lensing galaxy

Using the spatial information in the spectra of the PSF star S2, the spectrum was spatially deconvolved with the spectral version of the MCS deconvolution method (Courbin et al., 2000b). The deconvolution process decomposes the data into the individual spectra of the two quasar images and the faint lensing galaxy (see Figs. 8.5 and 8.6), as done for the lensed system HE2149-2745 in Chapt. 6. No emission lines were detected in the spectrum of the lensing galaxy (Fig. 8.5). However, an absorption doublet is clearly observed at $\lambda \sim 6700 Å$, matching very well the CaII H and K lines at a redshift of 0.705. This strongly suggests a redshift $z = 0.71 \pm 0.005$, especially since it coincides with one of the absorption systems present in the quasar. The difference in the redshift compared to the absorption systems reported by Chavushyan et al. (1997) is most probably due to

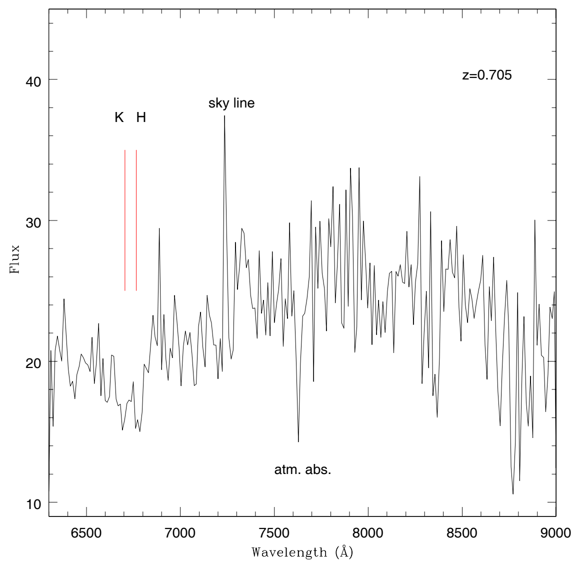

Figure 8.5: Spectrum of the lensing galaxy in SBS1520+530. The CaII (λ 3933, 3968 Å) is identified at redshift $z = 0.705$. Also indicated are a sky emission line and an atmospheric absorption line.

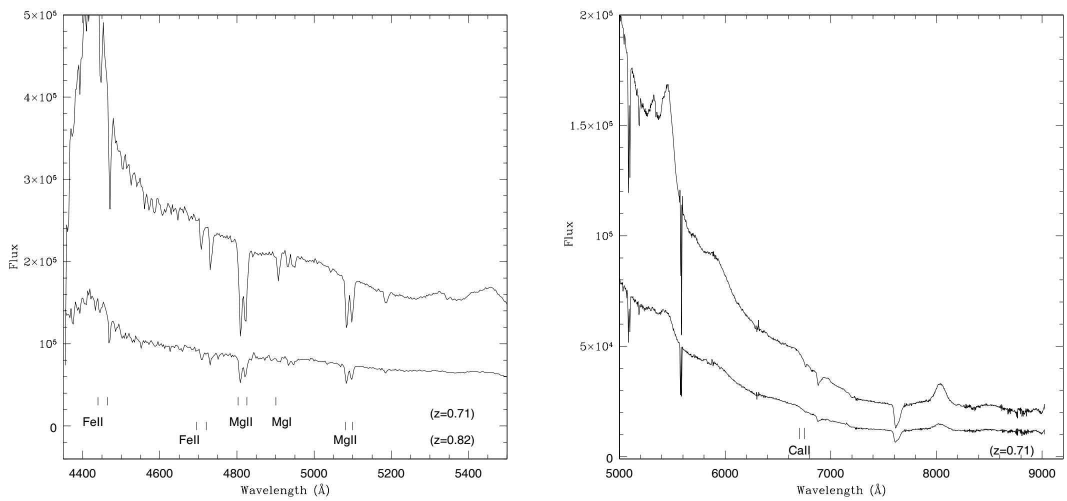

Figure 8.6: Spectra of the quasar components A (top) and B (bottom) of SBS1520+530. Absorption lines corresponding to metal absorption lines at $z = 0.71$ and $z = 0.82$ are indicated.

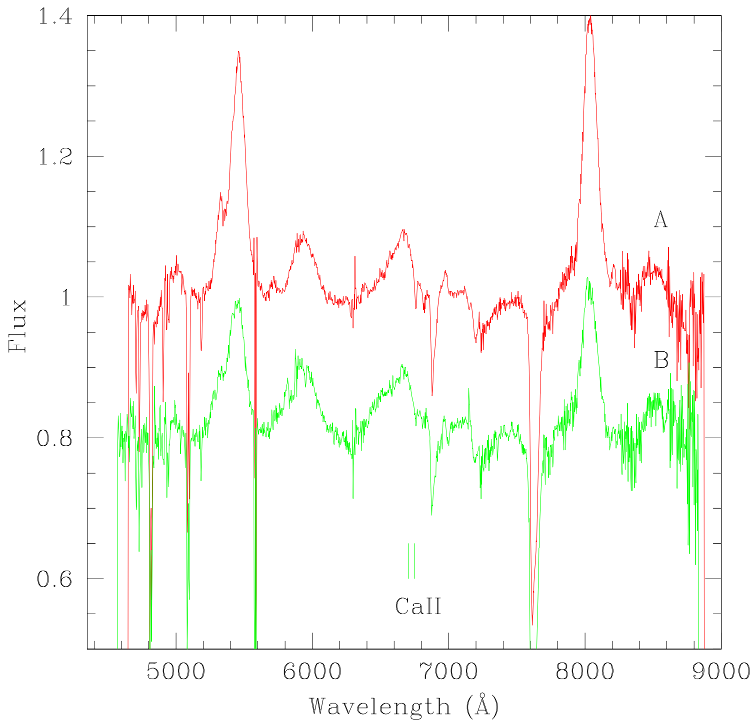

Figure 8.7: The A (top) and B (bottom, vertically shifted by -0.2 for clarity) spectra with normalized continuum. The equivalent widths of the emission lines including AlIII/CIII] and MgII are significantly smaller in B. The CaII absorption lines at redshift 0.71 are indicated.

uncertainties in the wavelength calibration of our spectra. No features corresponding to a redshift of 0.82 or 0.50 were observed in the spectrum of the galaxy, hence ruling out these two candidate redshifts.

8.3.3 Spectra of the quasar components

On the deconvolved spectrum of the two quasar components we detect the metal absorption lines first reported by Chavushyan et al. (1997). The absorption lines for FeII (λ 2587, 2600 Å), MgII (λ 2798Å), MgI (λ2853 Å) at redshifts 0.71 and 0.82, and CaII (λ 3933, 3968 Å) corresponding to the redshift 0.71 are indicated on Fig. 8.6. The CaII doublet for $z = 0.71$ is better seen in the normalized spectra (Fig. 8.7). We also see the quasar emission lines AlIII/CIII] (λ 1909 Å) and MgII (λ 2798 Å) with $z = 1.855$.

Due to the rather narrow slit, the shape of the spectra towards the blue wavelengths is most probably corrupted by atmospheric refraction. The observed reddening of B compared to A at the blue wavelengths is therefore most probably not real. This is supported both by multiband images obtained at the NOT in 1998 and the spectra published by Chavushyan et al. (1997), where the B image is bluer than the A image. In the red parts of the spectra, we find a flux ratio of 1.82 (at λ 9000 Å) which, compared with the ratio of 1.892 measured on R band light curves (λ 6500 Å), indicates an almost constant flux ratio in this wavelength range.

The continuum normalized spectra displayed in Fig. 8.7 show that the equivalent widths of the emission lines are much larger in A than in B, suggesting that B's continuum is amplified. Such a differential amplification can be explained by microlensing effects. Assuming that the lensed quasar follows the "standard" AGN model and that we are observing component B through a network of caustics produced by stars in the main lensing galaxy, one can imagine that the inner continuum region of component B is enhanced by a larger amount than the much larger BELR. This interpretation has already been proposed to explain similar spectral differences observed in the double HE1104-1805 (Wisotzki et al. 1993, 1995, Courbin et al. 2000a) and HE2149-2745 (Chapt. 6).

8.4 Discussion

The time delay measured for SBS1520+530 can be used to infer an estimate of H_0, based on modelling of the total gravitational potential responsible for the lensing effect. This includes the main lensing galaxy and any intervening massive cluster along the line of sight to the quasar. A galaxy cluster candidate is observed around the lensed quasar on deep images and this cluster introduces a shear in the lensing potential. A detailed model of the cluster must be performed in order to obtain a good mass model including all intervening galaxies. Nevertheless, since the largest contribution to the lensing potential comes from the main lensing galaxy, an H_0 estimate (although with larger uncertainties) can be derived by modelling the main lens. Adopting a simple analytical SIS (Singular Isothermal Sphere) model, the estimated redshift for the lens $z = 0.71$ and a $\Omega_m = 0.3$, $\Omega_\Lambda = 0.7$ cosmology, we find an H_0 value of 53 ± 4 km s^{-1}Mpc^{-1} where the errors come from the uncertainties in the time delay and in the redshift of the lensing galaxy. For an Einstein de Sitter Universe the value would be 46 ± 4 km s^{-1}Mpc^{-1}. Systematic errors most probably add to these uncertainties since we have not taken into account a shear from the galaxy cluster. Deep imaging of the field, e.g. from HST, and spectroscopy of the cluster members will be needed in order to study the galaxy cluster and to determine its mass distribution.

External variations, probably due to microlensing effects, are observed on the time delay shifted light curves (Fig. 8.3). Part of this effect can be modelled as a linear term, or corrected for with the iterative algorithm for measuring time delays. However, significant external variations of time scales of $\sim$50 days remain after these corrections. Whereas slow variations, such as the one modelled by a linear term, are typical for microlensing events by stars with velocities following the bulk motion of the galaxy, events of shorter duration may occur in cases of microlensing by stars in random motion (e.g., Wambsganss & Kundić 1995). In the case of SBS1520+530 we might observe a superposition of the two effects. An amplification of the continuum in B relative to A can also be explained by microlensing effects. A detailed study of such microlensing effects over time can be used to constrain compact masses in the lensing galaxy and to determine the size of the various regions of the quasar. The most appropriate way to study these effects is by conducting a spectrophotometric monitoring so that variations both in the continuum and in the emission lines can be studied.

Chapter 9

Synoptic discussion

9.1 Four new time delay measurements

Photometric monitoring programmes have been conducted at three telescopes (NOT, 1.5m Danish and NTT) with the aim of measuring time delays from lensed quasars. The main scientific goals are to determine the Hubble constant and to use time delays to study the mass and light distribution in the lensing galaxies. In this project, time delays for four systems have been measured, as summarized below:

B1600+434 was our first target monitored at the NOT. The mass model of the spiral lens galaxy was developed by Maller et al. (2000) and we inferred an estimate of the Hubble constant $H_0 = 52^{+14}_{-8}$ km s^{-1} Mpc^{-1} (95% confidence level) from the measured time delay $\Delta t = 51 \pm 4$ days. Additional variations, most probably due to microlensing effects in one of the quasar images, were detected in the light curves. Light curves with higher sampling will be needed to model the microlensing-induced variations and to constrain the size of compact mass objects in the lensing galaxy. Since the mass distribution in spiral galaxies is generally uncertain, the time delay measurement of this target is more appropriate to constrain the dark matter distribution in the lens, once H_0 is accurately determined from other methods (or other systems).

HE 2149-2745 is a BAL (Broad Absorption Line) quasar observed in V and I bands at the 1.5m Danish telescope. A time delay of 103 ± 12 days was measured from the light curves. By deconvolving VLT/FORS1 spectra we obtained the spectrum of the lensing galaxy. A redshift estimate $z_{lens} = 0.489$ was obtained from a comparison between the spectrum and standard galaxy-templates. Applying an analytical mass model yields $H_0 = 65 \pm 10$ km s^{-1} Mpc^{-1} and using a model based on pixelated density distributions yields $H_0 = 65 \pm 12$ km s^{-1} Mpc^{-1} (both at 95% confidence). Both our high S/N spectrum and our light curves indicate that the flux ratio between the two images is wavelength dependent, which most probably results from long time-scale microlensing effects, but could also be due to extinction from the lensing galaxy.

RX J0911+0550 is a quadruply lensed system where a time delay of 150 ± 6 days has been measured between the sum of the three A-components and the B component (see

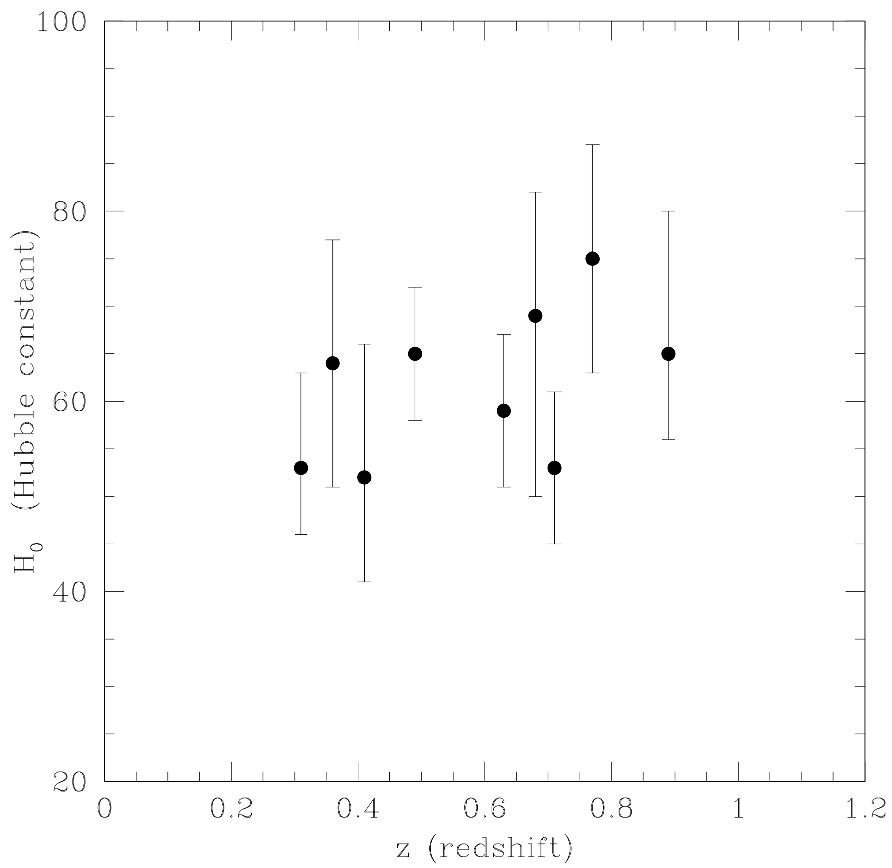

Figure 9.1: The estimated H_0 values from lensed quasars as a function of the lens redshifts. All the error-bars are taken at 2σ.

Sect. 3) on I band data from the NOT. External variations are observed in the lightcurves, probably due to microlensing effects in at least one of the A components. A massive cluster of galaxies is contributing to the gravitational potential. The mass distribution of the cluster is estimated from a measurement of its velocity dispersion by Kneib et al. (2000). A value of the Hubble constant $H_0 = 75 \pm 24$ km s^{-1} Mpc^{-1} (95% confidence) has been inferred from these measurements. The mass estimate is is very uncertain and a better approach for this system is to use a value of H_0 and the time delay to constrain the cluster mass.

SBS1520+530 is a double quasar where a time delay of 129 ± 3 days has been measured from R-band light curves obtained at the NOT. A redshift estimate $z_{lens} = 0.71$ has been obtained from recent Keck II spectra. Modelling the lens as a SIS we obtain an H_0 estimate of 53 ± 8 km s^{-1} Mpc^{-1}. However, additional errors may come from the fact that a cluster of galaxies in the field is not taken into account in the model. Microlensing effects are observed both in the light curves and on the spectra.

9.2 H_0 from all time delay measurements

All estimated H_0 values from lensed quasars are plotted as function of the lens redshift in Fig. 9.1, with error bars representing the 95% confidence (2σ). Measurements from a large range of redshifts (0.3−0.9) give H_0 estimates in agreement with one another. A marginal systematic increase in H_0 with redshifts can be observed in the figure, which could be due to systematic errors, e.g., the uncertainties in the lens redshifts, or it could be due to a physical effect, e.g., an evolution of mass profiles with redshift. We note from the figure and from Table 9.1 that the systems with highest z_{lens} are also the systems with the largest errors in the H_0 estimates. The mass models in these systems are not well enough constrained to determine whether this effect is physical or not.

The mean value of H_0 from the 9 individual measurements shown in Table 9.1 is 60 ± 4 km s^{-1}Mpc^{-1} (95% confidence). This value is obtained by attributing to each value a weight inversely proportional to the square of the quoted errors in the table. For B1600+434 only the value from Burud et al. (2000) was included in the calculation of the mean since this time delay is more accurate than the time delay from radio wavelengths published by Koopmans et al. (2000). For SBS1520+530 we multiplied the errors by two in the calculation of the mean in order to take into account systematic errors induced by the observed cluster of galaxies in this system. By correcting all values to a common cosmology I obtain $H_0 = 62 \pm 4$ km s^{-1}Mpc^{-1} for an $\Omega_m = 0.3$, $\Omega_\Lambda = 0.7$ Univers, and $H_0 = 57 \pm 4$ km s^{-1}Mpc^{-1} for an $\Omega_m = 1.0$, $\Omega_\Lambda = 0$ (Einstein de Sitter) Univers.

One could argue that not all systems should be included since some are far better constrained than others. In some cases there are uncertainties in the mass models due to external shear from clusters of galaxies, (e.g., Q0957+561, RX J0911+0550). In other systems microlensing is influencing the fluxes, which creates uncertainties in the time delays (e.g., HE1104-1805, B1600+434, RX J0911+0550). Nevertheless there is no appropriate rule for deciding *post hoc* where to draw the line between accepting and rejecting a given system. Consequently, I have chosen not to exclude any of the 9 systems.

9.2.1 Systematic errors in H_0 from mass models

In most cases the quoted errors in the inferred values of H_0 include uncertainties in the time delay and uncertainties in the chosen mass model. We should keep in mind that if the adopted mass model is wrong, that is, if the actual mass profile is different from the model, or if the influence of an external shear has not been properly considered, systematic errors are introduced. Witt et al. (2000) find that applying isothermal profiles to five different systems yields H_0 values that agree well with one another. In their sample, only Q0957+562 requires a more complex model due to the massive cluster of galaxies intervening in the gravitational potential. I have applied the method presented by Witt et al. to three of our four systems and I find $H_0 = 45^{+6}_{-5}$ km s^{-1}Mpc^{-1} for B1600+434, $H_0 = 53 \pm 8$ km s^{-1}Mpc^{-1} for HE2149-2745 and $H_0 = 53 \pm 4$ km s^{-1}Mpc^{-1} for SBS1520+530. These values are in good agreement with the values obtained by Witt et al., but the result for HE2149-2745 is lower than the value derived with the more complex models described in Chapt. 6. Similarly to what was concluded by Witt et al. for Q0951-561 I find that RX J0911+0505 needs to be modelled in more detail because of the massive cluster of galaxies. The value obtained for SBS1520+530, in good agreement

Table 9.1: Lensed quasar systems with measured time delays. The errors correspond to 95% confidence interval (2σ).

Lens	Comp.	z_{lens}	Δt (days)	H_0 estimate	Investigators
Q0957+561	(B-A)	0.36	417 ± 3	64 ± 13	Kundić et al. 1997
PG1115+080	(A-B)	0.31	11.7 ± 1.2		Schechter et al. 1997
	(C-B)		25.0 ± 1.6		Bar-Kana 1997
				53^{+10}_{-7}	Courbin et al. 1998
B0218+357	(B-A)	0.68	10.5 ± 0.4	69^{+13}_{-19}	Biggs et al. 1999
PKS1830-211	(B-A)	0.89	26^{+8}_{-10}		Lowell et al. 1998
				65^{+30}_{-18}	Lidman et al. 1999
HE1104-1805	(A-B)	0.73	267 ± 90		Wisotzki et al. 1998
B1608+656	(B-A)	0.63	31 ± 7	59^{+8}_{-7}	Fassnacht et al. 1999
	(B-C)		36 ± 7		
	(B-D)		76^{+9}_{-10}		
B1600+434	(B-A)	0.41	51 ± 4	52^{+14}_{-11}	Burud et al. 2000
	(B-A)		47^{+12}_{-9}	57^{+14}_{-11}	Koopmans et al. 2000
HE2149-2745	(B-A)	0.49	103 ± 24	65 ± 12	Burud et al. 2001
RXJ0911+0550	(As-B)	0.77	150 ± 12	75 ± 24	Hjorth et al. in prep
SBS1520+530	(B-A)	0.71	130 ± 6	53 ± 8	Burud et al. in prep

with the results from the other systems indicates that the cluster in this field introduces a less important shear in the gravitational potential than the cluster in Q0957+561 and RX J0911+0550.

The results for the cases with no cluster suggest that most galaxies share a common density profile. Nevertheless, it is important to obtain time delays for more systems and to test whether all the H_0 estimates derived from isothermal lens models are mutually consistent. Mass models using isothermal profiles will lead to an underestimated value of H_0 if the lens galaxies actually have steeper profiles (and vice versa). Therefore not only must we test whether or not galaxies have common profiles, but we must also check if the inferred H_0 estimates agree with results from other methods in order to corroborate the isothermal profile hypothesis.

For several systems a cluster of galaxies must be added to the main lensing galaxy in order to model the gravitational potential. When such an external shear is present there will be a change in the time delay (relative to the no-shear case) proportional to the strength of the shear (γ). The total effect of a shear on the time delay and hence on H_0 depends on the strength and direction of the shear and therefore cannot be determined without detailed modelling. Complementary observations from large ground based telescopes or space telescopes are required to pin down the mass distribution of intervening galaxies. Mass estimates of a cluster of galaxies can be obtained e.g., from high-resolution X-ray measurements, from weak-lensing analysis of background galaxies or from measurements of the velocity dispersion of the cluster.

9.2.2 Microlensing as noise and signal

In the present study, external variations, most probably due to microlensing effects, are detected in at least three of the four target systems. Moreover, among the targets presented in Table 9.1, microlensing effects are clearly detected in HE1104-1805 (Wisotzki et al. 1993, 1995, Courbin et al. 2000a) and have also been suggested in Q0957+561 (Schild & Smith 1991). Consequently, microlensing is detected in at least half of the systems with measured time delays. Obviously, these external variations act as noise increasing the uncertainties in the time delay measurements. However, the microlensing signal itself, depending on its time scale and amplitude, can be used to constrain (1) the size of the continuum and the line emitting region in the quasar, and (2) the distribution of compact matter in the lensing galaxy (Paczyński 1986, Kayser et al. 1986). Separating microlensing effects from intrinsic variations in a given system has the potential to provide information about source size and mass distribution in the lens, and to considerably improve the time delay measurement in the system.

Using microlensing to study source and lens properties requires that the external variations are well described over time. Given the irregular and often poor sampling of light curves (due to bad weather, periods when the target is not observable, etc.) the external variations are often difficult to disentangle from the intrinsic QSO variations. In the case of microlensing one would expect a difference in the magnification between the very concentrated continuum region of the quasar's AGN and of the much more extended emission lines region. In most AGN models, the observed size of the continuum depends on wavelength, and the Broad Emission Line Region (BELR) is usually believed to be larger than the continuum region by more than one order of magnitude (Krolik 1999). Assuming that a lensed quasar follows the "standard" AGN model and that one component is observed through a network of caustics produced by stars in the main lensing galaxy, we can hypothesize that the inner – and bluer – continuum region of the component is magnified by a larger amount than the outer redder parts. As the BELR is much larger than the central AGN (even the redder parts), it is much less affected by microlensing. This interpretation has already been proposed to explain this type of spectral differences which were observed in the double HE1104-1805 (Wisotzki et al. 1993, 1995, Courbin et al. 2000) and in HE2149-2745 (Chapt. 6). Such chromatic microlensing effects can be studied both from the slopes of continuum spectra and from ratios between the continuum and the emission lines in the various quasar images. Spectrophotometric monitoring therefore appears as an elegant way to study microlensing effects. Since the effect is colour dependent, it can also be studied by regular monitoring in several bands.

9.3 Comparison with other methods

It is natural to ask how H_0 estimates obtained from gravitational lenses compare with results from other methods (see Sect. 1.1.1 for a description of these methods). Values from the physical methods lie between the two different results from the classical methods, and are closer to the values from Tammann & Sandage (2001) than to the ones from Freedman et al. (2000) (see Table 9.2). We must therefore investigate the possibility that estimates from the physical methods are underestimated. In the case of CMB anisotropies the errors are dominated by measurement uncertainties. A conclusion from this method can only be drawn once accurate measurements are obtained with the future satellites Planck and MAP. The method based on the Sunayev Zel'dovich effect assumes that the gas distribution in clusters is uniform. If gas clumping actually happens, the derived H_0 is probably underestimated. In the case of lensed quasars there are several possibilities for systematic errors. A cluster of galaxies perturbing the gravitational potential may induce systematic errors if not properly modelled. However, the value of H_0 can be either over- or underestimated depending on the direction and the strength the external shear, which are specific for each system. External shear will therefore increase the scatter in H_0 determinations but will not introduce a systematic bias in one direction. On the other hand, H_0 will systematically be underestimated (respectively overestimated) if the galaxy mass profiles are systematically steeper (respectively shallower) than the ones used for the mass modelling, e.g., isothermal profiles. It is therefore important to study more systems in order to better understand the mass profiles of the lens galaxies, to check if they share a common density profile and if this profile is similar to that of nearby galaxies.

9.4 The age of the Universe

The age of the Universe not only depends on the Hubble constant H_0 but also on the mean matter density Ω_m and the vacuum energy density Ω_Λ. In the Einstein-de Sitter model ($\Omega_m = 1$, $\Omega_\Lambda = 0$) the expansion age t_0 is exactly 2/3 H_0^{-1}. In all models with $\Omega_\Lambda = 0$ the matter density is dominating the energy density which causes a deceleration of the expansion rate of the Universe, hence its age will always be younger than the Hubble age H_0^{-1}. An $\Omega_\Lambda > 0$, as recent observations suggest, points to an accelerating Universe with an age possibly older than H_0^{-1} (although Ω_Λ must have a very high value). Ages for different cosmological models are shown in Table 9.3. Adopting the mean value of the Hubble constant found from lensing, $H_0 = 60 \pm 4$ km s^{-1}Mpc^{-1} and the most popular cosmological density parameters $\Omega_m = 0.3$ and $\Omega_m = 0.7$) the age of the Universe is 15.7 Gyr.

9.4.1 Other age estimates

Several methods exist for determining a minimum age for our Galaxy, which helps to constrain cosmological models by providing a lower limit on the age of the Universe. The most useful age estimates are obtained for stars located in globular clusters of our Galaxy. For most of the lifespan of ordinary stars, hydrogen burns into helium in the central core, and a balance between the force of gravity and the outward pressure of radiation is established. This phase of evolution is called the "main sequence". Hydrogen exhaustion in the core marks the end of the main sequence. At that point the luminosity of the star increases and its surface temperature drops. By observing this so-called "turnoff" from the main sequence, and comparing it to models of stellar evolution, the masses and ages of stars in these systems can be estimated.

Until recently there was a discrepancy between the estimated age of the Universe based on globular cluster ages and H_0 measurements. On the one hand, from the 1970's until recently the calculated ages of globular clusters remained unchanged at approximately 15 Gyr (VandenBerg et al. 1996). In addition, when dating the Universe with globular clusters, one has to take into account the period of time required for their formation,

Table 9.2: Recent published values for the different methods to measure distances in the Universe, and hence H_0. When two values are given the one to the left results from the HST key program (Freedman et al. 2000) and the one to the right comes from Tammann et al. (2001) (see Sect. 1.1.1 for more details).

Classical methods	H_0	H_0
Local Cepheid galaxies	$71 \pm 2_r \pm 6_s$	54 ± 5
Type Ia supernovae	$72 \pm 9_r \pm 7_s$	58 ± 6
SBF	$70 \pm 5_r \pm 6_s$	
Tully Fisher clusters	$71 \pm 3_r \pm 7_s$	55 ± 5
Fundamental plane	$82 \pm 6_r \pm 9_s$	
Combined	72 ± 8	
Physical methods	H_0	
Sunyaev Zel'dovich	60 ± 18	
CMB	60−90	
Lensed QSOs	60 ± 4	

Table 9.3: The age of the Universe t_0 in Gyr for various values of the Hubble constant H_0, the mean matter density Ω_m and the cosmological constant Ω_Λ.

H_0	Ω_m	Ω_Λ	t_0(Gyr)
50	1.0	0.	13.0
50	0.3	0.	15.8
50	0.3	0.7	18.8
60	1.0	0.	10.9
60	0.3	0.	13.2
60	0.3	0.7	15.7
70	1.0	0.	9.3
70	0.3	0.	11.3
70	0.3	0.7	13.5

which is generally assumed to be about 1 Gyr. On the other hand, the most popular cosmological model was the Einstein-de Sitter model ($\Omega_m = 1$, $\Omega_\Lambda = 0$) translating the most popular H_0 estimates into ages younger than 15 Gyr (cf. Table 9.3).

This controversy now appears as mostly resolved, thanks to improved observational techniques. Results from the Hipparcos satellite have led to a significant downward revision of the ages of globular clusters to 11-14 Gyr (Reid et al. 1997). In addition, more precise estimates of the cosmological parameters suggest a matter density lower than in the Einstein-deSitter model, and a non-zero cosmological constant (de Bernadis et al. 2000, Riess et al. 1998; Perlmutter et al. 1999). Such models lead to an increase in the estimated age of the Universe for a given H_0. Adopting the mean H_0 determined from gravitational lensing, yielding an age of 15.7 Gyr, there is a good agreement between the two techniques for age estimation. However, if H_0 is 72 $\mathrm{kms}^{-1}\mathrm{Mpc}^{-1}$ as claimed by Freedman et al. (2000) the corresponding age (see Table 9.3) is at the limit of what is allowed by the ages of globular cluster. This comparison hence suggests that the H_0 estimates from gravitational lensing and from the group of Tamman & Sandage (2001) are closer to the real value of H_0 than the high values found by Freedman et al. (2000).

Interestingly, this figure is supported by a very recent study based on a completely new method to estimate the age of stars in our Galaxy (Caurel et al. 2001). The amount of radioactive isotope Uranium-238 was measured in an old star with the high resolution spectrograph UVES at the ESO Very Large Telescope (VLT). An age of 12.5 +/- 3 Gyr was obtained. Although the results are still model dependent, the method gives a very direct age determination of the Galaxy and with improved theoretical and laboratory data, it will provide a precise lower limit to the age of the Universe.

Chapter 10

Conclusion

The present research supports the use of gravitational lensing as a reliable method to estimate the age the Universe, and strongly advocates for an H_0 value of approximately 60 km $s^{-1}Mpc^{-1}$. Although this value combines literature data with my own estimates, the present study greatly increases our confidence in this estimate because: (i) I have studied about as many systems as previously available in the literature, and (ii) the values of H_0 obtained in my studies are in good agreement with the values obtained from other lens systems.

An H_0 estimate obtained from gravitational lensing is of major significance because of the persistent disagreement in the H_0 values obtained with the "classical distance indicators", which range from 50-60 to 70-80 km $s^{-1}Mpc^{-1}$. Actually, with an average value of 60 km $s^{-1}Mpc^{-1}$, my H_0 estimate suggests that the different calibrations of the "classical distance indicators" bracket the true value of H_0.

New results are only made possible through advances in the techniques of measurement and analysis. The present research greatly benefited from the MCS deconvolution algorithm which allowed me to perform accurate photometric measurements of QSO images typically separated by less than an arcsecond. Although I only contributed minor refinements to the MCS algorithm, my research exemplifies its power and usefulness. During the last four years, it has been my privilege to witness MCS grow from a budding algorithm to an internationally recognized method setting new standards for photometric measurements. With accurate photometric measurements, lightcurves of QSO images slowly emerged from years of patient monitoring. Translating this information into time delays required to develop a new algorithm for time series analysis, which specifically corrects for external variations (in addition to intrinsic variations) due to microlensing effects in one or several of the QSO images.

The ubiquity of microlensing effects in lensed quasar images comes as an unexpected result of the present research, as this phenomenon was previously thought to be rare. Microlensing is a hindrance to lightcurve analysis, and techniques such as the one that we developed must be further improved to increase the accuracy of time delay measurements. Nevertheless, I would argue that the future of microlensing analysis lies more in extracting the information it contains than in removing the noise it brings. Hence, microlensing can tell us a great deal about (i) how compact dark matter is distributed in galaxies and (ii) the structure of quasars, which is intimately related to their still uncertain nature. Not only better techniques, but also better observational strategies will be needed to analyse the microlensing signal in detail. Research conducted within the frame of this dissertation convinced me that microlensing effects are optimally studied by a combination of regular spectroscopy and multiband imaging. This is because microlensing effects are generally wavelength dependent due to a different magnification of the various parts of the source, e.g., continuum and emission line regions. A spectrophotometric monitoring is however more time consuming and more difficult to conduct than the already painstaking process of obtaining lightcurves from regular optical monitoring. Consequently, I would advocate for a more realistic approach that consists in conducting spectrophotometric measurements at least once per time delay period in addition to more frequent multiband imaging.

The value of H_0, as given in the first paragraph of this conclusion, can be derived from time delay measurements provided that the mass-to-light distributions of lensing galaxies are sufficiently well constrained. Consequently, in estimating H_0, more weight is given in the averaging process to values obtained from well constrained systems. I am convinced that in the years to come a consensus on the true value of H_0 will be reached, and that gravitational lensing will have greatly contributed to this achievement. At that moment, and already now to a lesser extent, gravitational lensing will provide us with a formidable tool to probe dark matter in galaxies and clusters of galaxies. This second important application let us foresee a bright and long future for gravitational lensing studies even long after the question of H_0 is finally resolved.

Bibliography

Abbott, L. F., 1988, Sci. Am., 258, 106

Angonin, M.-C., Vanderriest, C., Remy, M., Surdej, J. 1990, A&A, 233, L5

Angonin-Willaime, M.-C., Soucail, G., & Vanderriest, C. 1994, A&A, 291, 411

Alcock, C., Akerlof, C. W., Allsman, R. A. et al., 1993, Nature, 365, 621

Aubourg, E., Bareyre, P., Bréhin, S. et al., 1993, Nature, 365, 623

Bade, N., Siebert, J., Lopez, S., Voges, W., Reimers, D. 1997, A&A, 317, L13

Balbi, A., Ade, P., Bock, J. 2000, ApJ, 545, L1

Bar-Kana, R. 1997, ApJ, 489, 21

Birkinshaw, M. 1999, Phys. Rep., 310, 97

Burud, I., Courbin., F., Lidman, C. et al., 1998, ApJ, 501, L5

Burud I., Hjorth J., Jaunsen A. O., et al., 2000 ApJ 544, 117

Carlstrom, J. E., Joy, M., Grego, L. et al., 2001 review of Sunyaev-Zel'dovich Effect to appear in "Constructing the Universe with Clusters of Galaxies", IAP conference, July 2000, eds. F. Durret and G. Gerbal

Caurel, R., Hill, V., Beers, T. C. et al., 2001, Nature, 409, 691

Courbin, F., Lidman, C., Meylan, G., Kneib, J.-P., Magain, P. 2000a A&A, 360, 853

Courbin F., Magain P., Kirkove M., Sohy S. 2000b, ApJ, 539, 1136

Chavushyan, V. H., Vlasyuk, V. V., Stepanian, J. A. et al., 1997, A&A, 318, L67

Crampton, D., Schechter, P. L., Beuzit, J.-L., 1998, AJ, 115, 1383

de Bernadis, P., et al., 2000, Nature, 404, 955

de Vaucouleurs, G., 1981, NYASA, 375, 90

Eisenstein, D., J., Hu, W., Tegmark, M. 1998, ApJ, 504, L57

Faber, S. M., & Jackson, R. E., 1976, ApJ, 204, 668

Falco, E. E., Lehar, J., Shapiro, I. I. 1997, AJ, 113, 540

Falco, E. E., Kochanek, C. S. & Muñoz 1998, ApJ, 494, 47

Falco, E. E., Gorenstein, M. V., & Shapiro, I. I., 1991, ApJ, 372, 364

Falco E., Impey C.D., Kochanek C.S. et al., 1999, ApJ 523, 617

Feast, M. & Walker, A. R., 1987, AR&A, 25, 345

Fishcer, P., Bernstein, G., Rhee, G., Tyson, J. A. 1997, AJ, 113, 521

Freedman, W., D. Schramm memorial Volume, Physics Reports, Elsevier, 2000 (astro-ph/9909076)

Fynbo, J. U., Burud, I., Møller, P. 2000, A&A, 358, 88

Golse, G., Kneib, J.-P., Soucail, G. 2001, astro-ph/0103500

Grogin, N. A. & Narayan, R. 1996, ApJ, 464, 92

Helbig, P., 2000, astro-ph/0011031

Hjorth, J., Burud, I., Jaunsen, A. O., Andersen, M. I., Korhonen, H., Clasen, J. W., Østensen, R. 2001, in Gravitational Lensing: Recent progress and future goals, ASP Conf. Ser., eds. T. Brainerd and C. Kochanek, in press

Hook, R.N., Lucy, L., in The Restoration of HST Images and Spectra-II, R.J. Hanisch and R.L. White, eds., p. 86 (1994)

Hu, W., Fukugita, M., Zaldarriaga, M. ,Tegmark, M. 2000, ApJ, 549, 669

Hu, W. & White, M. 1996, ApJ, 441, 30

Hutsemékers, D., 1993, A&A, 280, 435

Kassiola, A. & Kovner, I. 1993, ApJ, 417, 450

Kayser, R., Refsdal, S., Stabell, R., 1986, A&A, 166,36

Kochanek, C. S., Falco, E. E., Impey, C., Lehar, J., McLeod, B., Rix, H.-W.: URL: http://cfa-www.harvard.edu/glensdata

Kochanek, C. S., Keeton, C. R. & McLeod, B. A. 2001, ApJ, 547, 50

Kneib, J.-P., Cohen, J., & Hjorth, J., 2000, ApJ, 544, L35

Koopmans, L. V. E, de Bruyn, A. G, Xanthopoulos, E., & Fassnacht, C. D. 2000, A&A, 356, 391

Krolik J., 1999, In: Ostriker J.P. (ed.) Active galactic nuclei: From the central black hole to the galactic environment. Princeton Series in Astrophysics, Princeton University Press

Kundić, T., Turner, E. L., Wesley, C. et al., 1997, ApJ, 482, 75

Lange , A. E., et al., 2001, Phys.Rev. D63, 042001 (astro-ph/0005004)

Lucy, L. Astron. J., 1974 79, 745

Madore, B. F., & Freedman, W., 1991, PASP, 103,933

Magain P., Courbin F., Sohy S., 1998, ApJ 494, 452

Maller A. H., Simard, L., Guhathakurta, P. et al. 2000, ApJ, 533, 194

Monier, E. M., Turnshek, D. A., Lupie, O. L. 1998, ApJ, 496, 177

Morgan, N. D., Chartas, G., Malm, M. et al. 2001, ApJ, in press, astro-ph/0103041

Narayan, R., Bartelmann, M. 1995, "Formation of Structure in the Universe", Proceedings of the 1995 Jerusalem Winter School; edited by A. Dekel and J.P. Ostriker; Cambridge University Press

Narayan, R., Nityananda, R., ARA&A 1986, 24, 127

Paczynski, B., 1986, ApJ, 301, 503

Paczynski, B., 1996, ARA&A, 34, 419

Peacock, J. A., Cole, S., Norberg, P. et al., 2001, Nature, 410, 169

Peebles, P. J. E. 1993, "Principles of Physical Cosmology", Princeton Series in Physics

Pelt, J., Kayser, R., Refsdal, S. et al. 1996 A&A, 305, 97

Perlmutter, S. et al., 1999, ApJ, 517, 565

Pijpers, F., 1997, MNRAS, 289, 933

Press, Rybicki & Hewitt, 1992, ApJ 385, 416

Refsdal S., MNRAS 1964a, 128, 295

Refsdal S., MNRAS 1964b, 128, 307

Refsdal, S. & Surdej, J. 1994, Rep. Prog. Phys., 57, 117

Reid, N., 1997, AJ, 114, 161

Renn, J., Sauer, T., Stachel, J., 1997, Science, 275, 184

Richardson, W. H. J. Opt. Soc. America bf 1972, 62, 55

Riess, A. G., Press, W. H., & Kirshner, R. P. 1996, ApJ, 473, 88

Riess, A. G., et al., 1998, AJ, 116, 1009

Romanowsky, A. J. & Kochanek, C. S. 1999, ApJ, 516, 18

Rusin, D., Ma, C.-P. 2001, ApJ, 549, L33

Saha, P. 2000, AJ, 120, 1654

Saha, P., Williams, L.R. 1997, MNRAS, 292, 148

Sandage, A., Tammann, G. A. 1982, ApJ, 256, 339

Schechter., P. L., 2000, in New Cosmological and the Values of the Fundamental Parameters, IAU Symp. No. 201, eds. A. N. Lasenby and A. Wilkinson, in press (astro-ph/0009048) Schild, R, Smith, R. C. 1991, AJ, 101, 813

Schild, R. & Thomson, 1995, AJ, 109, 1970

Schmidt, B. P., et al., 1998, ApJ, 507, 46

Skilling, J. & Bryan, R. K., MNRAS 1984, 211, 111

Sunyaev R. A. & Zel'dovich, Y. B., 1970, Astroph. Sp. Sci. 7, 3

Tammann, G. A., & Sandage, A. R. 1995, ApJ, 452, 16

Tonry, J. & Schneider, D. 1988, AJ, 96, 807

Tully, R. B., & Fisher, J. R. 1977, A&A 54, 661

Udalski, A., Szymański, M., Kałużny, J. et al. 1993, Acta Astron., 43, 289

VandenBerg, D. A., Bolte, M. & Stetson, P. B., ARA&A, 1996, 34, 461

Vanderriest, Schneider, Herpe et al., 1989, A&A, 215, 1

Walsh, D., Carswell, R., Weynmann, R., 1979, Nature, 279, 381

Wambsganss, J. 1998, Liv. Rew. in Relativity, vol. 1, 1992-12

Wambsganss, J., Paczyński, B. & Schneider, P. 1990 ApJ, 358, L33

Williams, L. L. R., Saha, P. 2000 AJ, 119, 439

Wisotzki L., Koehler T., Kayser R., Reimers D. 1993, A&A, 278, L15

Witt et al. 2000, ApJ, 544,98

Wozniak, P. R., Udalski, A., Szymanski, M. et al., 2000, ApJ, 540, L65

Zel'dovich, Y. B. & Sunyaev R. A. 1969, Astrophy. Sp. Sci., 4, 301

Zwicky, F. 1937a, Phys. Rev. Lett., 51, 290

Zwicky, F. 1937b, Phys. Rev. Lett., 51, 679